A continuación, se adjunta un conjunto de 4 artículos publicados en revistas científicas de reconocido prestigio en el ámbito del desarrollo del proyecto.

IEEE Access
Multidisciplinary : Rapid Review : Open Access Journal

Received October 5, 2020, accepted October 22, 2020, date of publication November 5, 2020, date of current version November 19, 2020.

Digital Object Identifier 10.1109/ACCESS.2020.3036140

A Day-Ahead Irradiance Forecasting Strategy for the Integration of Photovoltaic Systems in Virtual Power Plants

GUILLERMO MORENO, PEDRO MARTIN, CARLOS SANTOS, FRANCISCO J. RODRÍGUEZ, (Member, IEEE), AND ENRIQUE SANTISO
Department of Electronics, University of Alcala, 28805 Alcala de Henares, Spain

Corresponding author: Carlos Santos (carlos.santos@uah.es)

This work was supported in part by the PROMINT-CM Project, funded by the Comunidad de Madrid and the European Social Fund under Grant S2018/EMT-4366, in part by the HELIOS Project, funded by the Ministerio de Ciencia, Innovación y Universidades under Grant RTC-2017-6231-3, and in part by the Ministerio de Ciencia, Innovación y Universidades through the INERCIA0 Project under Grant RTI2018-098865-B-C33.

ABSTRACT Encouraged by the considerable cost reduction, small-scale solar power deployment has become a reality during the last decade. However, grid integration of small-scale photovoltaic (PV) solar systems still remains unresolved. High penetration of Renewable Energy Sources (RESs) results in technical challenges for grid operators. To address this, Virtual Power Plants (VPPs) have been defined and developed to manage distributed energy resources with the aim of facilitating the integration of RESs. This paper introduces a hybrid irradiance forecasting approach aimed at facilitating the integration of PV systems into a VPP, especially when a historical irradiance dataset is exiguous or non-existent. This approach is based on Artificial Neural Networks (ANNs) and a novel similar hour-based selection algorithm, has been tested for a real PV installation, and has been validated also considering irradiance measurements from an aggregation of ground-based meteorological stations, which emulate the nodes of a VPP. Under a reduced historical dataset, the results show that the proposed similar hour-based method produces the best forecasts with regard to those obtained by the ANN-based approach. This is particularly true for one-month and two-month datasets minimizing the mean error by 16.32% and 9.07% respectively. Finally, to demonstrate the potential of the proposed approach, a comparative analysis has been carried out between the hybrid method and the most used benchmarks in the literature, namely, the persistence method and the method based on similar days. It has been demonstrated conclusively that the proposed model yields promising results regardless the length of the historical dataset.

INDEX TERMS Virtual power plants, hybrid irradiance forecasting, solar power integration, similarity matching.

NOMENCLATURE

ACRONYMS

AI	artificial intelligence
ANN	artificial neural network
BR	Bayesian regularization
DG	distributed generation
EMS	energy management system
ESS	energy storage system
ICT	information and communication technologies
k-NN	k-nearest neighbors
LM	Levenberg-Marquardt
MLP	multilayer perceptron
NWP	numerical weather prediction
PV	photovoltaic
RES	renewable energy source
RNN	recurrent artificial neural network
SCG	scaled conjugate gradient
SH	similar hour-based method
TSA	time series analysis
VPP	virtual power plant

The associate editor coordinating the review of this manuscript and approving it for publication was Fabio Mottola.

NOTATION

BNI	beam normal irradiance $[W/m^2]$
CCF	cloud cover factor [-]
DHI	diffuse horizontal irradiance $[W/m^2]$
GHI	global horizontal irradiance $[W/m^2]$
MAE	mean absolute error $[W/m^2]$
MAPE	mean absolute percentage error [%]
NRMSE	normalized root-mean-square error [%]
PICP	Prediction Interval Coverage Probability [-]
α	elevation angle [rad]
θ_z	zenith angle [rad]
Ψ	azimuth angle [rad]
δ	declination angle [rad]
Φ	latitude angle [rad]
S	spatial pixel resolution [km]
H	cloud height [km]
(X, Y)	site location [pixel]
(R_X, R_Y)	relative cloud position [pixel]
(P_X, P_Y)	cloud location [pixel]
E	extra-terrestrial radiation $[W/m^2]$
T	temperature [°C]
D	difference vector [-]
u	uncertainty threshold [km]
ω	weight [-]
ED	Euclidean distance [-]
t	prediction hours [h]
z	past hours [h]
s	similar hours [h]
c	candidate hours [h]
N	normal distribution [-]
μ	mean value [-]
σ	standard deviation [-]
Y_t	measured data $[W/m^2]$
$\hat{Y}_t$	forecast value $[W/m^2]$

I. INTRODUCTION

The adoption of photovoltaic (PV) power generation is rising steeply worldwide [1]. There are several reasons behind its success: (a) the cost of photovoltaic power has plummeted since PV modules, storage systems and balance of system costs have been steadily dropping [2]. This has led to an increasing competitiveness in comparison to the conventional non-renewable resources; (b) PV peak power generation coincides with the time of higher load demand; (c) the increasing concern about climate change has definitely spread throughout the world and the electricity sector is playing a central role to fully decarbonize the power system. As a result, governments have implemented supportive policies to encourage investments in renewable sources of energy [3]; (d) the search for energy independence in most developed countries; and (e) most importantly the continued progress and improved accuracy of forecasting strategies of PV generation.

In general, power forecasting for renewable energy sources (RESs) has posed a considerable challenge during the last decade. This has particularly been the case for non-predictable resources such as solar energy where the power generation constantly fluctuates on account of meteorological factors such as cloud cover, temperature, wind speed or humidity level, which are stochastic in nature. This inherent uncertainty has hindered PV power integration at a high penetration level [4], [5]. This drawback can be overcome by including energy storage systems (ESSs) whereby this intermittent source of energy becomes more dispatchable [6]–[8]. However, a more technical and economic solution has been put forward: the aggregation of several PV systems into the so-called Virtual Power Plant (VPP) [9]–[11]. This approach allows prosumers [12], to maximize revenue opportunities by participating in the energy market mechanisms and by taking part in the operation of distribution and transmission networks in terms of the active control and services VPPs can provide, e.g. voltage regulation and frequency balancing, among others.

A VPP usually integrates four components [9]: (a) Distributed Generation (DG) units based on RESs and small scale fossil fuel conventional dispatchable generators; (b) ESSs; (c) responsive or flexible loads; and (d) information and communication technologies (ICTs) which play an essential role in the technological core of a VPP: the energy management system (EMS). The EMS coordinates the power flows among the different units in the VPP. Through a bidirectional communication strategy, which should be based on existing open standards such as the IEC 61850 [13], the VPP not only obtains information about the current state of the different nodes but also sends the commands related to specific targets, e.g. minimization of the generation costs, maximization of profit or reduction of greenhouse gases, to name a few. A crucial part, in the VPP general concept, involves obtaining accurate and rapid forecasts of the power generated by RESs with stochastic nature [14]. The purpose of forecasts is threefold: firstly, the power predictions allow VPP operators to meet regulatory requirements increasing the reliability and efficiency of the of the VPP; secondly, accurate predictions contribute to grid stability; and finally, more favourable trading conditions on the electricity markets can be achieved thereby maximizing revenue.

In the literature, there is a broad range of studies aimed at obtaining accurate forecasts. In this regard, [15]–[19] present comprehensive reviews of well-established techniques developed to forecast PV power generation. According to different factors, forecasting methods can be categorized into different groups. Regarding the forecasted parameter, two different approaches have been implemented: direct [20] and indirect [21]. Through historical datasets of weather conditions and PV power generation, the direct method predicts the generated power. Indirect forecasting, on the other hand, firstly predicts the solar irradiance and then, the output power is calculated by using a performance model of the PV plant. This approach is based on several methods including Numerical Weather Prediction (NWP) models, image-based systems, statistical-based alternatives and hybrid or ensemble methods. As for the time horizon, four categories can be found [22], [23]: very short term forecast also called nowcasting (from 1 min to several minutes), short-term forecast (from 1 hour to several hours), medium term forecast (from 1 month to 1 year) and long-term forecast (up to several years). As far as the model approach is concerned, four types have been widely used: (a) statistical models based on time series analysis (TSA) which tries to identify patterns between historical datasets and the output parameters; (b) artificial intelligence (AI) models mainly based on artificial neural networks (ANNs); (c) physical strategies which use solar and PV models for solar power forecasting; (d) hybrid models which explore different algorithm combinations with the aim of improving forecast accuracy and reducing computational burden for online forecasting applications [22]. Another ongoing challenge in solar power forecasting consists in assessing the uncertainty of the results. To assist with this, deterministic forecasting, also called point forecasting, produces a single value for each timestamp within the time horizon without considering either the upper and lower bounds or the percentage of confidence for each value. Probabilistic forecasting, on the other hand, provides additional accurate information about the expected values in terms of the range of plausible values and the probability associated to each of them [17]. Finally, regarding the spatial horizon, forecasting techniques can be applied to a single plant or to an ensemble with the last option being of major interest because it usually provides greater accuracy.

As mentioned above, the indirect forecasting approach aims firstly at predicting the solar irradiance, mainly global horizontal irradiance (GHI), and then by using the physical model of the PV system, the output power is calculated. This is the strategy used in this paper for one reason: weather-related variables and irradiance datasets can be obtained from ground-based meteorological stations. Likewise, cloudiness and temperature forecasts are freely available from weather forecast web services such that of AEMET in Spain [24]. This clearly facilitates stable and accurate forecasts even in the initial stage of the PV system operation [21]. As opposed to indirect forecasts, direct approaches require an extensive historical dataset for the derivation of the power forecast model, which reduces the possibility of accurate predictions when a new VPP node is integrated. It would be interesting to forecast other irradiance-related parameters such as Diffuse Horizontal Irradiance (DHI) and Beam Normal Irradiance (BNI). However, there are no datasets for these variables since the GHI is usually the only parameter measured by meteorological stations. That is the reason why indirect forecasting methods are mainly developed for GHI predictions and for the other irradiance-related variables are virtually non-existent, especially for DHI [25] in which issues relating to sensor calibration and spatial representativeness are difficult to address [26].

Approaches to irradiance forecasting can range from the most basic such that of similar day-based method to the most demanding in terms of computational load such as Recurrent Artificial Neural Networks (RNNs) which require computationally demanding training algorithms. The similar day-based approach provides an appropriate choice for irradiance forecasting. Similar day-based forecasting involves mining a dataset with the aim of finding days or even hours which are similar to the forecast day/hour in terms of certain parameters such as cloudiness and temperature [27]. The success of this alternative relies on the low computational burden it imposes on the forecast algorithm. On the other hand, ANNs have been extensively used for daily solar irradiance forecasts [28]–[33]. The forecast performance of an ANN relies on the learning algorithm along with the data available for the training process, the transfer function, the architecture, the nonlinear mapping capacity and the choice of input variables. The main limitation of ANNs stems from the fact that they required an extensive dataset for training purposes for better generalization and accuracy. Conversely, similarity matching works better than ANNs for short datasets, especially when a time granularity of one hour is considered. This enhancement is demonstrated conclusively in this work. Therefore, in the context of a VPP and at the earlier stages of its operation when limited data is available, hybrid strategies, which combine different methods, can improve the overall forecasting accuracy. In general, hybrid techniques have been widely used in diverse industrial applications [34], [35], delivering good results.

In this paper, an irradiance short-term forecasting strategy is presented, with the aim of facilitating the integration of PV systems in VPPs, especially when the lack of a comprehensive dataset hinders the forecasting performance of the algorithms causing inaccurate results. This strategy is based on a hybrid approach which combines an ANN and a novel similar hour-based forecasting algorithm. The outputs of both forecasting methods are dynamically weighted, according to the type of the day and some accuracy metrics, to provide the final forecast. The forecasting approach relies on no-cost temperature and cloudiness forecast maps generated by the AEMET via NWP, the irradiance measurements from a real PV installation located in the Polytechnic School of Alcala University and different ground-based meteorological stations emulating the role of VPP nodes.

The main contributions of this paper are summarized as follows: (i) the proposed forecasting approach is implemented in the context of a VPP considering the challenges it poses and drawing on its strengths; (ii) the input data for the forecasting algorithms comes from weather forecasts regularly published, free of charge, by the AEMET; (iii) the similar hour-based approach, which produces accurate irradiance forecasts for a reduced dataset, this usually being the case when a new node is integrated in the VPP; and (iv) the ensemble of ANNs and the similar hour-based approach which, through a dynamically weighted function that depends on the type of day, produces encouraging results.

The paper is organized as follows. Section II introduces a general description of the irradiance forecasting hybrid approach. In section III the data description and

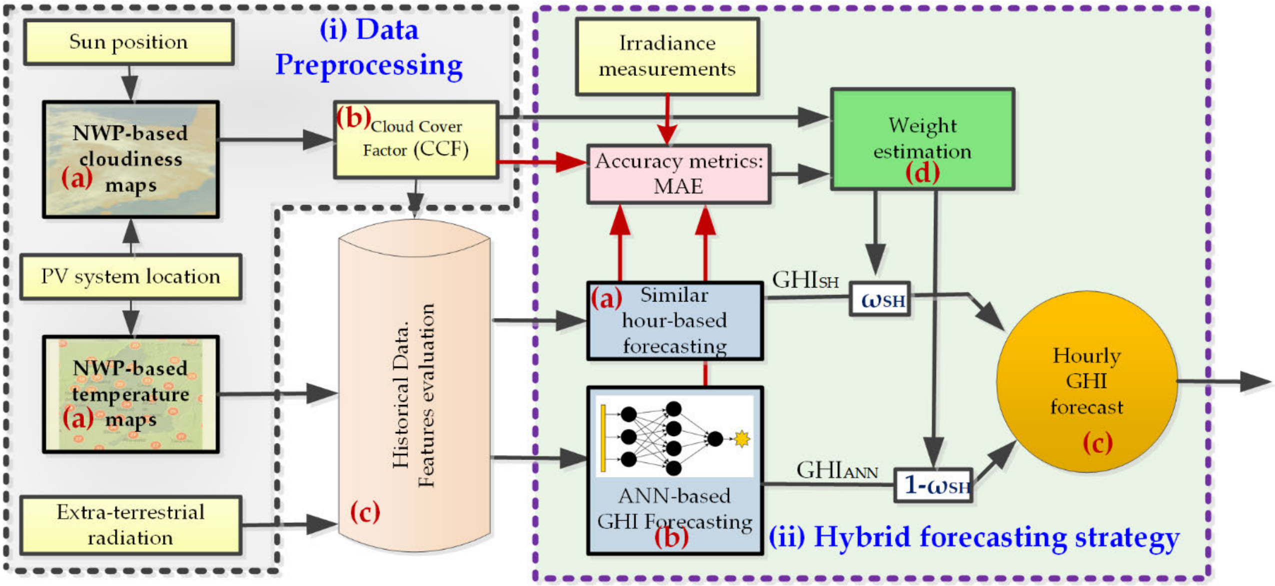

FIGURE 1. Block diagram of the forecasting approach, which consists of two parts: (i) a data pre-processing stage and (ii) the hybrid forecasting approach. The forecasting strategy is based on ANNs and a novel similar hour-based algorithm. The final forecast is obtained by dynamically weighting the outputs as a function of the type of the day.

pre-processing are presented. Section IV analyses in depth the algorithms involved in the hybrid approach. The experimental results are presented in Section V. Finally, some conclusions are drawn in the final section.

II. IRRADIANCE FORECASTING APPROACH. GENERAL DESCRIPTION

An important feature of irradiance forecasting models is that, in general, they rely on extensive historical dataset. However, when a VPP is to be operated in a cost-efficient manner at its initial stage or when a node is first integrated in an existing VPP, the lack of data reduces the accuracy of the day-ahead estimation of the irradiance and, as a result, the accuracy of the power forecasts. This leads to uncertainties, which result in financial penalties imposed by the grid operator. NWP-based GHI forecasts have proved to be a tool for indirect solar power prediction. Furthermore, when it comes to VPPs, an aggregation of small-scale PV installations makes it crucial to implement an EMS, which must include accurate forecasts such as, for instance, the NWP-based GHI forecasts for each location or site. However, this carries a cost, which depends on the number of sites taking part in the VPP. In order not to incur costs, which would cause a decline in profits, free access NWP-based cloudiness and temperature maps are used in this paper. This information along with known parameters such as the sun position, the location of the PV sites and the extraterrestrial radiation, constitute the inputs of the GHI forecasting hybrid approach proposed in this paper.

Fig. 1 shows the approach, which is based on ANNs and a novel similar hour-based algorithm. The outputs of both techniques are dynamically weighted according to the type of the day and some accuracy metrics. Thus, uncertainties in the 24-hour ahead final GHI forecasting, are reduced. The forecasting method consists of two parts: (i) a data pre-processing stage; and (ii) the hybrid forecasting approach.

i. The first part has 3 steps: (a) new data acquisition and transformation to provide the input data of the algorithm; (b) CCF calculation; and (c) data merging within the historical dataset collected. In step (a), to manage the ESS of some sites at night, weather forecast maps are downloaded at 22:00 hours from [24], gathering information on the day-ahead weather variables such as area of cloud cover and temperature. To turn the information from the maps into numerical data a transformation process is required. In step (b) the lack of an extensive dataset, especially at the earlier stages of the VPP operation, makes it essential to optimize the data available in order to provide the forecasting algorithms with the most relevant and correlated information. Hence, the data pre-processing stage becomes crucial. The 24-hour-ahead cloud cover maps are used to define a parameter, referred in this paper as Cloud Cover Factor (CCF), Section III-A, which is also based on the sun position. The CCF contains information about the shadows on the PV installation generated by a particular cloud area. In general, the shadowed area will be larger than the corresponding cloud area. Secondly, temperature maps are used to obtain the temperatures for the 24-hour target forecasting period. These temperatures can be validated by using both real measurements taken in the PV installation and those from the closest ground-based meteorological stations. Finally, the extra-terrestrial radiation gives information about the radiation at the top of the Earth's atmosphere.

In this paper it is assumed that the determining factor for the loss of radiation is the CCF, disregarding the influence of other factors such as the air molecules, the distance the solar radiation has travelled through the air mass, etc., which are assumed to modify the GHI in lesser proportion. This clearly introduces an estimation error the predictable effect of which is somewhat mitigated by giving more importance to those days closer to the target day. This is achieved by considering the temperature, since it is a parameter that depends on the season of the year. Finally, in step (c), once the information of the day-ahead weather variables has been processed, the historical dataset is updated with this information and the forecasting strategy can then be implemented.

ii. The second part focuses on the forecasting strategy and has 4 steps: (a) similar hour-based forecasting method; (b) artificial neural network forecasting approach; (c) hybrid forecasting strategy; and (d) weight estimation. In step (a) the novel method referred to in this paper as similar hour-based forecasting, Section IV-A, is implemented. It is based on the traditional method of similar days. The similar hour-based method performs reliably dealing with the information extracted from a reduced historical dataset. In step (b) the ANN, Section IV-B, forecasts from the same dataset. However, ANNs generalize better when an extensive historical dataset is available. In step (c) both methods are combined, thereby providing an accurate forecast irrespective of the dataset size. This makes the efficient management of a VPP possible from the very beginning or when a new VPP node is added.

The combined GHI forecasting output is the weighted sum of the individual GHI forecasting outputs of the two methods explained above (d). The weights depend on the type of the day, i.e. sunny, cloudy and overcast, and the Mean Absolute Error (MAE). Metrics based on mean and squared values have been selected to assess the performance accuracy because they are the most commonly used indexes in solar radiation techniques [36]. Error mean values are used for selection purposes, to minimize the forecasting error of each node comprising the VPP, irrespective of the length of the database considered, instead of penalizing atypical values. It is worth mentioning that results did not change excessively with the inclusion of atypical values. The type of the day is defined by means of the CCF, which shows to what extent a cloud area on the NWP-based cloudiness maps creates shadows on the PV installation.

The weights are calculated by using (1) where d_s, d_c, and d_o, are mutually exclusive flags which can take the values of either 0 or 1, representing with a value of 1, the type of day determined by the CCF, i.e. sunny, $d_s = 1$, cloudy, $d_c = 1$, or overcast, $d_o = 1$, and ω_d is the value of the weights which minimize the MAE in past hybrid predictions obtained for this type of day. These weights are updated daily by incorporating the latest and most up-to-date information from the dataset, thereby improving the accuracy of forecasting results.

$$\begin{aligned} \omega_{SH} &= d_s\omega_{d_s} + d_c\omega_{d_c} + d_o\omega_{d_o} \\ \omega_{ANN} &= 1 - \omega_{SH} \end{aligned} \tag{1}$$

III. DATA DESCRIPTION AND PRE-PROCESSING

As mentioned above, the inputs to the algorithm are based on weather forecasts, provided by the AEMET at different spatial and temporal scales, and the extra-terrestrial radiation, E, which is deterministic and can be evaluated by using known expressions. For instance, Duffie and Beckman's equation was considered to determine the extra-terrestrial radiation. Nevertheless, other expressions available in the literature [37] are equally accurate.

The weather forecasts are based on the NWP model HARMONIE-AROME. This model is commonly utilized for weather forecasts in Spain and other European countries [38]. NWP models include GHI and DNI forecasts, both being necessary to model irradiance on the inclined surfaces of the solar panels. However, the cost of purchasing this data is a deterrent for small-scale PV systems. Other weather forecasts include cloudiness, temperature, pressure and wind, all of them in the shape of weather maps. Cloudiness forecasts contain relevant information regarding irradiance. To turn this information into numerical values some data pre-processing must be applied. The term used in this paper for these numerical values is the above-mentioned cloud cover factor (CCF), in order not to confuse it with other parameters such as cloudiness index, which is modelled in a different way. Studies which rely on images from satellite or ground level cameras to find the shadows cast by the clouds already exist [39]–[42]. In this regard, the CCF provides the same information but without cost.

A. CLOUD COVER FACTOR EVALUATION FROM CLOUDINESS FORECAST MAPS.

The CCF is dimensionless and represents, in the context of the weather maps, the amount of cloud cover per pixel in each cloudiness forecast map, showing a negative correlation with the GHI, being 0 when the sunlight is not blocked by clouds and 1 when the sun is totally covered. At a particular time of day, e.g. 22:00, the 24 NWP-based cloudiness images, representing the cloudiness forecast for the next 24 hours, are downloaded from the AEMET web service. Fig. 2 represents a zoom area of the cloudiness forecast for the Community of Madrid (centre of the map) at 16:00 on March 1st, 2020. This image was downloaded on February 29th, 2020. The colormap on the right represents the percentage of cloudiness. The spatial resolution in the map is given by the pixel size in the image, being represented by a square with sides approximately equal to 2.5km.

Another important parameter for the CCF calculation is the cloud height. Unfortunately, this parameter cannot be obtained from Fig. 2 and some data pre-processing must be

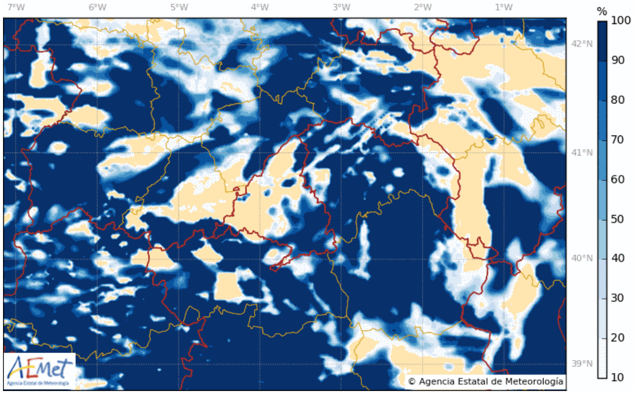

FIGURE 2. NWP-based cloudiness forecast map for the Community of Madrid (center of the map), from the spanish website, ©AEMET. Values range from 0% (absence of clouds) to 100% (heavy clouds).

done to identify those clouds that prevent the sun radiation from reaching the site, i.e. the clouds between the sun and the site. Therefore, both the cloud location and the sun's position are required. Fig. 3 shows the hourly position of the sun at the spring equinox for a site located in the Northern Hemisphere, and the most relevant variables used for the CCF evaluation. For the site-related pixels in the map, the aim is to quantify the CCF at a particular time of the day. Considering that the site location is known (X, Y), those pixels in the map covered by the clouds (P_X, P_Y) can be worked out, as a function of the cloud height (H), by using the following equations:

$$P_X = X + R_X \approx X + \frac{H}{S}\frac{sin\,(\psi)}{tan\,(\alpha)} \qquad (2)$$

$$P_Y = Y + R_Y \approx Y + \frac{H}{S}\frac{cos\,(\psi)}{tan\,(\alpha)} \qquad (3)$$

where R_X and R_Y represent the relative position of the pixel with respect to the site, S is the spatial resolution in the map ($2.5km$), and α and ψ are the elevation and azimuth angles, respectively.

Since the cloud height cannot be extracted from the cloudiness forecast, (2) and (3) are evaluated with the greatest cloud height considered (15 km) [43]. By doing so, the cloudiness values of the pixels on the way from (X, Y) to (P_X, P_Y) are evaluated and the average of those values is stored.

However, the CCF can vary widely over time when clouds are present on the map. To reduce this variation, a smoothing procedure based on a parameter called uncertainty threshold (u) is applied. This variable is used to expand the selected area in every direction, selecting a larger area on the map to obtain a greater number of pixels that provides a smoother variation of CCF values and enables the identification of the type of the day. The value of u is selected through an iterative process in which the threshold is gradually increased, i.e. the selected area on the map is expanded. The process terminates when the CCF variation is smooth and its value is consistent with the GHI measured. The value of u that minimizes the forecasting error was set to 8 pixels, covering an area of 20 km.

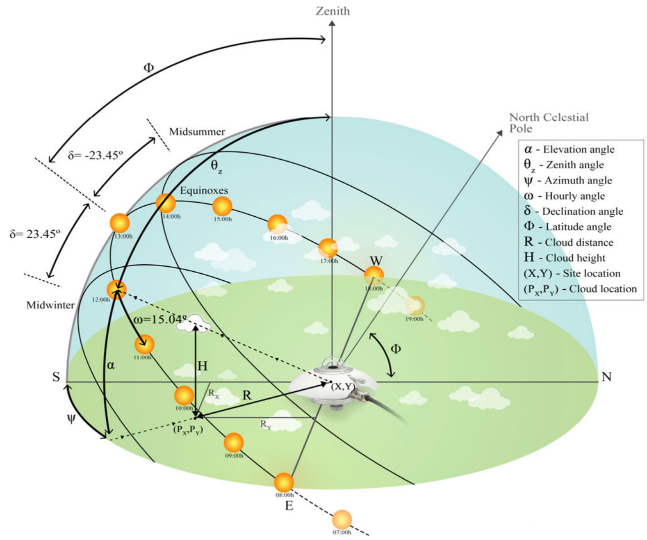

FIGURE 3. Relevant variables for the CCF assessment with respect to the sun position and the site location.

IV. HYBRID APPROACH FOR THE HOURLY GHI FORECASTING

In this section, the similar hour-based and ANN-based methods comprising the hybrid approach for GHI forecasting are explained.

A. SIMILAR HOUR-BASED APPROACH

The underlying behaviour behind meteorological events is difficult to model although it can be assumed that weather conditions repeat themselves in time. Therefore, searching for similarities is the key to predicting when certain weather conditions will repeat in the future.

A similar day-based approach intrinsically considers the weather conditions of a whole day to forecast the GHI in a moment of the day. Since the weather conditions do not follow a marked trend during the day, it seems perfectly reasonable to use the meteorological variables forecast at the target hour for similarity matching. Furthermore, if the candidates for the similarity study also depend on the extraterrestrial radiation, which replaces the conventional time variables for the day and hour, the number of potential hours to be considered is significantly increased.

In the model proposed in this paper, for similarity matching, a time-window of three hours around the forecast hour is considered, because the distance travelled by the sunlight through the atmosphere depends on the position of the sun in the sky (elevation and azimuth) which, in turn, influences in the GHI loss variation Therefore, the same hour as that of the target hour along with the adjacent hours, i.e. the previous and the following one, are extracted from each day in the historical dataset since these hours are similar in terms of the sun's position in the sky. The Sun position for a particular hour progressively changes as the days go by, becoming closer to the Sun position for the adjacent hours. However,

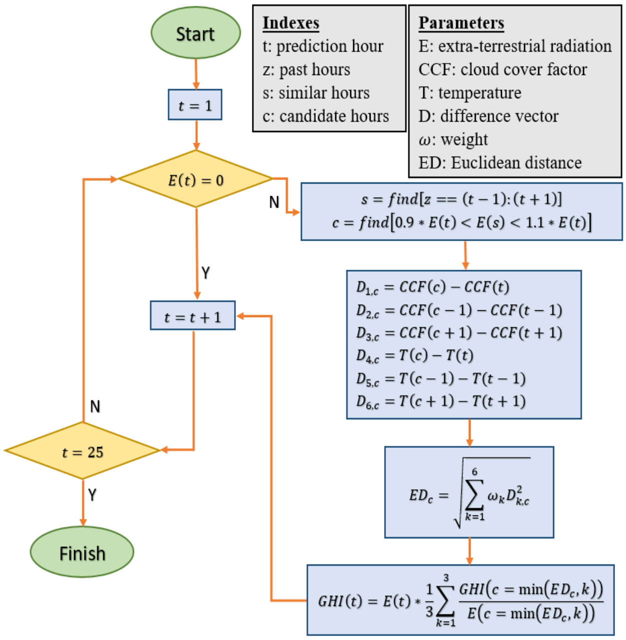

FIGURE 4. Flowchart of the proposed similar-hour based forecasting algorithm for a day-ahead prediction.

this strategy requires the removal of the hours with highly dissimilar values for the extra-terrestrial radiation. To that end, only the hours with values for the extra-terrestrial radiation, within a range of ±10% from that of the forecast hour are selected as potential candidates for similar hours. This strategy is referred to as similar hour-based approach in this work, and it makes a significant difference with respect to the day-based version. This is one of the main contributions of this paper since, to the best of the author's knowledge, this is the first time this approach has been used for irradiance forecasting. This algorithm, in contrast to the similar day-based methods, uses extra-terrestrial radiation to filter the most important time instants for the prediction, and delivers outstanding results in the early stage of the VPP node. Furthermore, the accuracy of this method is improved as new VPP nodes are aggregated, reducing the global error to a greater extent compared to other forecasting techniques.

The similar hour-based methodology is depicted in the flowchart of Fig. 4. Once the candidate hours (c) have been chosen from the historical dataset (z), the algorithm searches for similarities with the forecast hour (t) in terms of the CCF and temperature (T). Temperatures annually vary from minimum values in winter to maximum values in summer. Needless to say, the further back in time the potential candidates for similar hour are located, the less likely it is that the hours become similar hours.

The Euclidean distance (ED) is used as a measure of similarity. Firstly, the difference vectors (D) are obtained by evaluating the differences between the meteorological parameters, i.e. the CCF and the temperature (T), for the forecast hour (t) and those from the candidate hours (c). As justified above, the adjacent hours, i.e. $(t-1)$ and $(t+1)$, to the forecast hour (t) for the difference vector (D) calculation are also considered. As a result, a total of 6 variables are evaluated for the difference vectors (D), whose contribution to the similarity matching process is not, however, the same. Therefore, in a second step, a set of weights (ω), representing the relative importance the similar hour-based algorithm gives to each difference vector (D), is used. The selection of the weights (ω) is based on the principle of minimum error for the historical dataset of past forecasts, which are updated daily. Finally, the Euclidean weighted distance (ED) is calculated to find the most similar hours in the past to the forecast hour (t). Since NWP models have an inherent error that can adversely affect the forecast accuracy, the irradiance of the three candidates with the smallest Euclidean distance (ED) are averaged and taken as the final solution. Before the average can be calculated, an adjustment in the values of the irradiance of the three candidates is necessary. This adjustment is proportional to the difference between the extra-terrestrial radiation (E) for the chosen hour and that of the forecast hour (t). The algorithm iteratively repeats the similarity matching as long as the extra-terrestrial radiation (E) is greater than zero for the forecast hour (t).

B. ARTIFICIAL NEURAL NETWORK FORECASTING

The second forecast method making up the hybrid approach consists of an ANN, which produces accurate forecasts from extensive datasets. This clearly complements the similar hour-based method, which yields better results for a reduced dataset for which the ANN performance is only moderate. In this work, a multilayer perceptron (MLP) has been developed due to its simplicity and good overall performance. This type of ANN is the most widely used technique for day-ahead irradiance forecasting [44], excluding RNN because the time horizon is too large for a proper forecast using the observations as input [45] and the length of the dataset is too short to obtain patterns in a day-ahead forecasting [32].

The neural network has three layers: (i) an input layer has 7 neurons one for each predictor variable, namely, the CCF and the temperature at the time $(t-1)$, t and $(t+1)$, being t the forecast time, and the extra-terrestrial radiation; (ii) a hidden layer with 10 neurons which minimizes the forecast error by using a logarithmic sigmoidal activation function; and (iii) and output layer with one neuron with a linear transfer function which provides hourly GHI forecasting values.

The dataset comprises data from December 4th, 2019 to May 31st, 2020. To simulate the real scenario of the initial stage of a VPP, the ANN is trained daily with the historical dataset collected to the date under consideration. For operational purposes, the minimum amount of days in the dataset is established as 7 and the training and validation process is repeated every day. Consequently, the training dataset is variable and increases as the VPP operation time increases and more data is available.

The number of hidden layers is evaluated through cross-validation using the dataset available. Adding more layers

TABLE 1. MLP ANN characteristics of the hybrid method forecasting.

Parameter	MLP
Inputs	T, CCF, E
Output	GHI
Number of layers	3
Input neurons Hidden neurons (one layer) Output neurons	7 10 1
Hidden layer activation function	logistic sigmoid
Output layer activation function	linear
Objective function	MAE
Learning algorithm	Levenberg-Marquardt
Minimum gradient	1e-4
Maximum iterations	500

does not yield better results, but instead increases computational time. The Levenberg-Marquardt (LM) algorithm is used for the ANN learning process, because it ensures greater accuracy in comparison to other alternatives such as LM, Bayesian Regularization (BR) and Scaled Conjugate Gradient (SCG).

A sensitivity analysis of the ANN has also been carried out, to determine the relationship between the inputs and the output. As is to be expected, the extra-terrestrial radiation provides the greatest amount of information. The CCF is the second most important input, followed by the temperature (T). Temperature measured at time instants (t+1) and (t-1) are also relevant on account of the different patterns during mornings and evenings: depending on the temperature gradient, the ANN can recognize both periods of time.

To achieve better generalization, a popular technique in the context of short dataset is implemented, [32], [46]. It consists in training several independent ANNs for the same target variable. The average of the outputs of the set of independent ANNs is taken as the final prediction. Assuming that the error follows a normal distribution $N(\mu, \sigma) \sim N(0, 1)$, the average of the output values of up to 30 independent ANNs allows the prediction to be correctly validated. The characteristics of the ANN are summarized in Table 1.

C. COMBINING THE SIMILAR HOUR-BASED ALGORITHM WITH ANN-BASED FORECASTING

Once the forecasting methods have been introduced, the hybrid approach is explained in this section. The hybrid method consists in evaluating the final prediction as a weighted value of the individual forecasting outputs as shown in (4). The weights are determined as a function of the type of the day (sunny, cloudy and overcast), which depends on the values of the CCF at the forecast hour. By using the k-nearest neighbors (k-NN) algorithm, the days are classified taking into account the CCF and the corresponding set of weights are associated with the type of day. This simple classification algorithm allows the weight selection to be carried out automatically and independently for each site, selecting the set of weights that minimizes the MAE of previous forecasts.

$$GHI = \omega_{SH} GHI_{SH} + (1 - \omega_{SH}) \, GHI_{ANN} \tag{4}$$

The weights are updated daily for each type of day to optimize the final forecast. The historical data for the weight evaluation consists of up to a 2-month slide window with the most recent data. There are two reasons behind this value for the window width: (a) ANN performance improves as more data is available, which means that previous forecast should be disregarded; (b) it is expected that the strong seasonality in the weather directly influences the weights.

The novelty of the hybrid approach lies in the development of a model which has the ability to adapt itself to the amount of historical data. As previously stated, for a reduced dataset, the similar hour-based method outperforms ANN-based strategy, whereas the converse applies for larger datasets. Combining both methods, therefore, an accurate prediction can be obtained irrespective of the size of the dataset.

Initially, the similar hour-based forecasting output has a great influence on the prediction because this method considers extra-terrestrial radiation to filter the most important time instants for the prediction. When more data is available, the ANN-based forecasting gains more influence. In this way, a smooth transition of the weights is achieved.

V. RESULTS

This section presents the results obtained from the implementation of the similar hour-based and hybrid GHI forecasting strategies in two different scenarios: firstly, the approach is applied to an experimental setup (a real PV installation) that plays the role of a VPP node; and secondly, an aggregation of different PV installations in the shape of ground-based meteorological stations making up a VPP, is considered. The results from using other techniques, such as the persistence model, the similar day-based approach and neural networks, are also included for comparison purposes, proving the effectiveness of the proposed approaches.

A. EVALUATION OF THE HYBRID FORECASTING APPROACH FOR A REAL VPP NODE

To validate the proposed algorithm in the context of a single VPP node scenario, measurements taken from a recently installed photovoltaic facility located at the Polytechnic School of the University of Alcalá (Spain) are used. These measurements, mainly comprising GHI and temperature values, were recorded during the period between December 4th, 2019 to May 31st, 2020, and constitute the 6-month period of historical dataset for the algorithm validation. The first forecast is provided by using only a week of the historical dataset, which allows GHI predictions to be made from the earliest stages of the VPP node operation. The 24-hour ahead

GHI forecasting process is repeated on a daily basis, updating the data used in the process, with the collected data of that day. This process is carried out until all the data in the historical dataset is used. In this way, the performance of the prediction algorithm is assessed daily starting from the second week of the PV system operation until the 6-month period is covered.

To analyse the accuracy of the prediction algorithm, the overall error is calculated using the following performance indicators:

$$MAPE = \frac{\frac{1}{T}\sum_{t=1}^{T}\left|Y_t - \hat{Y}_t\right|}{\frac{1}{T}\sum_{t=1}^{T}\mathrm{Y_t}}100[\%] \tag{5}$$

$$NRMSE = \frac{\sqrt{\frac{1}{T}\sum_{t=1}^{T}\left(Y_t - \hat{Y}_t\right)^2}}{\frac{1}{T}\sum_{t=1}^{T}\mathrm{Y_t}}100[\%] \tag{6}$$

where Y_t is the measured data, $\hat{Y}_t$ is the forecast value and T is the length of the time series. MAPE shows the normalized average error between the measurements and the forecast, while NRMSE represents the normalized square error. The normalisation parameter used is the average of the measurements. Normalized indicators are used due to the fact that they allow a fair comparison of the results obtained as the validation is developed, since the dependence on the magnitude is removed. The use of both indicators is justified on the grounds that NRMSE is more sensitive to outliers than MAPE, which allows for a more comprehensive comparative study to be carried out.

In order to validate the benefits of the proposed forecasting strategy, described in section IV-C, a comparison is made with other widely used forecasting methods, as well as with the proposed similar hour-based approach. The following methods are analysed:

- Persistence model: it is the simplest method which assumes that the 24-hour ahead GHI forecast is equal to the GHI measurements taken the previous day [32].
- Similar day-based approach: this method calculates the difference vectors for the CCF and the temperature considering the weather forecasting of the day to be predicted and the previous 14 days within the historical dataset. The selection of the number of days is not arbitrary and aims at minimizing the error. The Euclidean distance of all the difference vectors is then calculated for each of the 14 days and the day that minimizes this distance is chosen as the following day's GHI prediction [47], [48].
- Proposed similar hour-based algorithm, which is described in detail in Section IV-A and separately implemented without hybridization.
- ANN-based forecasting approach, described in Section IV-B, and individually evaluated.

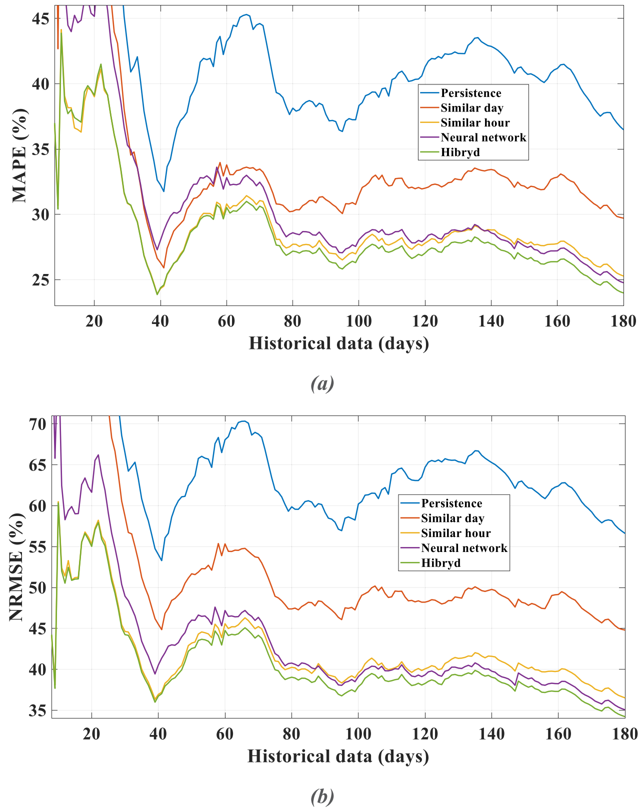

FIGURE 5. Forecasting errors of the methods under study (persistence, similar day, similar hour, neural network and hybrid model proposed) for the Alcala University site in terms of (a) MAPE and (b) NRMSE.

- Proposed Hybrid approach, described in detail in Section IV-C.

Fig. 5 depicts the forecast errors, using the MAPE and NRMSE indexes, depending on the days from the historical dataset employed. In order to improve the graph visualization, the highest errors made by certain forecasting methods when implemented for a reduced amount of historical data, are neglected. The maximum values in the neglected period for the persistence model, and similar day-based and ANN-based approaches are for the MAPE = [96.8 66.2 69.7] and for the NRMSE = [126.2 116.4 85.1].

From the figure it can be seen that the persistence method, on account of its simplicity, is the one that introduces the greatest error. The similar day-based forecast significantly improves the persistence prediction achieving a similar degree of accuracy to that of the ANN-based forecast for a reduced amount of historical data. However, as more data is available, the performance enhancement of the ANN is noticeable, especially with respect to that of similar day-based forecasting. The proposed similar hour-based method performs much better than the other methods in the case where little historical data is available. As the amount of historical data increases, it can be appreciated that its performance keeps improving relative to the similar day-based approach, and with similar accuracy to that of the ANN-based

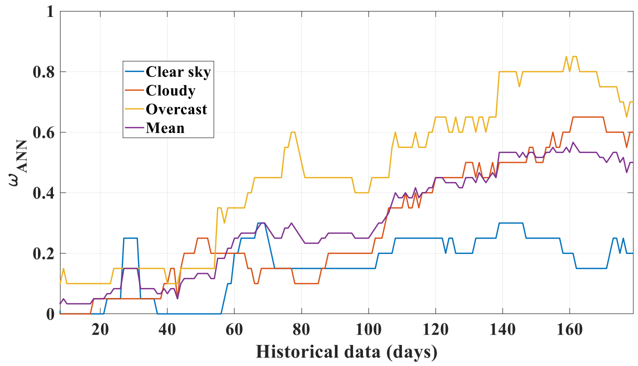

FIGURE 6. Weights used in the hybrid method for the ANN as a function of the number of days in the historical dataset, for the Alcala University site. It can be seen that the weights progressively give more importance to the ANN output, following a marked trend.

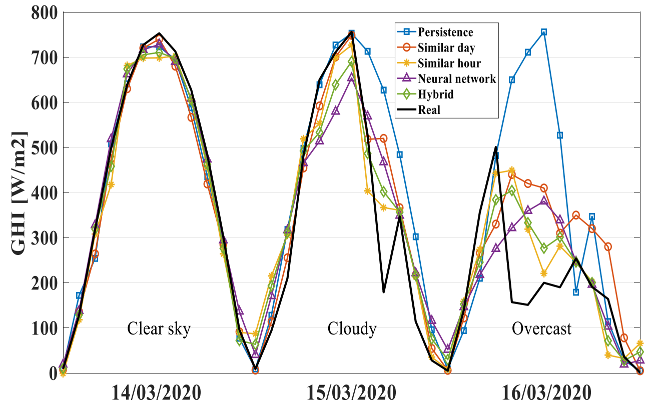

FIGURE 7. GHI forecasting values at the Alcala University site for the different methods, over three consecutive days, showing different weather conditions.

method. On the other hand, the ANN-based forecasts deliver better results than the similar hour-based method when a sufficiently extensive historical dataset is available, this being the reason that the ANN can generalize better. Finally, the hybrid method presented in this paper practically outperforms all the previous ones irrespective of the amount of data, because it manages to combine the advantages of neural networks and the similar hour matching.

The proposed hybrid method has been adjusted for different weights depending on the type of day as described in section 4.3. These weights evolve as the historical record increases as shown in Fig. 6.

Fig. 6 demonstrates how, as the historical dataset increases, the neuronal network carries more weight in the final prediction. This is justified by analysing Fig. 5(a), in which the accuracy of the ANN-based technique compared to that of the similar hour-based approach, gradually improves as the amount of historical data increases. This effect is more significant on cloudy and overcast days, since on clear sky days the performance of the similar hour-based technique is slightly better than that of the ANN-based approach. This

evolution is noticeable by analyzing the mean weight of the three day types in which the initial weight associated to the ANN output starts from approximately $\omega_{ANN} = 0.04$ reaching up to approximately $\omega_{ANN} = 0.51$ when the total historical dataset is completed.

Finally, Fig. 7 shows the GHI forecasting output of each method for three consecutive days between 14th and 16th March 2020. These days have been deliberately chosen because they represent the three types of day considered in the hybrid method. Moreover, in this case, approximately half of the historical dataset is employed, 102 days. It is observed that the error produced by all the forecasting methods increases as the cloudiness grows. This is because cloudy days are the most complicated to forecast since clouds have a strong impact on the GHI and it is difficult to predict their exact location for a 24-hour horizon. However, it can be seen from the results, that with the proposed hybrid strategy a considerable improvement in the forecast accuracy is achieved.

B. EVALUATION OF THE HYBRID FORECASTING APPROACH FOR AN EMULATED VPP

The potential of the proposed forecasting algorithms having already been demonstrated for a single photovoltaic installation, i.e. a single VPP node, in this section additional improvements are described for a set of photovoltaic facilities, grouped under the concept of VPP. As no additional photovoltaic installations are currently available, 6 ground-based meteorological stations located in the Community of Madrid in Spain (see Fig. 8) are used to emulate the new nodes. This is possible because meteorological stations publish, free of charge, all the required data utilized in the forecasting approach. The location of the stations is depicted in Fig. 8.

As in the previous section, the MAPE and NRMSE indexes are used to quantify the accuracy of the forecast outcomes for all the methods previously presented. The main difference is that in this case, once the GHI forecasts are produced for each station, all the VPP GHI variables are calculated by adding the corresponding GHI forecasts from each station, including the PV installation. In this way, the individual GHI measurements taken at each station, i.e. node of the VPP, are compared to the total GHI forecast.

Fig. 9 displays the evolution of the GHI forecasting error, for the ensemble of stations, quantified by the MAPE and NRMSE indexes. As depicted in Fig. 5, the graphs do not show the highest errors made by certain methods for the reason stated above. The maximum values in this omitted area for the persistence model, and for the similar day-based and ANN-based approaches are $MAPE = [93.263.5\ 62.8]$ and $NRMSE = [119.7\ 110.774.5]$. As in the case of a single installation, it can be seen that the persistence method exhibits the poorest performance followed by the similar day-based approach. The ANN-based method improves as the amount of historical data increases. In this case, however, it is not able to outperform the proposed method based on similar hours, irrespective the number of the days in the historical dataset. The novel methods proposed in this paper, i.e. similar hour-based and hybrid, achieve the highest accuracy regardless of

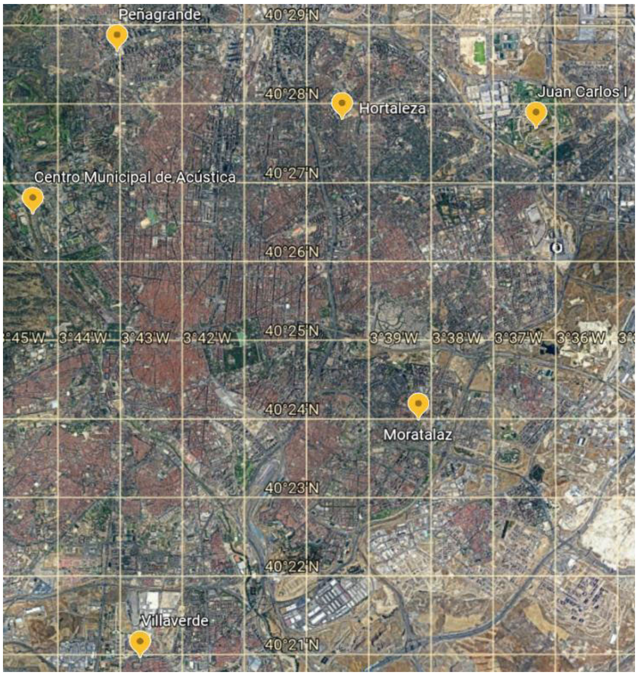

FIGURE 8. Location of the different ground-based meteorological stations in the Community of Madrid used in the study.

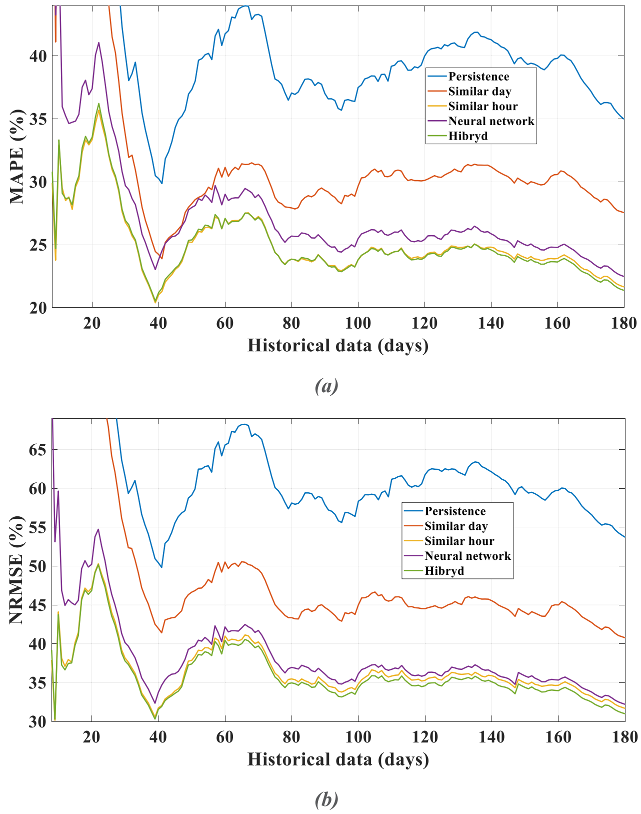

FIGURE 9. Forecasting error of the methods under study (persistence, similar day, similar hour, neural network and hybrid model proposed) for the VPP in terms of (a) MAPE and (b) NRMSE.

the number of days in the dataset, with the exception of the hybrid method, in which accuracy slightly increases as the historical dataset builds up.

To analyze the improvement of the proposed forecasting algorithms within the VPP scheme, the results obtained in each node are presented in Table 2. It can be appreciated that all the nodes in the VPP based on the meteorological stations, have similar performance to the one of the PV installation shown in Section V-A, in which the method based on similar hours introduces higher forecast error, in terms of MAPE and NRMSE, than the method based on ANNs when there is enough historical data available. However, when the similar hour-based GHI forecast for the entire VPP is calculated, the deviations from the GHI actual values, in the individual predictions for each node, tend to be compensated to a greater extent than when the ANN-based method is used.

This is because the method based on similar hours generalizes as a function of the node being considered and, consequently it can be assumed that the forecast errors follow different distributions. This makes certain errors partially compensate with each other when the GHI forecasts of the ensemble of VPP nodes are added. In contrast to the similar hour-based algorithm, in the ANN-based model the relationship between the inputs and the output identifies similar GHI patterns irrespective of the VPP node and, as a result, no error compensation takes place. The MAPE reduction of the similar hour-based strategy comparing the arithmetic mean of the 7 VPP nodes and the whole VPP is 3.31%, and in the case of NRMSE is 5.40%. As for the neural networks the reduction is 1.58% for the MAPE and 2.53% for the NRMSE. In the hybrid method, this reduction ranges between the two previous values as expected, 2.38% for the MAPE and 3.75% for the NRMSE.

Fig. 10 presents the average weight of all the nodes considered according to the historical dataset and the type of day. Although this average weight is not directly applied, because the set of weights for each VPP node are calculated individually, it provides an insight about how the weights for the different nodes evolve. It can be appreciated that this evolution is very similar to that of a single node shown in the Fig. 6. The mean weight for the three day types and the 7 VPP nodes evolves from an initial weight of $\omega_{ANN} = 0.10$ to approximately $\omega_{ANN} = 0.60$ when the total historical dataset is completed.

Finally, Fig. 11 shows the GHI forecasting for the entire VPP and for each method considering three days of the historical dataset: from 14th to 16th March 2020. These days are representative of the three types of day considered in the hybrid method. As in the case of one VPP node, it can be seen that the error produced in all the forecasting methods increases as the cloudiness grows. However, it can be observed to what extent, better forecasts are obtained with the proposed methods.

TABLE 2. Quantification of MAPE and NRMSE after 180 days of historical data.

Method	Sites	University	Ctro. Mpal. de Acustica	Hortaleza	Juan Carlos I	Moratalaz	Peñagrande	Villaverde	Mean	**VPP**
Similar hours	MAPE (%)	25.27	25.40	25.71	24.28	25.00	24.63	24.37	24.95	**21.64**
	NRMSE (%)	36.51	37.26	39.15	36.60	36.45	36.52	37.11	37.09	**31.69**
ANN	MAPE (%)	24.76	24.63	25.85	24.09	24.46	24.48	24.04	24.06	**22.48**
	NRMSE (%)	35.05	35.15	37.18	34.71	34.76	35.38	34.74	34.74	**32.21**
Hybrid	MAPE (%)	23.98	23.92	24.71	23.18	23.67	23.53	23.27	23.75	**21.37**
	NRMSE (%)	34.21	34.57	36.90	34.38	34.12	34.42	34.59	34.74	**30.99**

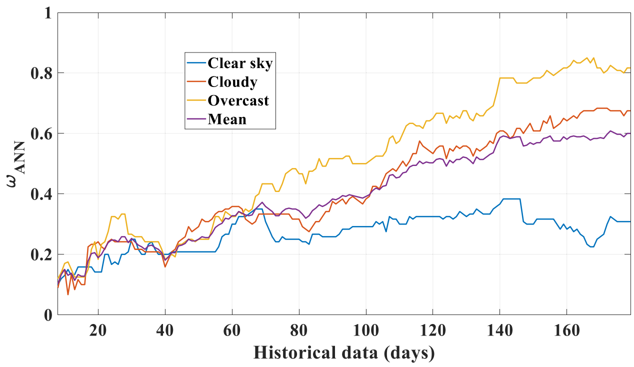

FIGURE 10. ANN mean weight for the VPP as a function of the day type and the historical data. It can be seen that weights give progressively more importance to the forecast provided by the ANN.

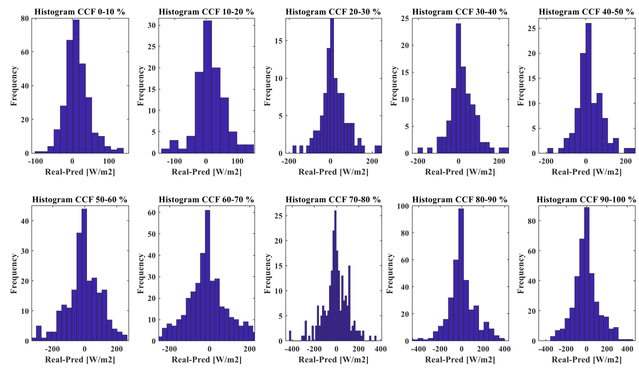

FIGURE 12. Distribution of the error for every subset considered. To create prediction intervals in the forecasting strategy, a Laplace distribution is assumed.

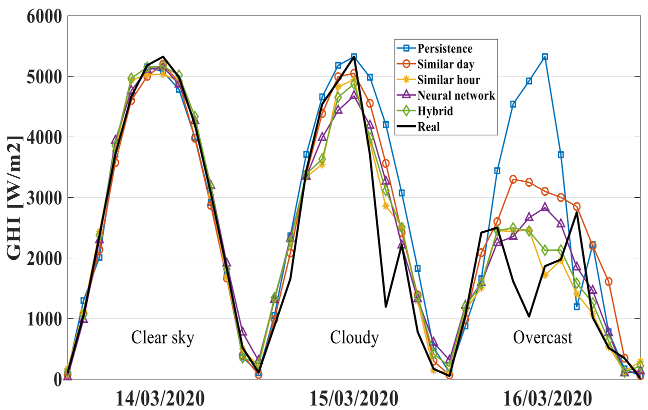

FIGURE 11. GHI accumulated forecasting in the VPP for the different methods and for three consecutive days, showing different weather conditions.

TABLE 3. Prediction intervals (p_s) for each subset and for the whole dataset, and their PICP.

CCF	MAE $[W/m^2]$	p_s $[W/m^2]$	*PICP*
0 - 10 %	34.02	±31.17	0.63
10 - 20%	44.08	±40.39	0.61
20 - 30 %	54.73	±50.15	0.60
30 - 40 %	58.52	±53.62	0.62
40 - 50 %	72.41	±66.35	0.58
50 - 60 %	80.87	±74.10	0.59
60 - 70 %	87.18	±79.88	0.55
70 - 80 %	89.81	±82.29	0.59
80 - 90 %	92.21	±84.49	0.60
90 - 100 %	91.67	±84.00	0.58
WHOLE DATASET	75.96	±69.60	0.62

C. UNCERTAINTY QUANTIFICATION

It is very important to specify a probabilistic range for the predictions, in order to assess the degree of uncertainty. To this purpose, in this section, statistical prediction intervals are considered based on the work carried out in [49].

Firstly, the dataset is split into 10 subsets as a function of the CCF. Looking at the error distribution of the hybrid-based forecast in Fig. 12, a Laplacian distribution can be reasonably assumed for each subset. Secondly, under this assumption, a prediction interval for each subset is defined, $I_{pred} \pm p_s$, in terms of the MAE, and the percentile p of probability $(1-s)$ is considered, knowing that $p_s = \pm MAE.\ln(2s)$ for a Laplacian distribution.

In this particular case, the reliability of the prediction interval under a confidence value of 60%($s = 0.2$), is evaluated. The prediction interval, p_s, which is determined as a function of the MAE of each subset, is then calculated. With this interval, the Prediction Interval Coverage Probability (PICP) [50], can be worked out. The PICP indicates the percentage of values that are inside the interval, and it needs to be close to the confidence level.

$$PICP = \frac{1}{T}\sum_{t=1}^{T}\epsilon_t, where\epsilon_i = \begin{cases} 1 & if\ x_i \in [\mathrm{L_i}, \mathrm{U_i}] \\ 0 & if\ x_i \notin [\mathrm{L_i}, \mathrm{U_i}] \end{cases} \quad (7)$$

In Table 3, it can be observed that the PICP is close to the confidence level for every subset. It can also be appreciated that the prediction interval increases with the presence of clouds, showing that overcast days are the most difficult days to forecast.

VI. CONCLUSION

Solar irradiance forecasts are of paramount importance for the integration of PV systems in a VPP in an effective way. However accurate irradiance predictions generally rely on extensive datasets, which are not always available when a VPP begins operating or when a new VPP is first integrated. Furthermore, data access usually carries a cost, which is driven up as the number of VPP increases leading to a decline in profits. There is not a simple way to overcome these limitations with only one approach which performs efficiently irrespective of the dataset size. For this reason, this paper presents a hybrid approach comprising two methods based on similar hours and ANNs. The outputs of both forecasting methods are dynamically weighted, according to the type of the day (sunny, cloudy and overcast) and the MAE. The proposed forecasting approach uses temperature and cloudiness forecast maps freely generated by the AEMET via NWP along with irradiance measurements obtained from both a real PV installation located in the Polytechnic School of Alcala University and a group of different ground-based meteorological stations operating in the Community of Madrid (Spain). Both, the similar hour-based approach and the hybrid method have demonstrated better performance than widely employed forecasting techniques, namely persistence method, and similar day-based and ANN-based approaches, when limited historical data is available. For a 7-node VPP configuration and for a 6-month period of historical data, a MAPE of 21.64% and a NRMSE of 31.69% for the similar hour-based technique, and a MAPE of 21.37% and a NRMSE of 30.99% for the hybrid strategy are obtained.

Under a reduced historical dataset, the results show that the proposed similar hour-based method produces the best forecasts relative to those obtained by the ANN-based approach. For one-month and two-month datasets the mean error is reduced by 16.32% and 9.07% respectively. Finally, to demonstrate the potential of the proposed approach, a comparative analysis between the hybrid method and the most commonly used benchmarks in the literature, namely, the persistence method and the method based on similar days, has been carried out. It has been concluded that the proposed model yields promising results regardless the length of the historical dataset.

Future work will address the estimation of the power generated by the PV facilities within the structure of the VPP. To this end, the forecasting techniques presented in this paper will be used, weighting each station according to the rated power. Finally, as the historical dataset of the installation increases in length, the computational time of the algorithm will grow in importance, augmenting the interest in the implementation of advance optimization techniques for some steps in the algorithm such as the calculation of the weights.

REFERENCES

[1] (Oct. 2019). *Market Report Series: Renewables 2019. Analysis and forecasts for 2024*. International Energy Agency (IEA). Paris, France. Accessed: Sep. 30, 2020. [Online]. Available: https://webstore.iea.org/renewables-2019
[2] M. Perez, R. Perez, K. R. Rabago, and M. Putman, "Overbuilding & curtailment: The cost-effective enablers of firm PV generation," *Sol. Energy*, vol. 180, pp. 412–422, Jan. 2019.
[3] B. Lin and J. Zhu, "The role of renewable energy technological innovation on climate change: Empirical evidence from China," *Sci. Total Environ.*, vol. 659, pp. 1505–1512, Apr. 2019.
[4] R. Shah, N. Mithulananthan, R. C. Bansal, and V. K. Ramachandaramurthy, "A review of key power system stability challenges for large-scale PV integration," *Renew. Sustain. Energy Rev.*, vol. 41, pp. 1423–1436, Jan. 2015.
[5] F. Falko, R. Brecha, and G. Luderer, "Analyzing major challenges of wind and solar variability in power systems," *Renew. Energy*, vol. 81, pp. 1–10, Sep. 2015.
[6] X. Li, D. Hui, and X. Lai, "Battery energy storage station (BESS)-based smoothing control of photovoltaic (PV) and wind power generation fluctuations," *IEEE Trans. Sustain. Energy*, vol. 4, no. 2, pp. 464–473, Apr. 2013.
[7] M. Katsanevakis, R. A. Stewart, and J. Lu, "Aggregated applications and benefits of energy storage systems with application-specific control methods: A review," *Renew. Sustain. Energy Rev.*, vol. 75, pp. 719–741, Aug. 2017.
[8] S. Grillo, M. Marinelli, S. Massucco, and F. Silvestro, "Optimal management strategy of a battery-based storage system to improve renewable energy integration in distribution networks," *IEEE Trans. Smart Grid*, vol. 3, no. 2, pp. 950–958, Jun. 2012.
[9] S. Ghavidel, L. Li, J. Aghaei, T. Yu, and J. Zhu, "A review on the virtual power plant: Components and operation systems," presented at the IEEE Int. Conf. Power Syst. Technol. (POWERCON), Sep. 2016. [Online]. Available: https://ieeexplore.ieee.org/document/7754037
[10] H. Saboori, M. Mohammadi, and R. Taghe, "Virtual power plant (VPP), definition, concept, components and types," presented at the Asia–Pacific Pow and Ener. Engr. Conf., Mar. 2011. [Online]. Available: https://ieeexplore.ieee.org/document/5749026
[11] D. Pudjianto, C. Ramsay, and G. Strbac, "Virtual power plant and system integration of distributed energy resources," *IET Renew. Power Gener.*, vol. 1, no. 1, pp. 10–16, Mar. 2007.
[12] G. Ritzer and N. Jurgenson, "Production, consumption, prosumption: The nature of capitalism in the age of the digital 'prosumer,'" *J. Consum. Culture*, vol. 10, no. 1, pp. 13–36, Mar. 2010.
[13] N. Etherden, V. Vyatkin, and M. H. J. Bollen, "Virtual power plant for grid services using IEC 61850," *IEEE Trans. Ind. Informat.*, vol. 12, no. 1, pp. 437–447, Feb. 2016.
[14] A. Tascikaraoglu, O. Erdinc, M. Uzunoglu, and A. Karakas, "An adaptive load dispatching and forecasting strategy for a virtual power plant including renewable energy conversion units," *Appl. Energy*, vol. 119, pp. 445–453, Apr. 2014.
[15] A. Mellit, A. Massi Pavan, E. Ogliari, S. Leva, and V. Lughi, "Advanced methods for photovoltaic output power forecasting: A review," *Appl. Sci.*, vol. 10, no. 2, p. 487, Jan. 2020.
[16] S. Sobri, S. Koohi-Kamali, and N. A. Rahim, "Solar photovoltaic generation forecasting methods: A review," *Energy Convers. Manage.*, vol. 156, pp. 459–497, Jan. 2018.
[17] J. Antonanzas, N. Osorio, R. Escobar, R. Urraca, F. J. Martinez-de-Pison, and F. Antonanzas-Torres, "Review of photovoltaic power forecasting," *Sol. Energy*, vol. 136, pp. 78–111, Oct. 2016.
[18] F. Barbieri, S. Rajakaruna, and A. Ghosh, "Very short-term photovoltaic power forecasting with cloud modeling: A review," *Renew. Sustain. Energy Rev.*, vol. 75, pp. 242–263, Aug. 2017.
[19] R. H. Inman, H. T. C. Pedro, and C. F. M. Coimbra, "Solar forecasting methods for renewable energy integration," *Prog. Energy Combustion Sci.*, vol. 39, no. 6, pp. 535–576, Dec. 2013.

[20] U. K. Das, K. S. Tey, M. Seyedmahmoudian, S. Mekhilef, M. Y. I. Idris, W. Van Deventer, B. Horan, and A. Stojcevski, ''Forecasting of photovoltaic power generation and model optimization: A review,'' *Renew. Sustain. Energy Rev.*, vol. 81, pp. 912–928, Jan. 2018.
[21] M. Kudo, A. Takeuchi, Y. Nozaki, H. Endo, and J. Sumita, ''Forecasting electric power generation in a photovoltaic power system for an energy network,'' *Electr. Eng. Jpn.*, vol. 167, no. 4, pp. 16–23, Jun. 2009.
[22] M. Q. Raza, M. Nadarajah, and C. Ekanayake, ''On recent advances in PV output power forecast,'' *Sol. Energy*, vol. 136, pp. 125–144, Oct. 2016.
[23] C. Wan, J. Zhao, Y. Song, Z. Xu, J. Lin, and Z. Hu, ''Photovoltaic and solar power forecasting for smart grid energy management,'' *CSEE J. Power Energy Syst.*, vol. 1, no. 4, pp. 38–46, Dec. 2015.
[24] *Spanish Agency of Meteorology (AEMET) Numerical Weather Predictions*. Accessed: Sep. 30, 2020. [Online]. Available: http://www.aemet.es/es/eltiempo/prediccion/modelosnumericos/harmonie_arome_ccaa?opc2=mad#
[25] L. Benali, G. Notton, A. Fouilloy, C. Voyant, and R. Dizene, ''Solar radiation forecasting using artificial neural network and random forest methods: Application to normal beam, horizontal diffuse and global components,'' *Renew. Energy*, vol. 132, pp. 871–884, Mar. 2019.
[26] C. Furlan, A. P. de Oliveira, J. Soares, G. Codato, and J. F. Escobedo, ''The role of clouds in improving the regression model for hourly values of diffuse solar radiation,'' *Appl. Energy*, vol. 92, pp. 240–254, Apr. 2012.
[27] Y. Zhang, M. Beaudin, R. Taheri, H. Zareipour, and D. Wood, ''Day-ahead power output forecasting for small-scale solar photovoltaic electricity generators,'' *IEEE Trans. Smart Grid*, vol. 6, no. 5, pp. 2253–2262, Sep. 2015.
[28] A. Mellit and S. A. Kalogirou, ''Artificial intelligence techniques for photovoltaic applications: A review,'' *Prog. Energy Combustion Sci.*, vol. 34, no. 5, pp. 574–632, Oct. 2008.
[29] F. Wang, Z. Mi, S. Su, and H. Zhao, ''Short-term solar irradiance forecasting model based on artificial neural network using statistical feature parameters,'' *Energies*, vol. 5, no. 5, pp. 1355–1370, May 2012.
[30] R. Marquez, V. G. Gueorguiev, and C. F. M. Coimbra, ''Forecasting of global horizontal irradiance using sky cover indices,'' *J. Sol. Energy Eng.*, vol. 135, no. 1, pp. 011017-1–011017-5, Feb. 2013.
[31] B. Amrouche and X. Le Pivert, ''Artificial neural network based daily local forecasting for global solar radiation,'' *Appl. Energy*, vol. 130, pp. 333–341, Oct. 2014.
[32] X. Qing and Y. Niu, ''Hourly day-ahead solar irradiance prediction using weather forecasts by LSTM,'' *Energy*, vol. 148, pp. 461–468, Apr. 2018.
[33] Y.-Y. Hong, J. J. F. Martinez, and A. C. Fajardo, ''Day-ahead solar irradiation forecasting utilizing Gramian angular field and convolutional long short-term memory,'' *IEEE Access*, vol. 8, pp. 18741–18753, 2020.
[34] C. H. Fajardo, J. Mula, and R. Poler, ''Adaptive and hybrid forecasting models—A review,'' *Engineering Digital Transformation*. Cham, Switzerland: Springer, Sep. 2018, pp. 315–322.
[35] Z. Hajirahimi and M. Khashei, ''Hybrid structures in time series modeling and forecasting: A review,'' *Eng. Appl. Artif. Intell.*, vol. 86, pp. 83–106, Nov. 2019.
[36] A. Teke, H. B. Yıldırım, and Ö. Çelik, ''Evaluation and performance comparison of different models for the estimation of solar radiation,'' *Renew. Sustain. Energy Rev.*, vol. 50, pp. 1097–1107, Oct. 2015.
[37] O. Behar, A. Khellaf, and K. Mohammedi, ''Comparison of solar radiation models and their validation under Algerian climate—The case of direct irradiance,'' *Energy Convers. Manage.*, vol. 98, pp. 236–251, Jul. 2015.
[38] L. Bengtsson, U. Andrae, T. Aspelien, Y. Batrak, J. Calvo, W. de Rooy, E. Gleeson, B. Hansen-Sass, M. Homleid, M. Hortal, and K. I. Ivarsson, ''The HARMONIE–AROME model configuration in the ALADIN–HIRLAM NWP system,'' *Monthly Weather Rev.*, vol. 145, no. 5, pp. 1919–1935, Apr. 2017.
[39] Z. Zhu and C. E. Woodcock, ''Object-based cloud and cloud shadow detection in landsat imagery,'' *Remote Sens. Environ.*, vol. 118, pp. 83–94, Mar. 2012.
[40] C. Huang, N. Thomas, S. N. Goward, J. G. Masek, Z. Zhu, J. R. G. Townshend, and J. E. Vogelmann, ''Automated masking of cloud and cloud shadow for forest change analysis using landsat images,'' *Int. J. Remote Sens.*, vol. 31, no. 20, pp. 5449–5464, Oct. 2010.
[41] S. Le Hégarat-Mascle and C. André, ''Use of Markov random fields for automatic cloud/shadow detection on high resolution optical images,'' *ISPRS J. Photogramm. Remote Sens.*, vol. 64, no. 4, pp. 351–366, Jul. 2009.
[42] Z. Zhu and C. E. Woodcock, ''Automated cloud, cloud shadow, and snow detection in multitemporal Landsat data: An algorithm designed specifically for monitoring land cover change,'' *Remote Sens. Environ.*, vol. 152, pp. 217–234, Jul. 2014.
[43] Y. Huang, S. Siems, M. Manton, A. Protat, L. Majewski, and H. Nguyen, ''Evaluating Himawari-8 cloud products using shipborne and CALIPSO observations: Cloud-top height and cloud-top temperature,'' *J. Atmos. Ocean. Technol.*, vol. 36, no. 12, pp. 2327–2347, Dec. 2019.
[44] M. Diagne, M. David, P. Lauret, J. Boland, and N. Schmutz, ''Review of solar irradiance forecasting methods and a proposition for small-scale insular grids,'' *Renew. Sustain. Energy Rev.*, vol. 27, pp. 65–76, Nov. 2013.
[45] P. Bacher, H. Madsen, and H. A. Nielsen, ''Online short-term solar power forecasting,'' *Sol. Energy*, vol. 83, no. 10, pp. 1772–1783, Oct. 2009.
[46] S. Haykin, ''Multilayer Perceptrons,'' in *Neural Networks and Learning Machines*, 3rd ed. Hamilton, ON, Canada: Prentice-Hall, 2009, p. 175.
[47] E. Akarslan and F. O. Hocaoglu, ''A novel method based on similarity for hourly solar irradiance forecasting,'' *Renew. Energy*, vol. 112, pp. 337–346, Nov. 2017.
[48] P. Mandal, T. Senjyu, N. Urasaki, T. Funabashi, and A. K. Srivastava, ''A novel approach to forecast electricity price for PJM using neural network and similar days method,'' *IEEE Trans. Power Syst.*, vol. 22, no. 4, pp. 2058–2065, Nov. 2007.
[49] J. Fonseca, T. Oozeki, H. Ohtake, T. Takashima, and O. Kazuhito, ''On the use of maximum likelihood and input data similarity to obtain prediction intervals for forecasts of photovoltaic power generation,'' *J. Electr. Eng. Technol.*, vol. 10, no. 1, pp. 30–40, May 2015.
[50] D. W. van der Meer, J. Widén, and J. Munkhammar, ''Review on probabilistic forecasting of photovoltaic power production and electricity consumption,'' *Renew. Sustain. Energy Rev.*, vol. 81, no. 1, pp. 1484–1512, Jan. 2018.

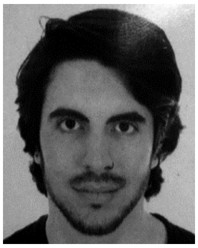

GUILLERMO MORENO was born in Tarifa, Cadiz, Spain, in 1990. He received the University degree in industrial engineering technology from the University of Malaga, Malaga, Spain, in 2015, and the master's degree in industrial engineering from the University of Alcala, Madrid, Spain, in 2018.

Since 2017, he has been a Research Assistant with the Electronics Engineering Department, University of Alcala. His research interests include design of photovoltaic installations, photovoltaic power forecasting, and virtual power plants management and operation.

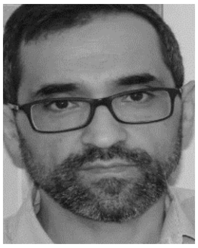

PEDRO MARTIN received the Ph.D. degree in telecommunications engineering from the University of Alcala, Spain, in 2000, and the degree in telecommunications from the Polytechnic University of Madrid, Spain, in 1994.

He currently works as an Associate Professor with the Department of Electronics, the University of Alcala. He is a member of the research group Electronics Engineering applied to the Renewable Energies. His research interets include design of embedded systems for power electronic systems and smart grids.

CARLOS SANTOS received the B.S. degree in telecommunications engineering and the M.Sc. degree in electrical engineering from the University of Alcala, Spain, in 2010 and 2011, respectively, and the Ph.D. degree in electronics in 2016.

He is currently with the Postdoctoral Research Contract, Department of Electronics, University of Alcala. His research interests include fusion algorithms, forecasting strategies, varying-time sampling control techniques, energy management systems, virtual power plants, and smart grids.

FRANCISCO J. RODRÍGUEZ (Member, IEEE) received the B.Sc. degree in technical telecommunication engineering from the University of Alcalá, Alcalá de Henares, Spain, in 1985, the M.Sc. degree in telecommunication from the Technical University of Madrid, Madrid, Spain, in 1990, and the Ph.D. degree in electronics engineering from the University of Alcalá, in 1997.

He worked in the private electronic industry for two years. Since 1986, he has been a Lecturer with the Department of Electronics, University of Alcalá, where he is currently a Professor. He is the author of more than 160 refereed publications in international journals, book chapters, and conference proceedings. Also, he has directed more than 55 investigation projects funded by public institutions and private industry. His research interests include smartgrids, microgrids, renewable energies, control electronics, and real-time processing.

ENRIQUE SANTISO received the Ph.D. degree in telecommunications engineering, in 2003.

He is currently a University Professor. Since January 1990, he has been teaching and researching with the Electronics Department, University of Alcalá. He has taught subjects related to sensing, data acquisition and processing, control, power, and digital systems. He has participated in eight published books, related to the teaching given. The teaching work was supported by the recognition of five teaching periods (five years). His research interests, which began in 1991, include mobile robotic systems (positioning and guidance), sensory systems, data acquisition, control, and power. He has directed two research projects in public calls, participated in one European project and 28 national projects. He has participated in 38 research and development projects with companies. He has 20 international articles and 41 participations in conferences. His research work has been recognized with the award of five research sections (six-year periods). He is also focusing his research on the management of electrical energy and the optimization of production systems.

Received October 15, 2020, accepted October 26, 2020, date of publication November 5, 2020, date of current version November 17, 2020.

Digital Object Identifier 10.1109/ACCESS.2020.3036340

Addressing Challenges in Prosumer-Based Microgrids With Blockchain and an IEC 61850-Based Communication Scheme

MIGUEL GAYO, CARLOS SANTOS, FRANCISCO JAVIER RODRÍGUEZ SÁNCHEZ, (Member, IEEE), PEDRO MARTÍN, JOSÉ A. JIMÉNEZ, AND MIGUEL TRADACETE

Department of Electronics, University of Alcalá, 28871 Alcalá de Henares, Spain

Corresponding author: Miguel Gayo (miguel.gayo@uah.es)

This work was supported in part by the PROMINT-CM Project funded by the Comunidad de Madrid and the European Social Fund under Grant P2018/EMT4366, and in part by the Ministerio de Ciencia, Innovación y Universidades through the INERCIA0 Project under Grant RTI2018-098865-B-C33.

ABSTRACT Since the advent of the microgrid (MG) concept, almost two decades ago, the energy sector has evolved from a centralized operational approach to a distributed generation paradigm challenged by the increasing number of distributed energy resources (DERs) mainly based on renewable energy. This has encouraged new business models and management strategies looking for a balance between energy generation and consumption, and promoting an efficient utilization of energy resources within MGs and minimizing costs for the market participants. In this context, this paper introduces an efficient management strategy, which is aimed at obtaining a fair division of costs billed by the utilities, without relying on a centralized utility or MG aggregator, through the design of a local event-based energy market within the MG. This event-driven MG energy market operates with blockchain (BC) technology based on smart contracts for electricity transactions to both guarantee veracity and immutability of the data and automate the transactions. The event-based energy market approach focuses on two of the design limitations of BC, namely the amount of information to be stored and the computational burden, which are significantly reduced while maintaining a high level of performance. Furthermore, the prosumer data is obtained by using IEC 61850 standard-based commands within the BC framework. By doing so, the system is compatible with any device irrespective of the manufacturer implementing the IEC 61850 standard. The advantages of this management approach are considerable for: MG participants, in terms of financial benefits; the MG itself, as it can operate more independently from the main grid; and the grid since the MG becomes less unpredictable due to the internal energy exchanges. The proposed strategy is validated on an experimental setup employing low-cost devices.

INDEX TERMS Blockchain, distributed generation, local energy market, prosumer, smart contract, Transactive Energy, aperiodic strategy.

NOMENCLATURE

Most of the symbols and notations used throughout this paper are defined below for quick reference. Others are defined following their first appearances, as needed.

A. ABBREVIATIONS & INDICES

MG	Microgrid
BC	Blockchain
SC	Smart Contract
EMS	Energy Management System
SBC	Single Board Computer
LD	Logical Device
LN	Logical Node
SoD	Send on Delta
SD	Standard Deviation
i	Index of prosumer of the Microgrid
t	Index of time
k	Index of aperiodic update

The associate editor coordinating the review of this manuscript and approving it for publication was Jiayong Li.

B. PARAMETERS

$PV_i(t)$	PV power of prosumer i in the MG at instant t
$Demand_i(t)$	Inflexible demand of prosumer i in the MG at instant t
$Load_i(t)$	Controllable load of prosumer i in the MG at instant t
$Power_i(t)$	Balance of power of prosumer i in the MG at instant t
$Energy_i(t)$	Balance of energy of prosumer i in the last minute in the MG at instant t
$\rho_{MG}(t)$	Ratio between $PV_{MG}(t)$ and at $Demand_{MG}(t)$ at instant t
$\text{Price}_{buy}(t)$	Energy acquisition cost from the grid.
$\text{Price}_{sell}(t)$	Price offered by the grid for energy injection.
$\text{Price}_{MG}(t)$	Price of the energy in the MG.
$\text{Gap}_{price}(t)$	Price gap between buying and selling to the grid.
$\alpha_{price}(t)$	Price factor applied in the MG
$t_{i,k}$	Update time instant k of prosumer i.
Δ_{SoD}	Threshold Send on Delta.
$\text{Error}_i(t)$	Energy estimation error of prosumer i in the last minute at instant t.
$size_{round}$	Stored memory per market round.
$size_{tx}$	Stored memory per transaction.

I. INTRODUCTION

In recent years, the rapid expansion of Distributed Energy Resources (DERs), mainly based on renewable energy sources, has transformed the electrical power system resulting in reductions of greenhouse gas emissions and electricity costs, and mitigating adverse impacts on the power system such as overload on the main grid and transmission loss [1].

Increasing deployment of DERs which include some intelligence has changed the role traditional consumers play in the electrical power system, leading to a new actor that not only consumes but also produces electricity and maybe has demand response capabilities by means of some controllable loads and storage units [2]. This new actor in the electricity market is known as a prosumer that can be an energy provider or a consumer according to its local energy balance. Prosumers, as an entity, may consist of a combination of energy sources, loads, and storage capacity, and they seek to optimize economic decisions regarding their energy balance [3].

The integration of large amounts of prosumers, usually with low and unpredictable power generation capacity and electricity demand, is changing the traditional approach of power systems, which is posing new challenges [4], and creating new opportunities for the generation and distribution operators and for the electricity market. The traditional centralized concept of the grid has given way to a complete decentralized strategy where several prosumers are interconnected and locally managed being seen by the utility grid as a controllable load or generator. Microgrids (MGs) epitomize this concept, which was first introduced in [5]. MGs facilitate the integration of DERs, without compromising the resilience of the main grid, creating opportunities for new economic models such as electricity trading, which can take place not only between MGs and utilities, but also among multiple prosumers, through a local energy market. They also promote the development of control systems that allow plug & play capabilities to face the ever-changing MG architecture.

This new concept, which challenges also the traditional business models, required a comprehensive framework with the aim of determining the electricity prices and defining the new business players and models, such as peer-to-peer frameworks for locally energy trading and transactions. In this context, prosumers try to maximize their profit by selling their surplus energy and the grid aims at maximizing efficiency.

To address these challenges, several works can be found in the literature proposing different solutions mainly based on centralized and distributed energy management systems (EMSs). Regarding the former, in [6] and [7] MGs are considered as scaled-down versions of the centralized electricity system and the EMS is defined accordingly. Centralized MG management and control suffers from drawbacks in terms of: (a) the need for a MG central controller with high computational capabilities, due to the amount of controllable resources, (b) lack of scalability since a small change in one node affects the central controller; and (c) privacy [8] as customers may not be willing to share their private data. Finally, all the information must be integrated and processed at a single point, which also results in reliability and security vulnerability of the central controller [9].

To overcome the drawbacks of the centralized methods, new EMS designs have been developed in a distributed fashion. For instance, in [10] authors simulate a MG with a distributed EMS achieving comparable performance with respect to the centralized counterpart. In [8] an example of distributed EMS, which includes a MG central controller (MGCC) operating in conjunction with the local controllers, is presented. However, this combined approach does not eliminate the vulnerability of a single point of failure.

The creation of local energy markets, that allow consumers and prosumers to trade energy, has been studied in the literature [11] as a way of decentralized management in MG. In local energy markets, prosumers try to match supply and demand by seeking competitive electricity prices, which results in greater resilience. The Brooklyn Microgrid [6] is one of the most known projects for the implementation of MG local energy market, which confirms the economic and technical feasibility of decentralized strategies. In [12], the concept of local energy market is taken one step further by interconnecting several geographically close MGs, which allows the surplus and deficit of energy to be exchanged in a neighboring market. This further reduces the dependency on the main grid and, as a result, increases the resilience of the MGs.

This paper introduces a novel event-based local energy management strategy for MGs. The design, development and implementation of the strategy is based on the combination of the BC technology and the IEC 61850 communication standard, enhancing the capabilities of both technologies when applied to energy-sector applications. BC technology is used to create a local energy market in a decentralized fashion, which has been proved to be remarkably resilient to failure and cannot be maliciously manipulated as it maintains a detailed record of past transactions that cannot be changed retrospectively. Furthermore, executable code embedded in the BC, which is called the smart contract (SC), allows the entire process to be automated [13]. Likewise, the BC-based local energy market is standardized by using the IEC 61850 communication protocol. The strong point of this approach is that the electrical parameters of all MG resources can be automatically obtained without the involvement of the resource owners, which avoids manipulation of those parameters for their own advantage. To the best of the author's knowledge, this is the first local energy market implementation that combines the IEC 61850 and BC technology whereby devices commercialized by diverse manufacturers can be seamlessly integrated in the market, in a plug & play fashion, which approaches to a real project. Research works in this topic are non-existent.

The main contributions of this paper are summarized as follows:

1. Integration of the IEC 61850 standard into the Smart Contracts of the BC. This enables the distributed communication between the commercial devices implementing the standard.
2. A reduction in the amount of resources required to create a local distributed energy market by means of event-based techniques which do not negatively affect the system performance. This allows the system to operate efficiently for a greater number of years.
3. Low-cost hardware implementation of the system, which decreases the time for the return on the investment making it feasible to use it in residential environments.
4. For both energy producers and consumers, the development of a win-win market strategy within the MG allows financial savings to be obtained by taking advantage of the gap between the price paid for the electricity consumed and that generated and injected to the grid.

The paper is organized as follows: Section II describes the underlying technologies employed in the local energy market design, namely BC and IEC 61850 communication standard and the advantages that they can bring to the energy sector in general and to MGs in particular. Section III shows the advantages of the combination of both technologies. Section IV describes the design of proposed prosumer-based microgrid. Section V presents the implementation of the proposed BC-IEC 61850 network, analysing the required resources for its correct operation. In section VI, the system is tested in a specific case of use. Finally, in Section VII, the conclusions and the future work are outlined.

II. LITERATURE REVIEW: STATE OF THE UNDERLYING TECHNOLOGIES

Vast literature has been published on BC technology and IEC 61850 communication standard separately. However, the literature lacks references considering both technologies working together. This paper aims at filling this gap. In this section a literature review of the two technologies mentioned above, is carried out. Being two of the most researched technologies and with the aim of narrowing the search, this section only deals with the most recent and up to date works in the context of the energy sector and MG.

A. BLOCKCHAIN TECHNOLOGY IN MICROGRIDS

BC is the technology behind Bitcoin cryptocurrency, created in 2008 by Shatoshi Nakamoto [14]. This disruptive technology is based on decentralized computation with secure storage and transactions. BC has evolved since then, and these days, BC is being widely used in fields, such as, transportation systems [7], IoT [8], financial sector [9], electric vehicle charging and e-mobility [10], and the energy sector in general [15], inter alia.

BC can be briefly defined as a decentralized information network with a distributed computing paradigm, which means that there is not a master computer compiling and processing the information. BC is based on a distributed ledger which guarantees the immutability of stored data and the availability of the latest version in each node of the network. To that end, BC employs chronological, chained blocks to store encrypted data generated by distributed consensus algorithms. Therefore, blocks record transactions, i.e. actions created by the BC participants, and ensure that they are in the correct sequence and have not been tampered with. This is achieved by linking each new block with all the previous ones through an ID that is unique and dependent on the information contained in the block and the ID of the previous block. This allows any change in the information contained in the previous block to be quickly detected and discarded. Thus, this technology makes it possible to eliminate intermediaries making all the transactions faster and more secure, as previous records cannot be altered, and they are available at any time for all the participants in the network. In 2014 the BC technology rapidly evolved with the creation of a new cryptocurrency, Ethereum [13], which allowed code to be executed in a decentralized way via the so-called Smart Contracts.

BC solutions for the energy sector have been proposed in several works. A comprehensive review of BC activities and initiatives in the shape of projects and startups in the energy sector can be found in [15]. The authors argue that the decentralized features of BC technology facilitate the creation of trading platforms for billing purposes. They also include an extensive survey of platforms used to design projects in the energy sector. In [12], a review of BC-based current projects and platforms in different domains is carried out. They determine the requirements of smart energy systems with the aim of identifying appropriate BC-based solutions for smart energy applications. In [6] a case study proves the effectiveness of BC when it comes to operating decentralized MG energy markets. The authors in [16] go beyond economic aspects of energy transactions and, by means of BC technology, they track energy losses during energy transactions in MGs.

Distributed Generation, MGs and the implementation of energy local markets for energy trading call for the use of BC technology. This will, without doubt, transform the energy landscape as shown in the literature where numerous projects under development or in preliminary testing are presented.

B. COMMUNICATIONS STANDARDS: IEC 61850 IN MICROGRIDS

The IEC 61850-based communication standard has been universally accepted for substation automation [17]. However, new parts have been developed and published allowing the standard to be used as a standard for communication networks and systems for power utility automation. Most researchers agree that the future trends are towards standardization through IEC 61850 since it is based on the interoperability approach.

In the context of MGs, efficient and secure communications among all the nodes become an essential feature. This is another ongoing research topic as demonstrated by the numerous papers recently published in the literature. In [18] an IEC 61850-based energy management system for emergencies is presented. The paper shows the plug-and-play capabilities that the IEC 61850 standard can bring, for alternative power system operation based on local assets in the event of an emergency. A review on the evolution of MG communication approaches is presented in [19], where authors identify specific communication requirements in MGs such as reliability, scalability, interoperability and cybersecurity, which can be fulfilled by the help of the IEC 61850 standard. An IEC 61850-based model of a MG protection system with logical nodes and datasets is proposed in [20] which is aimed at ensuring the protection in a bidirectional system. In [21] authors propose a standardized communication framework based on IEC 61850 to manage energy routers and to improve the operation of MGs achieving the optimal selection of the power source and routing path. Communications for management and control of MGs based on IEC 61850 are designed and implemented in [22] and [23], proving the effectiveness and security of the standard when implemented in a distributed EMS with small end-to-end latency times within WAN networks. Finally, in [24] IEC 61850 is also used to improve MG automation, proposing a standard-based model for controllable loads. Results from the above research works encourage and support the inclusion of IEC 61850 in MG management and automation.

In 2009, in response to the increasing number of DERs aggregated to the grid, part 7-420 [25] was provided, which standardizes several DERs by using predefined logical nodes (LNs). Device modelling via LNs helps to simplify the integration of equipment from different manufacturers. This significantly facilitates the implementation, as well as the interconnection of different MGs.

III. HIGHLIGHTS OF THE COMBINED APPROACH

This section highlights the benefits of combining BC technology and the IEC 61850 communication standard in MGs.

As stated above, BC technology has prominent features, such as immutability of the stored data, decentralization, public ledger facility and security, to name a few. These inherent features have promoted the use of BC technology to overcome the main drawbacks of centralized-based EMSs for MGs. Despite of the obvious benefits derived from the use of BC technology, there are, however, potential shortcomings and challenges which stem from the fact that BC is far from being a mature technology in MG applications [26], [27].

These shortcomings are especially relevant in Prosumer-based MGs. These MGs are dynamic in nature, where prosumers join or leave the MG. Therefore, the MG changes its temporal and spatial topology, which poses a challenge. To face this problem, the proposed BC-IEC 61850 strategy presents the following features:

1.-Interoperability: equipment and hardware used in MGs are usually manufactured by different vendors overlooking the interoperability between these devices. This aspect plays an important role in producing standardized transactions for the BC implementation.

2.-Generic plug & play: The design of non-device-specific SCs provides the capability to add or remove different commercial devices from the MG, introducing the switches automatically to the local energy market.

3.-Veracity: Data acquisition in a distributed manner by running SC with IEC 61850 communication standard adds an extra layer of security as it reduces the chances of manipulation with respect to data acquisition locally and subsequent delivery for storage in the BC.

IV. DESIGN OF THE PROSUMER-BASED MICROGRID

In this section, the proposed prosumer-based architecture for a MG is introduced. The developed strategy takes advantage of the fact that prosumers generally have different energy demand and supply profiles which depend on the prosumers' energy generation capacity, or whether they have energy storage systems (ESSs) or some controllable loads. This means that prosumers could draw or inject electricity into the distribution grid at different times and in different quantities for profit maximization.

The proposed architecture relies on energy agents representing prosumers within the MG, which are interconnected through their own distribution grid. The MG is connected to the main grid at a single point, through a point of common coupling, where the amount of energy is measured by bidirectional smart meters. As the electricity prices vary substantially over the day, splitting the cost of the bill among prosumers is not straightforward. Local energy markets arise as a means of overcoming the problem of fair cost sharing, and

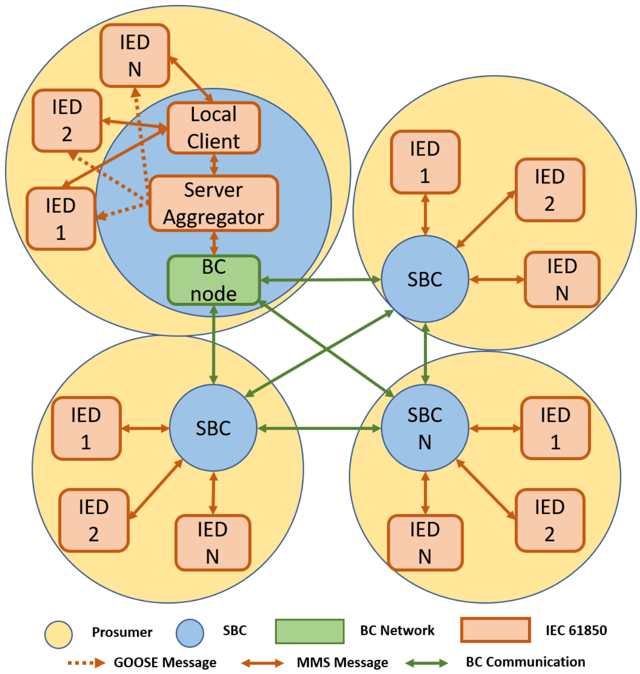

FIGURE 1. BC-IEC 61850-based communication architecture between the different devices that comprise the MG.

balancing energy consumption and generation curves within the MG, thereby reducing the amount of energy exchanged with the main grid.

The objective of the proposed MG is to facilitate the deployment of clean energy technologies, while eliminating the potential barrier to achieving fair cost sharing. To address this, the designed market strategy increases the return on investment by providing cost savings and increasing profits e.g. reducing the electricity bill, trading energy surplus, etc., for the prosumers participating in the MG. Finally, the privacy and veracity of the prosumers' data are guaranteed by combining BC technology and the IEC 61850 communication standard.

A. COMMUNICATIONS ARCHITECTURE BASED ON BC AND IEC 61850

In this section, the communication architecture based on BC and the IEC 61850 standard for the proposed prosumer-based MG is described. It is assumed that the prosumer's installed equipment, i.e. inverters, energy storage elements, smart meters, controllable switches, etc., complies with the IEC 61850 standard. The IEC 61850 communication standard works with a client-server structure in which Intelligent Electronic Devices (IEDs) play the role of a server. The servers send their data by request of the client. Therefore, an IEC 61850 client is only needed to collect data from these servers.

FIGURE 1 shows the architecture that implements the communications between the MG prosumers, and combines BC technology and the IEC 61850 standard. It can be seen that prosumers are connected to each other through a BC network. The installed equipment for each prosumer consists of two types of devices: the IEDs, which are IEC 61850 servers, and a single board computer (SBC) which comprises a standard client, a standard server with the installation model and a BC node. The messages exchanged between clients and servers are based on the Manufacturing Message Specification (MMS) protocol whereas those sent by the server aggregator to the IEDs are based on Generic Object-Oriented Substation events (GOOSE) with the aim of minimising the latency in the installation's state changes. Both protocols are based on the IEC 61850 standard. GOOSE messages are directly transmitted through ethernet packets with a subscriber-publisher structure and with a maximum latency of 3 ms [28].

The standard IEC-61850 operation is implemented in the Prosumer Local Phase (described in detail in SECTION IV-B-1) in which a client, which runs on a SBC, constantly reads the prosumer's IED data. This local client sends the data to a server aggregator. The proposed aggregator is modelled according to the Smart Home System proposal [17], in which the SHCT logical node is presented. This node is based in the IEC-61850 standard and is aimed at: (i) controlling the installation as a whole (the amount of energy exchanged with the network and the price of such exchanges); (ii) switching to the different modes of operation, i.e. islanded or grid connected; and (iii) defining optional configurations (voltage and current limits, times at which different operating modes are allowed, etc.).

The implementation of another IEC 61850 client in the form of SC can be considered as a novel feature of the proposed system. The execution of this SC results in the acquisition of data from all aggregator servers that are connected to the MG. This execution occurs automatically whenever an aggregator detects that the conditions of the installed equipment have changed significantly since the last acquisition.

This SC sends an MMS message to each of the registered devices and, in response, it receives another MMS message with the requested data. From this data only those parameters affecting the efficient system operation, e.g. energy generation-consumption balance in the time period since the last BC register update and the current demand, are included in the BC immutable database. Furthermore, if the prosumer has additional generation capacity or conversely load demand through controllable loads, it sends an offer of the amount of extra energy it can provide or absorb from the MG.

In this way it is verified that the SC is designed to read any IED from any manufacturer that supports the IEC 61850 standard, acquiring the selected parameters. Moreover, the results of the local energy market are sent to each SBC through an MMS message by executing another SC, which acts as IEC 61850-based client updating the data of the server aggregator. If the server aggregator receives an order to change the state of the installed equipment, the aggregator sends GOOSE messages to all the IEDs needed to make this change possible, at a given instant of time.

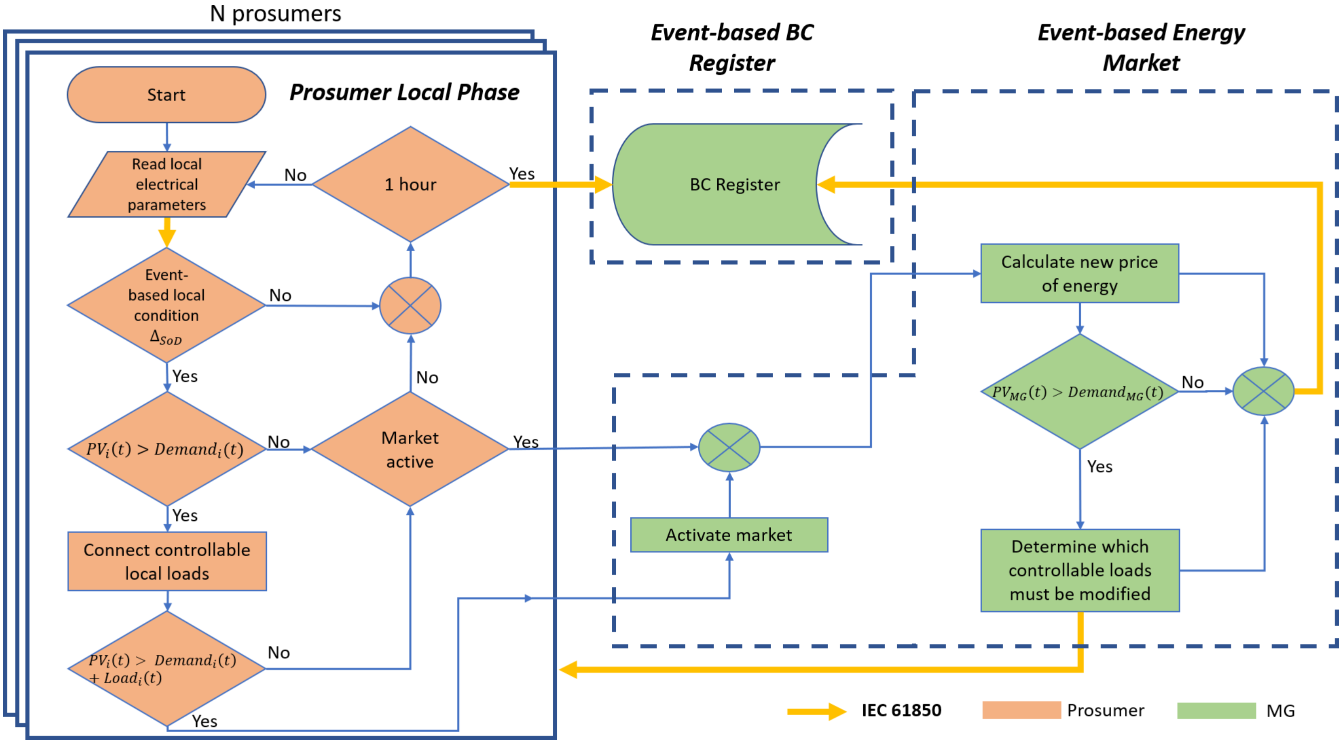

FIGURE 2. Flowchart representing the tasks prosumers perform both locally in a distributed manner through the SC. Three phases are clearly differentiated: prosumer local phase, event-based energy market and event-based BC register.

B. EVENT-BASED LOCAL ENERGY MARKET

BC technology relies on an ever-growing distributed database, which is updated by appending blocks containing new information. These blocks are sequentially attached to the end of a file which compiles all the information that was previously received. As a result, the amount of information to be stored and transmitted becomes one of the most critical parameters when it comes to designing a hardware system to implement the BC.

To meet this challenge and to reduce the communication within the MG, an event-based local energy market is designed. This event-driven control approach triggers the market only when there is a significant change in the energy exchanges within the MG. Consequently, a significant reduction in the amount of information to be processed and sent through the communication channels is achieved, without degrading the system performance. For its operation, a Send on Delta (SoD) data collecting scheme is chosen for its simplicity and efficiency [29]. At the prosumer level, an implementation of SoD monitoring strategy evaluates the difference between the last-minute energy measurement sent by the prosumer to the MG and the current measurement. When the value of this difference is above a certain threshold level, Δ_{SoD}, which is set by the designer, the local energy market must be updated.

The expression used to calculate the difference mentioned before is the following:

$$t_{i,k} = \min\{t > t_{i,k-1} \| Energy_i(t) - Energy_i(t_{i,k-1})| \geq \Delta_{SoD}\}, \quad (1)$$

with:

$$Energy_i(t) = \int_t^{t+\Delta_t} Power_i(t)\, dt, \quad (2)$$

$$Power_i(t) = PV_i(t) - Demand_i(t) - Load_i(t), \quad (3)$$

$$\Delta_t = 60s, \quad (4)$$

where $t_{i,k}$, represents the trigger instant of the prosumer i, $Demand_i$ and $Load_i$ are the non-controllable and controllable load demanded by prosumer i, respectively, PV_i is photovoltaic energy generated by prosumer i, $Power_i$ indicates the power balance of prosumer i, $Energy_i(t)$ is the last minute energy of the prosumer with respect to instant t in kWh and Δ_t, is the integration time.

The local trigger of any prosumer leads to a new market update, thus the market is always distributed and executed locally to fulfill the decentralized nature of BC technology. The operation of the proposed event-based local market is described in detail in the flow chart shown in FIGURE 2. This flowchart depicts the main tasks of the proposed strategy. The tasks are carried out in three phases:

1) PROSUMER LOCAL PHASE

The local phase of each prosumer relies on the use of the IEC 61850 communication standard to send the electrical parameters to the MG. Firstly, each prosumer's SBC locally monitors its electrical parameters through IEC 61850-based messages. Through a Manufacturing Message Specification (MMS) protocol for IEDs, changes in the prosumers' energy balance, i.e. changes greater than the aperiodic update threshold Δ_{SoD}, are detected. Whenever the prosumer satisfies the triggering condition, it is checked whether it is generating more energy than that consumed. To activate the prosumer's controllable loads, a GOOSE message is sent by the aggregator, because GOOSE messages are significantly faster than MMS messages. If the prosumer's energy balance is still positive, the local energy market is activated by executing a SC that captures the electrical parameters of all the prosumers within the MG in a distributed manner. In addition, the SC is also randomly executed by one of the prosumers on an hourly basis, even though the trigger condition is not satisfied. By doing so, a record of all the prosumers' electrical parameters is stored in the BC, with a dual purpose: firstly, the current MG state is known beforehand; and secondly the record saved is used for checking and splitting the billing.

2) EVENT-BASED ENERGY MARKET

The market phase begins when at least one of the prosumers has a positive energy balance in that instant of time, i.e., the prosumer generates more energy than it consumes at that point in time. The first step in this phase consists in calculating the price of the energy to be exchanged in the period considered as detailed in section IV-C In a second step, it is checked whether the energy the prosumers are injecting into the MG is greater than that being consumed. If this is the case, each prosumer with available controllable loads, submits an offer with the aim of taking advantage of more economically competitive energy. The MG matches the offers received for the energy surplus generated and sends the offer matching results to the prosumers so that they can control the loads based on those results. This is done by sending an IEC 61850-based message to their IEDs following the MMS protocol. The process of offer matching takes into account the current state of the controllable loads, which in the case of energy storage elements aims at equalizing the energy levels stored by all the prosumers that comprise the MG.

3) EVENT-BASED BC REGISTER

In this last phase, at the given time points defined by the two previously described phases, all the electrical parameters obtained through the IEC 61850 communication standard, the values of the energy exchanged between the different prosumers and the corresponding prices, are registered in an aperiodic fashion in the BC. In this way, the prosumers' bills for the energy drawn from the grid can be calculated by considering the price reduction and increase that each prosumer has to pay for the energy exchanges within the MG.

C. LOCAL ENERGY MARKET STRATEGY

This section describes the developed local energy market strategy. It is important to know that in most conventional trading schemes, prosumers have virtually no control of the trading process of the electricity they generate. Utilities buy and sell energy to retail prosumers by applying a profit margin and a set of taxes and surcharges. This results in a significant difference between the electricity prices paid to the prosumer for the electricity injected into the grid and that paid to purchase electricity from the grid [30]. Since the MG is made up of prosumers that want to purchase and sell energy at different times, the proposed local energy market offers more competitive energy purchase and selling prices than those of the utilities. Local energy markets are, therefore, beneficial to their participants provided that the average electricity price is lower than that set by the main grid.

The proposed market strategy takes advantage of the price difference between the purchase and sale price of energy to the grid. The pricing mechanism is based on matching the purchase and selling offers made by the prosumers for an amount of energy when the event-based market is activated, as described in section IV-B. When the market is activated and the information sent by all the prosumers is available, the amount of energy delivered and demanded within the MG is calculated as follows:

$$Demand_{MG}(t) = \sum\nolimits_{i=1}^{N} Demand_i(t), \tag{5}$$

$$PV_{MG}(t) = \sum\nolimits_{i=1}^{N} PV_i(t), \tag{6}$$

where N is the number of prosumers in the MG. With this data, the price of energy in MG is calculated for the amount of energy available to be exchanged. The market price is set by the following formula:

$$\text{Price}_{MG}(t) = \text{Price}_{sell}(t) + \alpha_{price}(t) * \text{Gap}_{price}(t) \tag{7}$$

with:

$$\text{Gap}_{price}(t) = (\text{Price}_{buy}(t) - \text{Price}_{sell}(t)) \tag{8}$$

$$\alpha_{price}(t) = \begin{cases} (0.5 - 0.2\rho_{MG}(t)), \ \rho_{MG}(t) < 1 \\ 0.3, \ \rho_{MG}(t) \geq 1 \end{cases} \tag{9}$$

$$\rho_{MG}(t) = \frac{PV_{MG}(t) - Demand_{MG}(t)}{Demand_{MG}(t)} \tag{10}$$

where ρ_{MG} represents the value of the energy ratio between the PV energy and the demand in the MG. α_{price}, represents the price adjustment factor within the MG. For values of ρ_{MG} greater than or equal to 1, this factor is adjusted to 0.3 to set a minimum factor within the MG. Gap_{price} represents the difference in price between buying (Price_{buy}) and selling (Price_{sell}) to the grid. Finally, $\text{Price}_{MG}(t)$, indicates the price of the surplus PV energy of prosumers that are purchased by other prosumers within the MG.

Through this formula a win-to-win market strategy is established for all prosumers due to the fact that prices within the MG will include the sale price to the grid plus a part of the Gap_{price} which will vary between 30% and 70% depending on the energy ratio ρ_{MG}.

Once the price is set, the surplus PV power is assigned to all the non-controllable loads of the MG. In case the surplus is not enough for all the loads, it covers the same percentage of each one of them and the rest of the demanded energy is consumed from the grid. In this way, each prosumer has a part of the energy at market price and another part at the grid price.

On the other hand, if the surplus is greater than the non-controllable loads, the transactions with the controllable loads are established, proceeding to activate them as indicated in FIGURE 2. In this case, all the possible loads are activated, giving priority to the prosumers that have the greatest capacity remaining to be fed.

Finally, if all the available controllable loads are fed and there is still a surplus power, it will be injected into the main grid. In this case, the energy not consumed in the MG is sold at the grid price, the percentage of surplus energy injected to the grid is calculated and this percentage is applied to the benefit of each prosumer that is injecting at that moment. This way, all prosumers with surplus will have the same percentage of their power injected at MG price and the rest at grid price.

V. IMPLEMENTATION AND PERFORMANCE EVALUATION OF BLOCKCHAIN-IEC 61850 PROPOSAL

To promote the use of renewable energies, the proposed strategy improves the operation of MG, maximizing the benefit of all its participants. To this end, it is essential that both the initial investment and the operational cost of the system are as low as possible. Consequently, to bring down the cost associated with the operation of the hardware system, low-power consumption strategies are mandatory. Therefore, consensus algorithms such as Proof of Work (PoW) [31] cannot be used, since appending new blocks in the BC demands high computational power, e.g. a node must decipher a cryptographic puzzle, which drives up the cost of the hardware implementing the node and increases energy consumption.

To select the most suitable technology for the BC introduced in this paper, a comprehensive review of the available frameworks to implement BC technology has been conducted. In [15] the underlying technologies employed in 140 projects that integrate BC technology in the energy sector are analyzed in detail. For the purposes of this work, the Hyperledger Fabric [32] is the best option for several reasons, namely: (a) it allows BC networks to be created in which each prosumer must be registered to participate; (b) the consensus algorithm is based on Byzantine Fault Tolerant protocols i.e. if there is a fault in any of the nodes of the BC network, it can continue operating without any problem; and most importantly (c) this framework is open source, which means that the code is available and can be modified and adapted to implement new functionalities. This significant advantage allows ARM-based hardware architectures to be included for BC implementation. This feature, which is not included in the original framework, allows the range of potential hardware components to be extended thereby reducing the cost and the power consumption of the final system.

A. HARDWARE IMPLEMENTATION

The hardware implementation of the BC network is based on the Raspberry Pi 4 model B [33], one of the most popular SBC. The selection is based on comparing performance characteristics through numerous benchmarks which are used to measure the millions of operations per second (MOPS) the hardware architecture can perform. Furthermore, the performance evaluation can be extrapolated to other architectures. In [34], an extensive set of tests are performed on the Raspberry Pi.

B. HYPERLEDGER FABRIC

The modular architecture of the Hyperledger Fabric framework [32] makes it possible to implement the energy exchange system in three phases:

1. The first one consists in building Hyperledger Fabric Docker images targeted towards hardware architectures with the 64-bit ARM processor such as Raspberry Pi devices. In addition, these docker images are modified to integrate the libiec61850 library [35], required for the execution of IEC 61850-based clients into the images. By doing so, the library can be used in the SCs. These modified images are freely available for download 36].
2. The second phase deals with the process of writing SC in Go language. Hyperledger Fabric supports Smart Contracts authored in general-purpose languages such as Java, Go and Node.js. However, among those languages, Go allows the use of the most complete and updated library for the IEC 61850 standard implementation, the libiec61850 [35], written in C language.
3. Finally, in the last phase, the clients interacting with the blockchain, are specified in JavaScript. These programs control the execution of the SCs.

In the Hyperledger Fabric framework, due to its modular architecture, every node in the system can be individually modelled displaying unique characteristics. However, in this work, the nodes comprising the blockchain have been designed to share the same characteristics thereby achieving a set of nodes with no priority over each other. Docker images of peer, those of orderer and an external database called CouchDB [37] have been integrated, to be able to submit enriched queries, which facilitates the development of applications that make use of the stored data.

C. PERFORMANCE EVALUATION

To assess the performance of the approach presented in this paper, a BC use case is tested, in which the market rounds happen at five-minute intervals. At the beginning of each market round, the prosumers send an offer in terms of the energy they need or the energy surplus they have. Then, to match the offers, a SC is executed, whereby it is determined whether a particular prosumer has to inject or draw energy from the grid. Finally, another SC is executed to read, in a distributed way, the IEC 61850 compatible devices and to save the data representing the state of the devices during the interval of time in the BC. By studying the data collected from the previous use case, the results can be extrapolated to other time intervals for the market rounds. Tests have also been carried out for different number of prosumers with the aim of evaluating the BC-IEC 61850 performance based on the number of prosumers that make up the MG. With the information

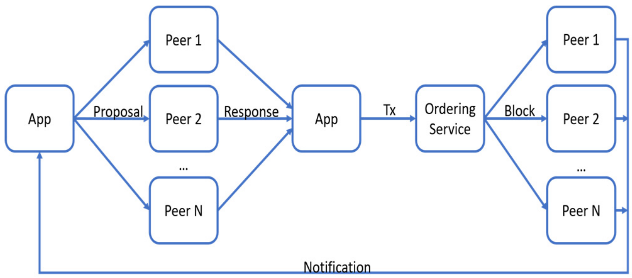

FIGURE 3. Transaction flow in Hyperledger Fabric framework.

compiled by running the tests, the required resources for the docker containers making up the nodes (peer, orderer and CouchDB), in terms of CPU usage, bandwidth, required storage and latencies are individually evaluated. This allows prosumers to assess whether to integrate an orderer or just the peer in their hardware devices reducing the cost of the system at the expense of affecting performance.

1) HYPERLEDGER FABRIC TRANSACTION FLOW

To gain a better insight into the data obtained, FIGURE 3 schematically shows the flow of information exchange involved in each transaction for it to be included in the BC. More detailed information can be found in [32]. From the figure, it can be seen that, the client application sends to all the SBCs working as peers, a transaction proposal created by the Hyperledger Fabric SDK. According to the endorsement policy that has been established, a subset of peers has to verify that the transaction is valid. In other words, each transaction needs only to be endorsed by the subset of peers required to satisfy the transaction's endorsement policy. For the transaction to be valid, the following points must be proved: (a) the proposal must be well formed; (b) a similar proposal must not have been completed in the past; (c) the signature must be valid; and (d) the client requesting the transaction is authorized to do so.

If the endorsement policy has been satisfied, the client application submits the transaction to the ordering service, which establishes consensus on the order of transactions and creates transaction blocks. A block can be created either when a predefined period, from the arrival of the first transaction, has elapsed or when the maximum number of transactions, the block can contain, has been reached. Once the block is created, the ordering service is responsible for broadcasting it to each peer, which append it to the end of their BC. When the ledger is up to date, a notification is sent to the client application informing it that the transaction has been correctly processed or that an error has occurred.

2) CPU

The total CPU usage, which is given by the percentage of use of one Raspberry Pi core, has been calculated considering the individual CPU utilization of the docker containers making up a BC node. This allows the analysis of the required resources to be more precise. TABLE 1 shows the minimum and maximum values of the CPU usage for the tests carried out for each element.

TABLE 1. Minimum and maximum CPU utilization in each test performed by each docker container.

Number of nodes	Peer		Orderer		CouchDB	
	Min (%)	Max (%)	Min (%)	Max (%)	Min (%)	Max (%)
3	1,73	2,22	0,23	0,89	0,69	2,43
4	2,30	2,94	0,22	1,07	0,68	1,91
8	2,36	4,53	0,15	0,59	0,62	2,29
16	3,40	6,60	0,24	0,93	0,63	2,49

TABLE 2. Bandwidth needed for the peer and the orderer as a function of the number of nodes that make up the BC network.

Number of nodes	Peer		Orderer	
	TX	RX	TX	RX
3	34,22	40,29	37,37	16,00
4	64,69	67,57	62,12	21,17
8	111,40	163,30	85,26	40,07
16	192,60	236,30	163,50	65,92

As for the peers, the maximum CPU usage follows a logarithmic trend as a function of the nodes connected to the BC. On the other hand, as far as the orderers are concerned, the CPU utilization changes slightly as the number of nodes increases, ranging from 0.15% to 1.07%. The CPU usage by the external database exhibits similar behavior with values ranging from 0.69% to 2.49% irrespective of the number of nodes.

For the worst-case scenario, with a 16-node blockchain and considering the maximum values of CPU time consumed by the elements that comprise the node, the CPU usage ratio just for one core of the 4-core processor, is roughly 9.16%. Therefore, it can be concluded that the hardware architecture comfortably meets the computational requirements of the system, again irrespective of the number of nodes.

3) BANDWIDTH

A similar procedure to that described above, has been followed to determine the bandwidth for the effective operation of the system. In contrast to the CPU usage, peak values for the bandwidth occur when transactions take place, when the nodes communicate with each other to validate the transactions, when they are accepted by the BC, and when the nodes are synchronized with the latest transactions.

As an example, FIGURE 4 shows the required bandwidth for both sending and receiving data by every peer and orderer in a 4-node experimental test. It can be observed that a peak occurs during the insertion of offers by prosumers. Likewise, a half-period-delayed smaller peak can also be

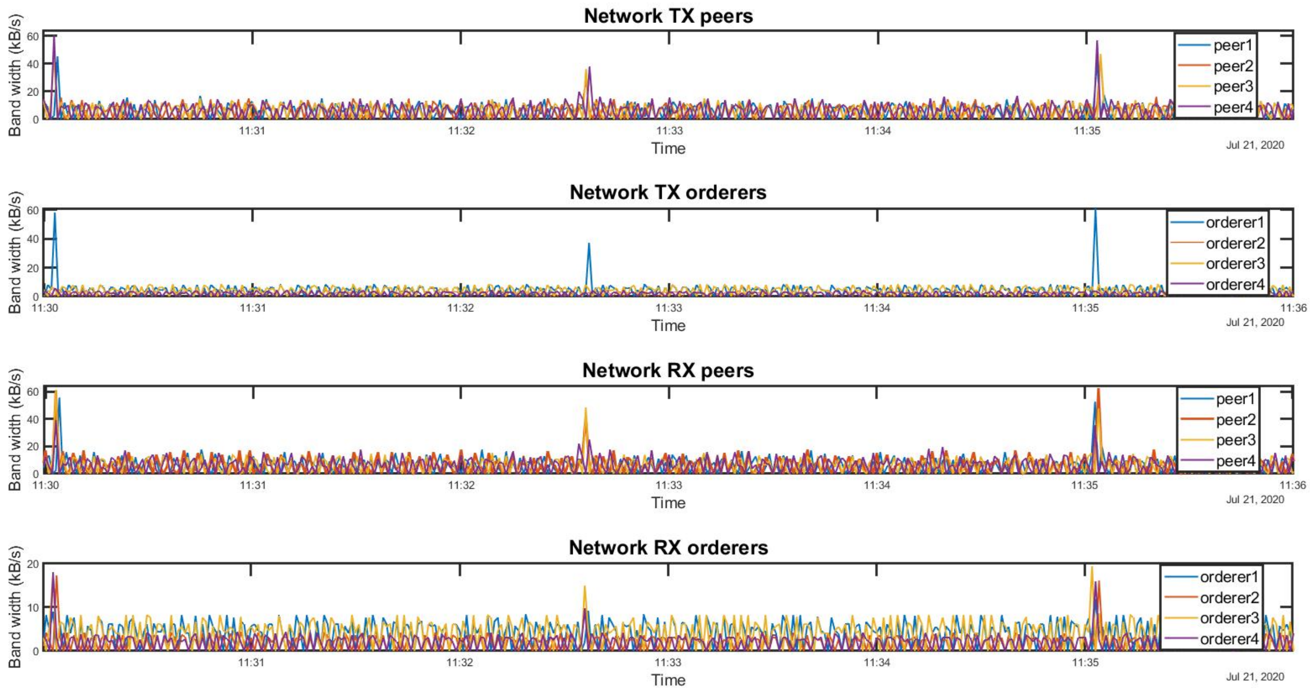

FIGURE 4. Bandwidth required by the peer and the orderer for both sending and receiving data in the test performed with four nodes. Every 5 minutes all the users send an offer to the market and in the middle of the period two transactions are made, collecting the data from the IEC 61850 server and matching the offers.

seen, which corresponds to the process of offer matching and that of reading the prosumers' IEC 61850 compatible devices. The magnitude of the peak values for the bandwidth varies according to the number of nodes making up the system (see TABLE 2). For the 16-node network, i.e. the worst-case scenario, the maximum bandwidth measured for uploading and downloading has been 356 kB/s and 302kB/s, respectively.

4) REQUIRED STORAGE

The data size in the BC becomes an important parameter which depends on the structure of the blocks in the Hyperledger Fabric framework [38]. The blocks consist of a header, a body which is composed of a variable number of transactions and the block metadata.

The number of transactions within a block depends on two factors, the maximum number of transactions the block can contain and the waiting time from the arrival of the first transaction until the block is formed. The number of transactions per block has been limited to 10 in this work because this way the best performance is achieved [38]. The timeout has been set at 1 second since no minor latencies are required for the correct operation of the system and the more transactions that enter the same block, the less storage required. Every transaction has three parts when it comes to creating a block: (i) the transaction proposal sent by a peer to endorsing peers; (ii) the transaction validation by the endorsing peers; and (iii) the response to the requested transaction by the smart contract invoked.

The block size has been determined through experiments on the 16-node blockchain where most of the nodes must verify the transaction before acceptance. Measurements revealed a block size ranging from 4 kB for one transaction to 32 kB for ten transactions.

Each SC execution is considered as a transaction. Therefore, there are four blocks with only one transaction in each round: (i) the electrical parameters are registered; (ii) the market is started (iii) the price is calculated; and (iv) offers are matched and the results are sent. In addition, users interested in buying or selling energy on the market send an offer (by the execution of another SC) simultaneously. This creates new blocks with a size between 1 and 10 transactions each.

Since the information contained in a transaction (alphanumeric data only) is small compared to the total size of the block, it can be assumed that all transactions in the system are of a similar size regardless of the transaction. Therefore, the storage required by the execution of a market round can be estimated with the following formula:

$$size_{round} = 4 \cdot size_{tx(MAX)} + size_{tx} \cdot N \tag{11}$$

where $size_{round}$ is the storage that is needed in a market round, $size_{tx(MAX)}$ is the storage required by a block with a single transaction, $size_{tx}$ the average storage used by a transaction in a block with several transactions and N the number of prosumers in the MG.

It is considered that the endorsement policy (section V-C-1) is fixed in a subset of 16 peers. Consequently, the size of the block is not increased as the number of prosumers grows

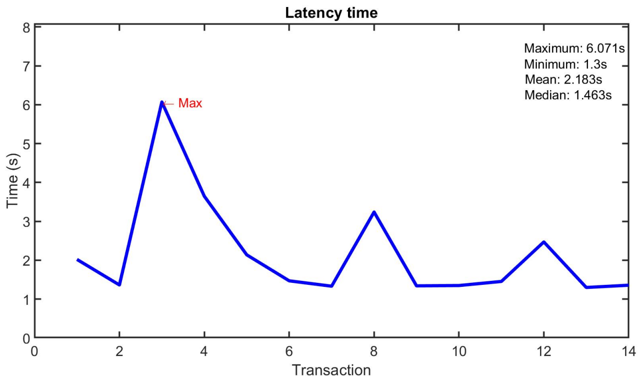

FIGURE 5. Latency for the different transactions of the 4-node test.

since the number of signatures is bound. For the worst-case scenario, the size of each transaction is 4 kB. Taking this into account, the number of prosumers participating in the system for a given storage capacity over a period of 20 years can be calculated. For instance, considering a memory of 1 TB, if a market round is performed every 5 minutes, the maximum number of prosumers is 107, whereas when market rounds are performed at 1-minute intervals, only 22 prosumers could participate.

In addition, some approaches have been adopted in which the BC size is reduced. Firstly, increasing the number of transactions inside a block, at the expense of increasing latency, result in a 20 % decrease of size (from 4 kB to 3,2 kB per transaction). Secondly, the number of market rounds that are carried out during the day can also be reduced using the proposed event-based strategy.

5) LATENCY

Different latencies can be considered. In this work, the latency refers to the waiting time that elapses between the execution of the transaction requested by the client application and the reception of the notification generated as a result of the request. This latency depends on the block creation time, which in the Hyperledger Fabric framework is set to 2 seconds by default. However, this value can be adjusted to the specific BC application being implemented. For the tests, the block creation time has been set to 1 second.

TABLE 3 shows the latency as a function of the number of nodes. The latencies were obtained by carrying out tests based on a single transaction at 5-minute intervals over one hour. Both the minimum and the median latency increase as the number of nodes grows. Furthermore, peak values of latency, above the usual range, occasionally appear (see FIGURE 5).

TABLE 4 depicts the latencies for the scenario in which every prosumer submits a transaction at the same time. It can be observed a decrease in the minimum and median latencies whereas the maximum latency taken up by a transaction is increased.

TABLE 3. Time delay for a single transaction.

Number of nodes	Minimum (s)	Maximum (s)	Median (s)
3	1,294	19,19	1,43
4	1,30	6,07	1,46
8	1,54	23,64	2,94
16	2,08	30,50	5,40

TABLE 4. Delay time taken to carry out several transactions simultaneously.

Number of nodes	Minimum (s)	Maximum (s)	Median (s)
3	1,223	22,76	1,30
4	0,95	12,54	1,00
8	0,70	25,22	1,83
16	1,38	34,97	5,92

VI. EXPERIMENTAL RESULTS

As a use case, a MG connected to the main network, is emulated. To replicate real residential consumption and PV energy production profiles, real data obtained from [39] is used. In addition, electricity prices of the Spanish electricity market, published by Red Eléctrica de España in the ESIOS portal [40] on a daily basis are also used. For the use case considered in this paper, the operation of the MG in island mode is not addressed. Therefore, the MG is always connected to the main grid. Moreover, since the use case is representing residential users, reactive energy billing is not taking into account.

The proposed MG comprises 18 heterogeneous prosumers, each one implemented in a Raspberry Pi 4 model B [33] as described in Section V. The 18 prosumers are categorized into three groups: (a) the first group is made up of 6 prosumers (1-6) with PV power generation and controllable and non-controllable loads; (b) the second group consists of 6 prosumers (7-12) with controllable and non-controllable loads, but no power generation capacity; and (c) the last group is composed of 6 prosumers (13-18) with only non-controllable loads. The details of each prosumer are described in TABLE 5.

The controllable loads, depicted in TABLE 5, are electric water heaters, one for each prosumer within the first and second group, i.e. prosumers from 1 to 12. Each heater has a rated power of 1.5 kW and a capacity of 3.6 kWh. It is assumed that these heaters have to be fully charged during the day to be completely emptied at the end of the day, emulating typical residential use. With this simple scenario, it is demonstrated how the BC-IEC 61850 proposal manages to improve the energy efficiency and the economic benefit of all prosumers.

For the study, a sunny day and a partially cloudy day are considered. A case of a very overcast day is not included because in that case there would hardly be any transactions

TABLE 5. Installed PV power and controllable loads of each prosumer in the use case scenario.

Prosumer	Installed PV (kW)	Heater	
		Power (kW)	Capacity (kWh)
1	3.75	1.5	3.6
2	2.5	1.5	3.6
3	1.75	1.5	3.6
4	1.25	1.5	3.6
5	4	1.5	3.6
6	1.5	1.5	3.6
7-12	---	1.5	3.6
13-18	---	---	---

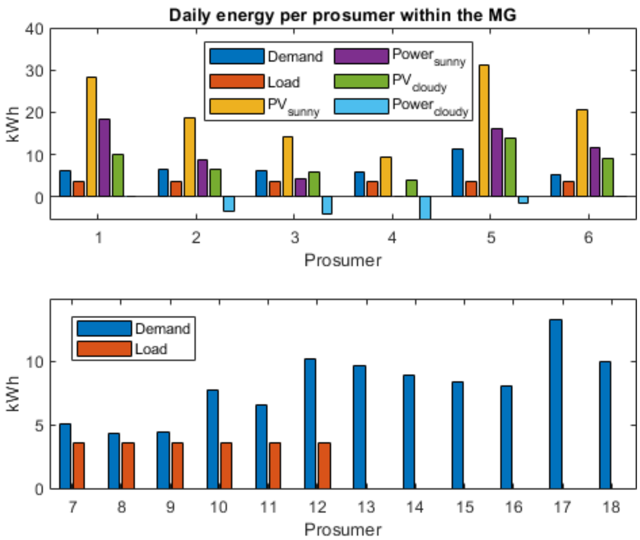

FIGURE 6. Spanish electricity market prices on a working day.

between the prosumers since the prosumer surplus of PV energy would be non-existent or very scarce.

FIGURE 6 illustrates the non-controllable and controllable load consumption of each prosumer per day, as well as the PV energy generated on the selected sunny and cloudy day. Additionally, the energy balance for each prosumer is shown for the two selected days. In both scenarios, the same profile of electricity consumption of non-controllable loads and the same profile of buying and selling grid prices are considered in order to make a more accurate comparison between both. In the case of PV generation, only the first 6 prosumers are displayed, as they are the only ones with installed PV power.

The electricity prices used in this use case are shown in FIGURE 7. As mentioned before, they are real prices from the Spanish electricity market [40] for a working day. It should be noted that in this market, it is possible to choose between a default billing or two period tariff, both are studied to validate the proposal.

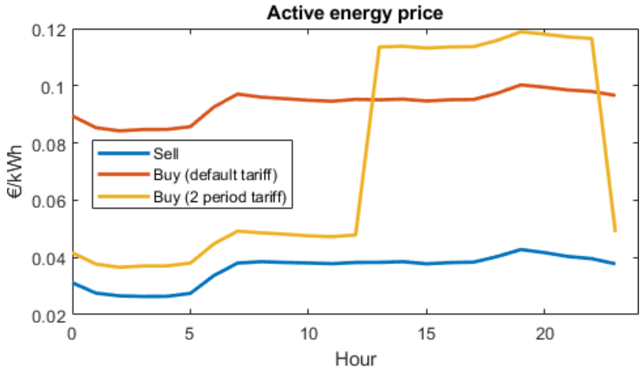

FIGURE 7. Energy consumed and generated by each prosumer on the sunny and the cloudy day under study.

Analysing the graph, the great difference in price between buying and selling energy to the grid is appreciated, which strengthens the justification of our market strategy. This is particularly noticeable during the peak period, from 13 to 23 hours, when the average price for selling energy to the grid is 0.039 €/kWh, and the buying price is 0.095 €/kWh for the default tariff and 0.113 euros/kWh for two period tariff.

A. TRANSACTION ANALYSIS

To evaluate the market update strategy, the sunny day profile data presented in FIGURE 7 is used. The study compares two different Thresholds for the SoD technique (1). The parameters to be evaluated are the number of updates made in the aperiodic market and therefore stored in the BC register and the energy estimation error committed by prosumer ($\mathrm{Error}_i\,(t)$) and the total error in the MG ($\mathrm{Error}_{MG}\,(t)$), evaluated by the following expressions:

$$\mathrm{Error}_i\,(t) = \int_{t_{i,k-1}}^{t} Energy_i\,(t) - Energy_i(t_{i,k-1})dt \quad (12)$$

$$Error_{MG}\,(t) = \sum\nolimits_{i=1}^{N} Error_i(t), \quad (13)$$

This error integrates the difference between the last energy consumption per minute that was sent to the MG and the consumptions that have actually occurred during the time the market has not been updated. In this way it is possible to quantify the error made between the amount of energy estimated in that time interval and that which has actually been delivered. TABLE 6 quantifies the results obtained after emulating the proposed strategy for the sunny day under study.

Instead of presenting all the individual results of the different prosumers, for space consideration, their statistical data is shown. The mean and standard deviation (SD) of the 18 prosumers are calculated. In addition, the total result of the MG is presented, being this the most significant information. The table details both the number of market updates and the error made in the energy estimate throughout the day. Comparing $\Delta_{SoD} = 0.025$ with SoD with $\Delta_{SoD} = 0.005$, shows that

TABLE 6. Number of event-based updates and power error rate in blockchain registration on a sunny day.

Aperiodic threshold SoD (kWh)		Mean per Prosumer	SD per Prosumer	MG
0.005	Updates	30.222	49.584	**399**
	Error (kWh)	0.050	0.063	**-0.424**
0.025	Updates	2.167	4.731	**39**
	Error (kWh)	0.533	0.408	**-8.1188**

the number of updates is significantly lower, but the error is higher. This allows the designer to set a trade-off between the number of updates and the desired performance, always keeping the punctual error limited with threshold (Δ_{SoD}).

B. HARDWARE DIMENSIONING

Based on the data obtained through the implementation of the BC-IEC 61850 strategy in the test bench described in Section V, it is possible to estimate the resources that are necessary to implement the strategy in the use case.

The selected device to implement the developed system is a 64-bit ARM processor with a Linux-based operating system. Based on the previous study carried out in Section V, the SBC used easily meets the computing power requirements for this use case.

Regarding the bandwidth, each prosumer needs a minimum of 1 MB/s. If a user had speed problems, he could operate without an orderer on his computer, which would significantly reduce the amount of bandwidth needed, with a 0.5 MB/s connection being enough to meet requirements.

The most critical point in the implementation of the BC in a system that is expected to work over a long period of time is the amount of storage required, since having an always growing and distributed database in all the nodes of the network can be a challenge, but thanks to the proposed event-based technique (1), this BC could be working for a great number of years.

In TABLE 7, it can be seen that depending on the threshold (Δ_{SoD}) used, a different number of daily transactions are made, and this has a direct impact on the number of years that the BC can be in operation. It presents a trade-off between the precision of the technique employed and the time it will be possible to keep the system functioning. In order to calculate this time, the worst-case scenario, i.e. maximum storage capacity required per update, is taken into account. For each update (9), each transaction requires 4 KB (section V-C-4).

From the table, the significance of the reduction in the number of updates is appreciated, and a comparison is made with the one-minute periodic implementation due to it is the minimum time step of the proposed event-based implementation. In addition, sporadic maximum latencies of up to 34 seconds have been observed during testing, so it is reasonable to set a minimum time between transactions of one minute. The proposed system is able to reduce the amount of information to be stored in the BC register database by a factor of 18, committing an error of less than 0.5 kWh per day in the entire MG. Even in the worst-case scenario, the most accurate event-based technique indicates that a 64 GB storage system is suitable for the MG with 18 prosumers and it could reliably operate for at least 33 years.

TABLE 7. Comparison of storage capacity requirements according to the technique used.

Technique	Tx per day	Size per day (MB)	Size per year (GB)	Years microSD 64 GB
T = 1 min	31680	123,75	44,1	1,45
SoD (0,005)	1596	5,46	1,94	33
SoD (0,025)	156	0,53	0,19	336

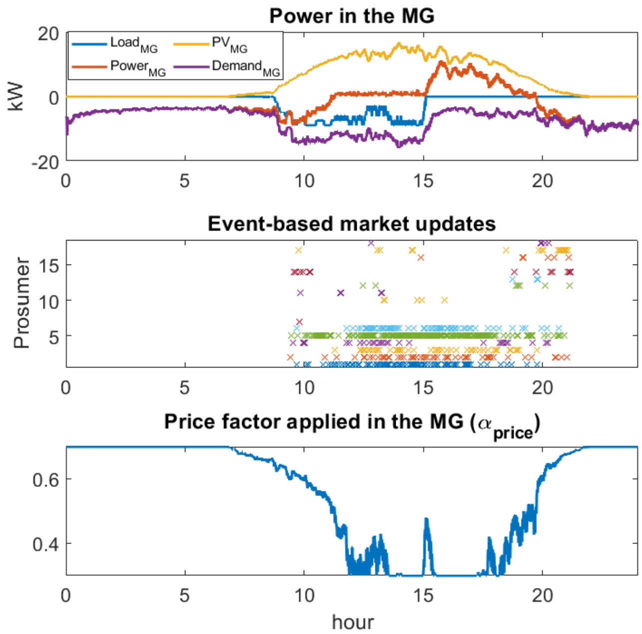

FIGURE 8. Sunny day use case: MG power profile throughout the day, updates of each prosumer and the price factor applied at each moment of the day.

C. USE CASE RESULTS

Finally, the results obtained for two types of days with the selected threshold ($\Delta_{SoD} = 0.005$ kWh) are presented. The energy profiles are those presented in FIGURE 6 and the prices are obtained from FIGURE 7.

In the first instance, FIGURE 8 shows the results for the sunny day. The graph shows the MG power profile throughout the day, the updates of each prosumer obtained from (1) and the price factor applied at each moment of the day (α_{price}) obtained from (6).

In the upper graph, the total power within the MG is shown. These power values are calculated as the sum of the PV power produced at each moment by each prosumer, in yellow; the sum of all the loads of each prosumer at each moment,

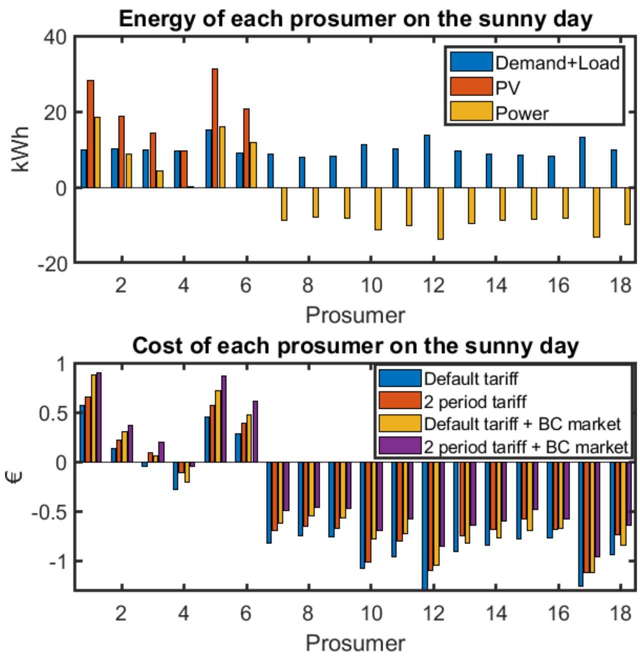

FIGURE 9. Sunny day use case: Economic study.

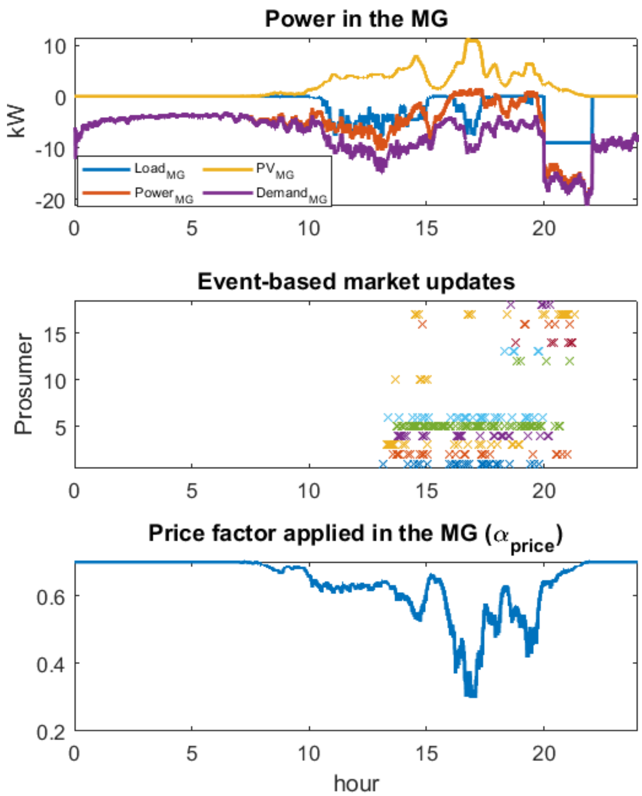

FIGURE 10. Cloudy day use case: MG power profile throughout the day, updates of each prosumer and the price factor applied at each moment of the day.

in purple; the sum of the controllable loads, in blue; and the power balance in the MG resulting from the difference in the generated energy minus the energy consumed, in orange. Analysing this graph, it can be seen how the production of the PV systems takes place between 7 and 21 hours. In the first hours the generation is low, so the energy is consumed locally by each prosumer, therefore no market event takes place. From 9 hours on, there are prosumers who begin to have surpluses, which activates the market. In the following hours, all surplus energy is absorbed by the controllable loads of the different prosumers. This can be seen in the energy balance signal around zero until approximately 17 hours. From that moment on, all the water heaters are fully charged, which means that the energy demand decreases sharply and a positive energy balance starts to be achieved in the MG. This surplus energy is sold to the grid.

The intermediate graph presents the moments of market activation and the prosumer that activates them. As commented previously, these events occur between 9 and 21 hours because these are the moments in which some prosumer has a surplus of PV energy. The number of events generated by each prosumer depends on the amount of variation in their energy balance over time, the total events in the MG are 399.

Finally, at the bottom graph, the price factor is shown for each instant of time. As expected, this factor is higher in the initial and final hours of the day because these are the moments when a smaller amount of surplus PV energy is available.

FIGURE 9 shows the economic study of the proposal applying the strategy described in section IV-C. The upper graph represents the amount of PV energy produced by each prosumer, in orange, the amount energy consumed, in blue, and the energy balance, in yellow, for the entire day. The lower graph depicts the profit obtained (positive gain/negative loss) by each prosumer in four different scenarios:: (a) without the developed strategy for the default tariff; (b) without the developed strategy for the two period tariff; (c) with the MG strategy for the default tariff; and (d) with the MG strategy for the two period tariff. In the graph, it can be seen how significant the increase in profit of the energy producers is, as well as the savings of those who only consume, both for the two period tariff and the default tariff. The total energy balance of the MG is -58.52 kWh. The total cost of the MG, calculated as the sum of the individual costs of all prosumers, when the strategy is not applied is 10.03€ and 7.62€ for the default tariff and for the two period tariff, respectively. However, when the strategy is applied these total costs are reduced to 6.95€ and 4.52€ respectively. Therefore, for a sunny day, the proposed strategy achieves a significant saving in costs of 30,75% and 40% for the default tariff and for the two period tariff, respectively.

In the second instance, FIGURE 10 shows the results for the cloudy day. As in the previous case, it presents the MG power profile throughout the day, the updates of each prosumer and the price factor applied at each moment of the day. In this case, it can be seen that the surplus PV energy of the prosumers is more limited, so all the surplus produced is absorbed by the MG, for this reason the energy balance in MG is almost always below zero. Since not all the heaters can be fully charged with excess energy after 20 hours, the remaining

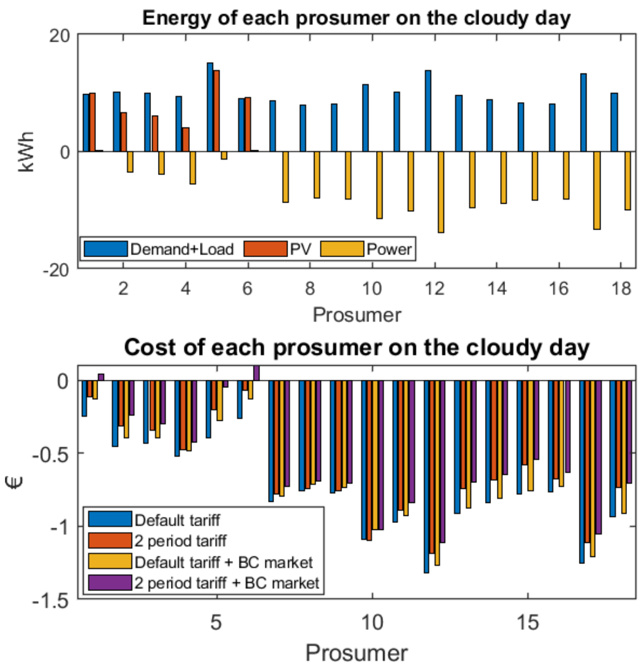

FIGURE 11. **Cloudy day use case: Economic study.**

capacity is charged with energy from the grid. This results in the peak consumption from 20 to 22 hours. The shortage of surplus of PV energy compared with the sunny day also justifies: the lower number of market activation events and the fact that the price factor of MG energy is almost always above 0.5 as it is a case where energy is more expensive due to lower PV production. The number of events and the error (Error_{MG}), calculated with (13), for an entire day in the MG are 235 and -0.6092 kWh respectively.

FIGURE 11 shows the economic study for the case of the cloudy day. In this case, the benefits produced are less than those of the sunny day because fewer transactions can be made. However, it is worth highlighting that despite having less surplus of energy available, all prosumers achieve a small economic benefit. Analysing the results achieved on a cloudy day, the balance of energy of the MG is -132,01 kWh. The total cost of the MG, calculated as the sum of the individual costs of all prosumers, when the strategy is not applied is 13,53€ and 11,52€ for the default tariff and for the two period tariff, respectively. However, when the strategy is applied these total costs are reduced to 12,55€ and 10.23€ respectively. Therefore, for a cloudy day, the proposed strategy achieves a significant saving in costs of 7,22% and 11,22% for the default tariff and for the two period tariff, respectively.

VII. CONCLUSION AND FUTURE WORK

This paper addresses one of the main technical challenges of the energy sector on account of the increasing number of DERs mainly based on renewable energy: the shift from a centralized operational approach to a distributed generation paradigm. This has encouraged the advent of MGs to propose new business models and management strategies. Within this context, this paper introduces an efficient management strategy, which is aimed at obtaining a fair division of costs billed by the utilities, without relying on a centralized utility or MG aggregator. The management strategy relies on the design of a local event-based energy market within the MG. This local market is based on the integration of the IEC 61850 standard into BC Smart Contracts, which facilitates the distributed communication among the commercial devices complying with the standard. The approach is implemented using low cost off-the-shelf hardware, such as the Raspberry Pi 4 model B platform, which reduces the time for the return on the investment. Consequently, the proposed strategy becomes an economically feasible solution for residential environments. The development of an event-based market also results in a reduction in the amount of computation and communication resources required, and more importantly, without negatively affecting the system performance. In addition, the proposed pricing strategy provides a win-win energy price for both energy producers and consumers, taking advantage of the gap between the price paid for the electricity consumed and that generated and injected to the grid. In the use case scenario, it is demonstrated that the proposed system is able to reduce the amount of information to be stored in the BC register database by a factor of 18. Furthermore, the error introduced is less than 0.5 kWh per day and for the entire MG. Finally, the strategy allows to achieve energy price savings up to 40%.

Future work will address the design of an islanded strategy, supported by batteries installed within the prosumers and the implementation of the BC-IEC 61850 in a real MG.

REFERENCES

[1] M. F. Akorede, H. Hizam, and E. Pouresmaeil, "Distributed energy resources and benefits to the environment," *Renew. Sustain. Energy Rev.*, vol. 14, no. 2, pp. 724–734, Feb. 2010.

[2] H. Kanchev, D. Lu, F. Colas, V. Lazarov, and B. Francois, "Energy management and operational planning of a microgrid with a PV-based active generator for smart grid applications," *IEEE Trans. Ind. Electron.*, vol. 58, no. 10, pp. 4583–4592, Oct. 2011.

[3] S. Grijalva and M. U. Tariq, "Prosumer-based smart grid architecture enables a flat, sustainable electricity industry," in *Proc. ISGT*, Jan. 2011, pp. 1–6.

[4] V. Madani, R. Das, F. Aminifar, J. McDonald, S. S. Venkata, D. Novosel, A. Bose, and M. Shahidehpour, "Distribution automation strategies challenges and opportunities in a changing landscape," *IEEE Trans. Smart Grid*, vol. 6, no. 4, pp. 2157–2165, Jul. 2015.

[5] R. H. Lasseter, "MicroGrids," in *Proc. IEEE Power Eng. Soc. Winter Meeting*, Jan. 2002, pp. 305–308.

[6] E. Mengelkamp, J. Gärttner, K. Rock, S. Kessler, L. Orsini, and C. Weinhardt, "Designing microgrid energy markets: A case study: The Brooklyn Microgrid," *Appl. Energy*, vol. 210, pp. 870–880, Jan. 2018.

[7] Y. Yuan and F.-Y. Wang, "Towards blockchain-based intelligent transportation systems," in *Proc. IEEE 19th Int. Conf. Intell. Transp. Syst. (ITSC)*, Nov. 2016, pp. 2663–2668.

[8] A. Banafa, "IoT and blockchain convergence: Benefits and challenges," *IEEE Internet Things*, 2017. [Online]. Available: https://iot.ieee.org/newsletter/january-2017/iot-and-blockchain-convergence-benefits-and-challenges.html

[9] S. Underwood, "Blockchain beyond bitcoin," *Commun. ACM*, vol. 59, no. 11, pp. 15–17, Oct. 2016.

[10] F. Knirsch, A. Unterweger, and D. Engel, "Privacy-preserving blockchain-based electric vehicle charging with dynamic tariff decisions," *Comput. Sci. Res. Develop.*, vol. 33, nos. 1–2, pp. 71–79, Feb. 2018.

[11] T. Morstyn, A. Teytelboym, and M. D. McCulloch, "Designing decentralized markets for distribution system flexibility," *IEEE Trans. Power Syst.*, vol. 34, no. 3, pp. 2128–2139, May 2019.
[12] N. Ul Hassan, C. Yuen, and D. Niyato, "Blockchain technologies for smart energy systems: Fundamentals, challenges, and solutions," *IEEE Ind. Electron. Mag.*, vol. 13, no. 4, pp. 106–118, Dec. 2019.
[13] G. Wood, "Ethereum: A secure decentralised generalised transaction ledger," *Ethereum Project Yellow Paper*, vol. 151, pp. 1–32, Apr. 2014.
[14] S. Nakamoto. (2008). *Bitcoin: A Peer-to-Peer Electronic Cash System*. [Online]. Available: https://bitcoin.org/bitcoin.pdf
[15] M. Andoni, V. Robu, D. Flynn, S. Abram, D. Geach, D. Jenkins, P. McCallum, and A. Peacock, "Blockchain technology in the energy sector: A systematic review of challenges and opportunities," *Renew. Sustain. Energy Rev.*, vol. 100, pp. 143–174, Feb. 2019.
[16] M. L. Di Silvestre, P. Gallo, M. G. Ippolito, E. R. Sanseverino, and G. Zizzo, "A technical approach to the energy blockchain in microgrids," *IEEE Trans. Ind. Informat.*, vol. 14, no. 11, pp. 4792–4803, Nov. 2018.
[17] S. M. S. Hussain, A. Tak, T. S. Ustun, and I. Ali, "Communication modeling of solar home system and smart meter in smart grids," *IEEE Access*, vol. 6, pp. 16985–16996, 2018.
[18] S. M. S. Hussain, M. A. Aftab, I. Ali, and T. S. Ustun, "IEC 61850 based energy management system using plug-in electric vehicles and distributed generators during emergencies," *Int. J. Electr. Power Energy Syst.*, vol. 119, Jul. 2020, Art. no. 105873.
[19] S. Marzal, R. Salas, R. González-Medina, G. Garcerá, and E. Figueres, "Current challenges and future trends in the field of communication architectures for microgrids," *Renew. Sustain. Energy Rev.*, vol. 82, pp. 3610–3622, Feb. 2018.
[20] T. S. Ustun, C. Ozansoy, and A. Zayegh, "Modeling of a centralized microgrid protection system and distributed energy resources according to IEC 61850-7-420," *IEEE Trans. Power Syst.*, vol. 27, no. 3, pp. 1560–1567, Aug. 2012.
[21] S. M. S. Hussain, M. A. Aftab, F. Nadeem, I. Ali, and T. S. Ustun, "Optimal energy routing in microgrids with IEC 61850 based energy routers," *IEEE Trans. Ind. Electron.*, vol. 67, no. 6, pp. 5161–5169, Jun. 2020.
[22] W. Shi, X. Xie, C.-C. Chu, and R. Gadh, "Distributed optimal energy management in microgrids," *IEEE Trans. Smart Grid*, vol. 6, no. 3, pp. 1137–1146, May 2015.
[23] I. Ali and S. M. S. Hussain, "Control and management of distribution system with integrated DERs via IEC 61850 based communication," *Eng. Sci. Technol., Int. J.*, vol. 20, no. 3, pp. 956–964, Jun. 2017.
[24] I. Ali and S. M. Suhail Hussain, "Communication design for energy management automation in microgrid," *IEEE Trans. Smart Grid*, vol. 9, no. 3, pp. 2055–2064, May 2018.
[25] *Communication Networks and Systems for Power Utility Automation—Part 7-420: Basic Communication Structure—Distributed Energy Resources Logical Nodes*, document IEC 61850-7-420:2009, International Electrotechnical Commision, 2009.
[26] T. Yang, Q. Guo, X. Tai, H. Sun, B. Zhang, W. Zhao, and C. Lin, "Applying blockchain technology to decentralized operation in future energy Internet," in *Proc. IEEE Conf. Energy Internet Energy Syst. Integr. (EI)*, Nov. 2017, pp. 1–5.
[27] N. Wang, X. Zhou, X. Lu, Z. Guan, L. Wu, X. Du, and M. Guizani, "When energy trading meets blockchain in electrical power system: The state of the art," *Appl. Sci.*, vol. 9, no. 8, p. 1561, Apr. 2019.
[28] R. E. Mackiewicz, "Overview of IEC 61850 and benefits," in *Proc. IEEE Power Eng. Soc. General Meeting*, Jun. 2006, p. 8.
[29] C. Santos, J. A. Jimenez, and F. Espinosa, "Effect of event-based sensing on IoT node power Efficiency. Case study: Air quality monitoring in smart cities," *IEEE Access*, vol. 7, pp. 132577–132586, 2019.
[30] J. M. Zepter, A. Lüth, P. Crespo del Granado, and R. Egging, "Prosumer integration in wholesale electricity markets: Synergies of peer-to-peer trade and residential storage," *Energy Buildings*, vol. 184, pp. 163–176, Feb. 2019.
[31] Z. Zheng, S. Xie, H. Dai, X. Chen, and H. Wang, "An Overview of Blockchain Technology: Architecture, Consensus, and Future Trends," in *Proc. IEEE Int. Congr. Big Data (BigData Congr.)*, Jun. 2017, pp. 557–564.
[32] Hyperledger. *Hyperledger Fabric*. Accessed: Jun. 2020. [Online]. Available: https://hyperledger-fabric.readthedocs.io/en/release-2.1/
[33] Raspberry Pi Foundation. *RaspberryPi*. Accessed: Aug. 19, 2020. [Online]. Available: https://www.raspberrypi.org/products/raspberry-pi-4-model-b/
[34] R. Longbottom, "Raspberry Pi 4B 64 bit benchmarks and stress tests," unpublished, 2019. [Online]. Available: https://www.researchgate.net/publication/337165767_Raspberry_Pi_4B_64_Bit_Benchmarks_and_Stress_Tests, doi: 10.13140/RG.2.2.33099.54562.
[35] MZ Automation GmbH. (Mar. 2020). *libiec61850*. Accessed: Aug. 10, 2020. [Online]. Available: https://libiec61850.com/libiec61850/downloads/
[36] M. Gayo. (Mar. 2020). *Docker Hub*. [Online]. Available: https://hub.docker.com/u/miguelgayo
[37] (Mar. 2020). *Apache*. [Online]. Available: https://couchdb.apache.org/
[38] P. Thakkar, S. Nathan, and B. Viswanathan, "Performance benchmarking and optimizing hyperledger fabric blockchain platform," in *Proc. IEEE 26th Int. Symp. Modeling, Anal., Simulation Comput. Telecommun. Syst. (MASCOTS)*, Sep. 2018, pp. 264–276.
[39] Open Power System Data. (Apr. 15, 2020). *Open Power System Data*. Accessed: Jul. 2020. [Online]. Available: https://data.open-power-system-data.org/household_data/2020-04-15/
[40] REE. (2020). *ESIOS*. Accessed: Aug. 2020. [Online]. Available: https://www.esios.ree.es/es

MIGUEL GAYO received the B.S. degree in industrial electronics and automatic engineering and the M.Sc. degree in industrial engineering from the University of Alcalá, Alcalá de Henares, Spain, in 2017 and 2019, respectively, where he is currently pursuing the Ph.D. degree with the Advanced Electronic Systems Program.

He worked in the private energy sector for two years. He is currently with the Department of Electronics, University of Alcalá, with a Research Contract funded by the Comunidad de Madrid and the European Social Fund to research in the field of microgrids. His research interests include the areas of renewable energies, blockchain, microgrids, and energy management systems

CARLOS SANTOS received the B.S. degree in telecommunications engineering and the M.Sc. degree in electrical engineering from the University of Alcalá, Spain, in 2010 and 2011, respectively, and the Ph.D. degree in electronics in 2016.

He is currently with the Department of Electronics, University of Alcalá, with a Postdoctoral Research Contract. His research interest include the field of fusion algorithms, forecasting strategies, varying-time sampling control techniques, energy management systems, virtual power plants, and smart grids.

FRANCISCO JAVIER RODRÍGUEZ SÁNCHEZ (Member, IEEE) received the B.Sc. degree in technical telecommunication engineering from the University of Alcalá, Alcalá de Henares, Spain, in 1985, the M.Sc. degree in telecommunication from the Technical University of Madrid, Madrid, Spain, in 1990, and the Ph.D. degree in electronics engineering from the University of Alcalá, in 1997.

He worked in the private electronic industry for two years. Since 1986, he has been a Lecturer with the Department of Electronics, University of Alcalá, where he is currently a Professor. He is the author of more than 160 refereed publications in international journals, book chapters, and conference proceedings. He has also directed more than 55 investigation projects funded by public institutions and private industry. His research interests include the areas of smart grids, microgrids, renewable energies, control electronics, and real-time processing.

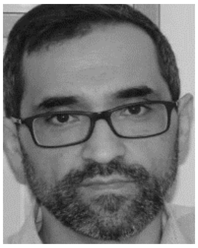

PEDRO MARTÍN received the Telecommunications degree from the Polytechnic University of Madrid, Spain, in 1994, and the Ph.D. degree in telecommunications engineering from the University of Alcalá, Spain, in 2000.

He currently works as an Associate Professor with the Department of Electronics, University of Alcalá. He is a member of the research group ''Electronics Engineering applied to the Renewable Energies.'' His research activities include the design of embedded systems for power electronic systems and smart grids.

JOSÉ A. JIMÉNEZ received the Electronic Telecommunication Engineering degree from the University of Valencia, Spain, in 1996, and the Ph.D. degree from the University of Alcalá, Spain, in 2004. He is currently an Associate Professor of Instrumentation Electronics with the Electronics Department, University of Alcalá. His research areas include multi-sensor integration, sensorial systems, instrumentation, and electronic systems applied to smart grid and smart cities.

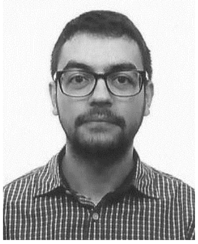

MIGUEL TRADACETE was born in Cuenca, Spain, in 1994. He received the Industrial Electronics and Automatic Engineering degree from the University of Alcalá, where he is currently pursuing the master's degree in electronic engineering.

From 2017 to 2018, he was a Scholarship Researcher with the University of Alcalá, where he has been a Teaching and Research Academic Staff with the Department of Electronics, since 2018. He is author of three articles in the autonomous driving field. His research interests include robotics, electric vehicles, autonomous driving, renewable energy generation, micro-grid systems, and energy management systems.

sensors

Article

Turning Base Transceiver Stations into Scalable and Controllable DC Microgrids Based on a Smart Sensing Strategy

Miguel Tradacete [1], Carlos Santos [2], José A. Jiménez [1], Fco Javier Rodríguez [1,*], Pedro Martín [1], Enrique Santiso [1] and Miguel Gayo [1]

[1] Department of Electronics, University of Alcalá, Alcalá de Henares, 28805 Madrid, Spain; miguel.tradacete@edu.uah.es (M.T.); jose.jimenez@uah.es (J.A.J.); pedro.martin@uah.es (P.M.); enrique.santiso@uah.es (E.S.); miguel.gayo@uah.es (M.G.)

[2] Department of Signal Theory and Communications, University of Alcalá, Alcalá de Henares, 28805 Madrid, Spain; carlos.santos@uah.es

* Correspondence: franciscoj.rodriguez@uah.es; Tel.: +34-91-885-6561

Abstract: This paper describes a practical approach to the transformation of Base Transceiver Stations (BTSs) into scalable and controllable DC Microgrids in which an energy management system (EMS) is developed to maximize the economic benefit. The EMS strategy focuses on efficiently managing a Battery Energy Storage System (BESS) along with photovoltaic (PV) energy generation, and non-critical load-shedding. The EMS collects data such as real-time energy consumption and generation, and environmental parameters such as temperature, wind speed and irradiance, using a smart sensing strategy whereby measurements can be recorded and computing can be performed both locally and in the cloud. Within the Spanish electricity market and applying a two-tariff pricing, annual savings per installed battery power of 16.8 euros/kW are achieved. The system has the advantage that it can be applied to both new and existing installations, providing a two-way connection to the electricity grid, PV generation, smart measurement systems and the necessary management software. All these functions are integrated in a flexible and low cost HW/SW architecture. Finally, the whole system is validated through real tests carried out on a pilot plant and under different weather conditions.

Keywords: base transceiver stations (BTS); microgrid; green communications; energy management systems (EMS); IEC61850 standard; embedded systems for Internet of Things (IoT); monitoring and control systems; photovoltaic distributed generation

Citation: Tradacete, M.; Santos, C.; Jiménez, J.A.; Rodríguez, F.J.; Martín, P.; Santiso, E.; Gayo, M. Turning Base Transceiver Stations into Scalable and Controllable DC Microgrids Based on a Smart Sensing Strategy. *Sensors* **2021**, *21*, 1202. https://doi.org/10.3390/s21041202

Academic Editor: Hossam A. Gabbar

Received: 30 December 2020

Accepted: 4 February 2021

Published: 9 February 2021

1. Introduction

In the last two decades, there has been a growing demand for Base Transceiver Stations (BTSs) due to the development of mobile communication networks with smaller cells and BTSs closer to the users. From the network operator (NO) point of view, BTSs are the main source of energy consumption. A decade ago, virtually 60% of the energy consumption of mobile phone operators was directly attributed to the equipment installed in the BTSs [1]. However, with the advent of the fourth (4G) or Long-Term Evolution (LTE) and fifth generation (5G) networks, the amount of traffic volume in the mobile networks has considerably grown, which has led to an increase in the total energy consumption, and therefore, in the carbon footprint generated. Moreover, 5G networks require between two and three times the number of BTSs compared to those installed for the legacy mobile generations [2]. Although 5G has been designed to be more energy efficient than the previous generations [3], the deployment of BTSs for 5G will increase the energy consumption by 5% [4]. As a result, the costs in terms of capital expenditure (CapEx) and operational expenditure (OpEx) will steadily rise. Enhancing the energy efficiency of telecommunication networks becomes a significant contribution when it comes to fighting global warming. However, in the context of rapidly rising energy prices, it is also creating economic opportunities [5]. Currently, energy consumption is regarded as an important performance indicator of the equipment comprising the BTSs [6]. This is stated in the European Telecommunications Standards Institute (ETSI) standard [7] and in 3GPP (3rd Generation Partnership Project) specifications [8].

For many years in the design of mobile networks, the focus has always been on increasing the user throughput and the service provider capacity, without taking energy efficiency and environmental impact into consideration. However, the last decade has seen a change of emphasis and improving energy efficiency within BTSs has become strategically vital, not only for financial reasons, reducing costs, but also for developing a more self-sustainable network of BTSs, which clearly has a positive impact on the corporate brand image of the network operators (NOs). Several projects, such as EARTH [9], ECONET [10], co-funded by the European Commission under the Framework Programme 7 (FP7), and GreenTouch [11] and 5GrEEn [12], have been carried out, which shows the growing public and private concern about this field. Finally, OPERA-Net and OPERA-Net 2 [13] are other projects which stand out in the field of energy efficiency and low-cost implementation for Mobile Radio Access Networks.

In the literature, two approaches have mainly been put forward to address this problem: (i) energy saving strategies, also called power saving [14], which take into account the traffic load, which is based on real-time data traffic and advocates the use of energy-efficient components to improve the energy consumption of the BTS at the hardware level; and (ii) the use of renewable sources of energy as main power sources for BTSs to reduce the electricity bill and the negative environmental impact of conventional fossil fuel-based energy resources due to their carbon footprint [15].

As for the use of renewable energy, sustainable BTSs have become a real solution to the problem. BTS configurations range from standalone solar powered BTSs with storage batteries, to grid-connected ones, in which the grid provides power to the BTS when the photovoltaic system (PVS) and the battery energy storage system (BESS) do not provide enough power. Hybrid configurations can also be found, which integrate different renewable sources such as wind and solar energy along with conventional energy sources such as diesel generators [16–18]. The authors in [19–21] carried out a detailed analysis of the technical and economic feasibility for different configurations used to power BTSs. However, to the best of the author's knowledge, there are no research studies which focus on the economic benefit derived from considering a BTS as an MG in terms of optimal energy flow control. Needless to say, achieving energy efficiency needs to go hand in hand with providing uninterruptible and reliable power supply to the critical loads for operation. In this regard, BTSs powered by only solar energy pose a challenge of dimensioning the PV system and the Battery Energy Storage System (BESS) [22]. On the other hand, in grid-connected BTSs, when a power outage occurs, the communication networks should remain operative. Moreover, a BTS based on renewable energy without an operational strategy may increase the OpEx, thereby delaying the return on the initial investment and making this alternative less attractive for network operators. Design of an operational strategy must consider the BTS energy profile in terms of the energy consumed by each component, and thus, the energy allocation per function within the BTS. This topic has been properly researched in [23,24], showing that the radio equipment and amplifiers account for more than 60% of the power consumed; 11% is due to the DC power system, while the cooling equipment is responsible for 25% of the power consumed. Therefore, an optimal design of the radio equipment and the cooling system can reduce the power drawn by the BTS. Likewise, it is very important to develop strategies directed towards BTS Energy Savings, which can be applied to both the radio equipment, e.g., radio sleep mode [25], and to the cooling, e.g., passive cooling, advanced climate control [26] and power electronics. Additionally, the forecasting of the available energy from renewables should be considered due to their stochastic nature, and the electricity price, battery health and lifespan, charging and discharging cycles for the BESS etc. are also required. Hence, an intelligent energy management of the BTS components has to be adopted.

To develop the above-mentioned operational strategy, a microgrid (MG) paradigm can be used to model a BTS, consisting of a low-voltage network (DC and/or AC) that integrates renewable energy sources (RES), a BESS and controllable loads connected to the main grid. To provide the MG-based BTS with intelligent energy management, a local controller and an Energy Management System (EMS) should be implemented. By supervising and coordinating the operation of the sources of renewable energy, the BESS, the controllable loads (critical and non-critical) and the network devices, the BTS performance can be improved.

The operation of an MG-based BTS should be based on a sensing system for determining the value of electrical and environmental parameters. In [27], a comprehensive review of several PV sensing systems is presented. Overall, these systems have either a high cost [28] or reveal limitations regarding the number and type of the parameters to be measured [29]. The practical application of monitoring systems poses many challenges, such as the harsh environmental conditions the different components must withstand and the degradation of the electrical components e.g., connector corrosion, resource restrictions with respect to the energy efficiency, real-time constraints and low-cost implementations, to name but a few [27]. To successfully address these challenges, the monitoring system proposed in this paper is based on up-to-date technologies which guarantee real-time operating conditions, low energy consumption, protection against harsh environmental conditions, firmware OTA updating, local and cloud-based data storage, high computational capacity, accurate measurements and support for several communication protocols, e.g., I2C, SPI, Modbus and MQTT, implementing a low-cost approach. Another strength of this approach is that the system not only monitors the BTS variables but also is able to control the energy flow among the different elements comprising the BTS. This is carried out by an EMS algorithm developed for this application.

The scalable MG-based architecture for BTSs described in this paper includes the following features:

1. Transformation of BTSs in scalable and controllable DC Microgrids to reduce the OpEx. For this purpose, an Energy Management System (EMS) is developed. EMS manages the energy flow in the MG-based BTS based on different scenarios as described in Section 4.
2. The BTS is modeled on the IEC 61850 standard, which improves interoperability and scalability, supporting, in the future, the integration of new BTSs. The equipment used in BTSs are usually manufactured by different vendors overlooking the interoperability between these devices. Thus, a significant advantage of using the IEC 61850 is that it facilitates future extensions.
3. The data collection scheme is based on the cloud from where the information becomes available. This provides always-on, real-time data collecting and the possibility of cloud computing for real-time management.
4. The hardware/software (HW/SW) architecture within the BTS is implemented by using low-cost off-the-shelf hardware. This reduces the time for the return of investment and becomes an economically feasible solution for network operators.

The main contributions of the paper are summarized as follows: (i) the design of a scalable architecture to turning BTSs into Scalable and Controllable DC Microgrids which can be applied to any type of BTS; (ii) the architecture is based on the IEC 61850 standard, which enables the distributed communication among the BTSs; (iii) the low-cost hardware implementation of the system, which decreases the time for return on the investment, making it more attractive for network operators; (iv) the proposed architecture lays the foundations to allow several BTSs to work cooperatively, sharing energy among them and injecting the surplus energy to the grid. In short, it allows a set of controllable MG-based BTSs to be aggregated through a centralized management in the shape of a Virtual Power Plant (VPP) [30,31]; (v) implementation of an EMS which focuses on optimizing the monetary benefits obtained by managing the charging and discharging of a BESS along with the production of photovoltaic (PV) energy and the shedding of non-critical loads;

(vi) the development of a smart sensing strategy, as all the sensors have communication capabilities, smart processing based on low-cost hardware and cloud computing facilities for PV forecasting. This allows several BTSs to work cooperatively.

In the literature, there are virtually no works dealing with the transformation of a conventional BTS into a scalable and controllable DC MG. An experimental setup has been developed to validate the approach.

The remainder of this paper is organized as follows. Section 2 describes the conventional BTS layout and the proposed BTS architecture. Section 3 described in detail the proposed MG-based BTS. Results are presented in Section 4. Finally, conclusions are drawn and future work is outlined in Section 5.

2. Architecture of the Microgrid-Based Base Transceiver Station (MG-Based BTS)

In this section, the proposed architecture for the MG-based BTS is described. To evaluate the degree of the transformation, the conventional BTS is first introduced.

2.1. Conventional Base Transceiver Station

Figure 1 shows the architecture of a conventional grid-connected BTS without renewable energy generation nor local controller.

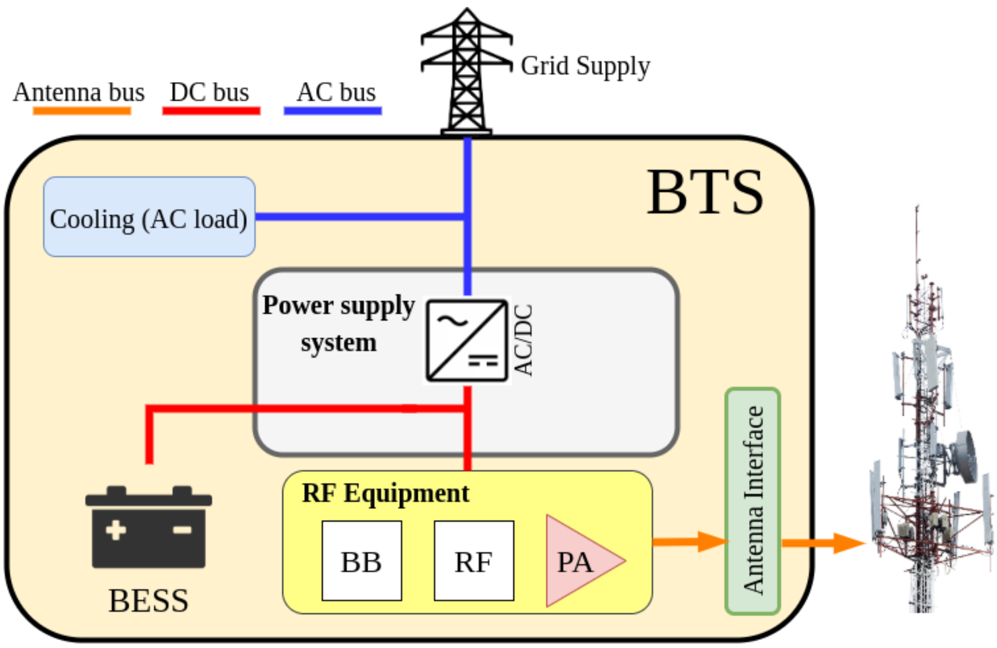

Figure 1. Conventional BTS architecture.

This BTS layout can be applied to any BTS regardless of the type [9]. As seen in Figure 1, the BTS consists of a grid-connected power supply system which integrates a rectifier, the BESS unit, the Base Band unit (BB), the Radio Frequency (RF) unit, the Power Amplifier (PA) and different AC loads, such as the cooling system and lighting. The DC output of the rectifier is connected to: (i) the BESS, which acts as a backup source to facilitate continuous operation in case of a power outage; (ii) the transmission/reception equipment (RF, PA and BB). The grid-connected power supply system manages the charge of the BESS.

A power modeling approach for conventional BTSs can be found in [32], in which, at the time of publication, it was estimated that, in a full-load scenario, the power demand by BTSs would be reduced by 50% and 20%, respectively, from 2014 to 2020. With this power estimation in mind, the BESS size is determined as a function of the required autonomy, i.e., the amount of time the BESS can power the BTS uninterruptedly to ensure 100% operability in case of a power outage.

2.2. Proposed Architecture for the MG-Based BTS

Figure 2 depicts the block diagram of the proposed architecture for a grid connected BTS with solar generation based on a microgrid architecture.

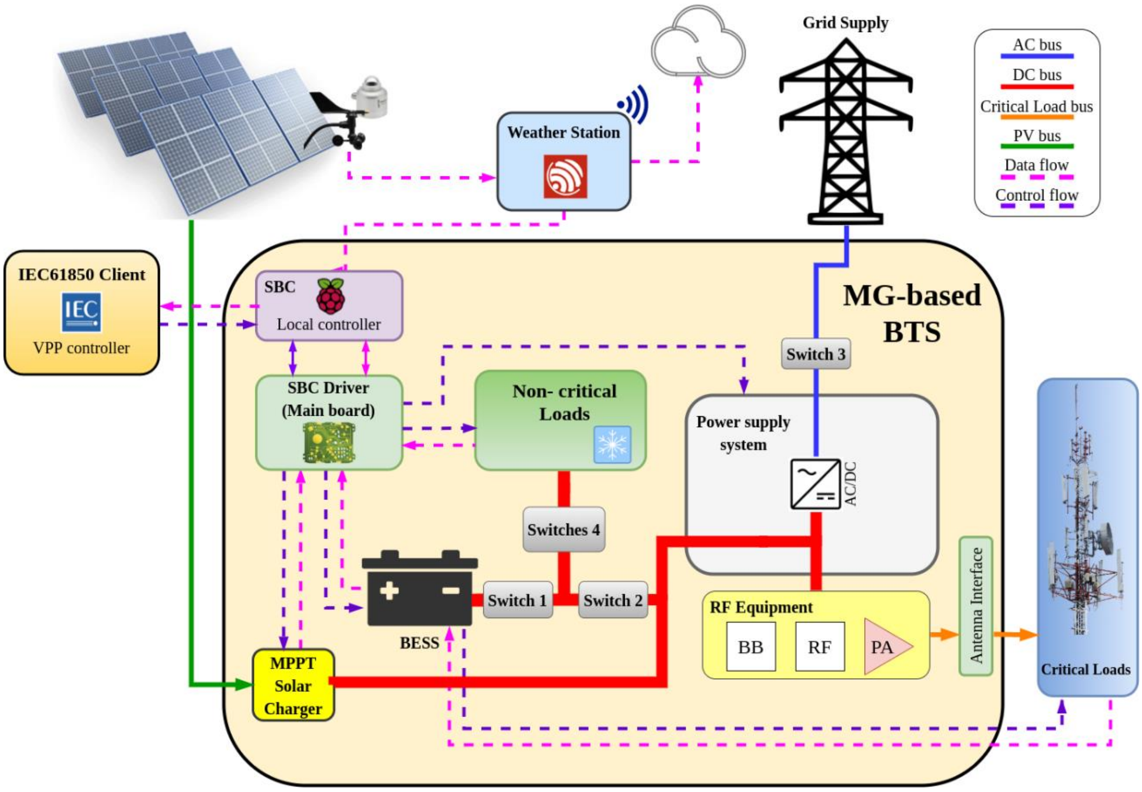

Figure 2. Base Transceiver Stations transformed into DC Microgrids.

The MG-based BTS consists of the aforementioned BTS along with a PV system with Maximum Power Point Tracke (MPPT) control and a DC bus connected to the BTS rectifier. This DC bus acts as the microgrid main bus to which the different elements are connected. The BESS and non-critical loads are directly connected to the DC bus without DC/DC converters. This is the approach adopted by most companies with the aim of maximizing short-term profitability, since a more technologically sophisticated design would increase the costs. In the BTS architecture proposed in this paper, all loads (critical and non-critical) and connections of the different parts of the MG-based BTS become controllable elements through a set of switches (Figure 2). Furthermore, several variables, such as currents and voltages in loads and the BESS are monitored. Thus, different operating modes and energy flows within the BTS can be managed by designing a local controller.

This local controller is implemented on an Single-Board omputer (SBC) Raspberry Pi 4 model B and some electronics associated. The reason for choosing this SBC is three-fold: firstly, a reduction of power consumption is required; secondly, because of its high processing power; finally, the Raspberry Pi platform has been successfully used in similar works [33–35]. The associated electronics consists of a main board and a series of latching relays electrically connected to the main board. In the main board, several sensors and conditioning electronics have been included to collect electrical parameters of the installation, such as BESS and load currents, BESS voltage and some ambient parameters (temperature, humidity, etc.). These parameters are sent to the SBC through I2C protocol. The local controller, which also receives the DC bus voltage and PV modules parameters from the MPPT solar charger controller through Modbus protocol, processes all this information to calculate other variables, such as the State of Charge (SoC) of the BESS, which allows the MG-based BTS to be managed. To implement the control of the MG-based BTS, there are also three latching relays which connect or disconnect the BESS and the non-critical loads to the DC bus, and the rectifier to the grid. Henceforth, these associated electronics will be referred as the SBC driver, since it acts as the bridge between the local controller in the SBC and the hardware of the installation.

Likewise, to provide the basis for the smart sensing strategy, a server based on IEC61850 standard has been implemented. This allows the MG-based BTS to be remotely controlled as a VPP node using an external IEC61850 client. Previously, an IEC61850 plant model of the MG-based BTS is proposed to store data in a standard way.

The MG-based BTS has been designed for the worst-case scenario for a macro BTS with a rated power of 3 kW. The experimental setup has been developed using the same RF equipment and power amplifiers as those installed in 3-kW BTSs. The rated power is equally split among the three controllable loads: two critical loads corresponding to the always-on transceivers and a non-critical load for transceivers that can be switched off, and auxiliary equipment, such as the cooling system, when necessary, and lighting. This power configuration can be easily scaled to meet the requirements of more power-demanding BTSs.

3. MG-Based BTS Operation

3.1. MG-Based BTS Measurements and Control Electronics

In this subsection, the parameters to monitor and the electronics required to accomplish the stated objectives are described. The relationship between the elements that measure the electrical parameters and control the flow of energy in the MG-based BTS is shown in Figure 3. In the following paragraphs, these elements will be explained.

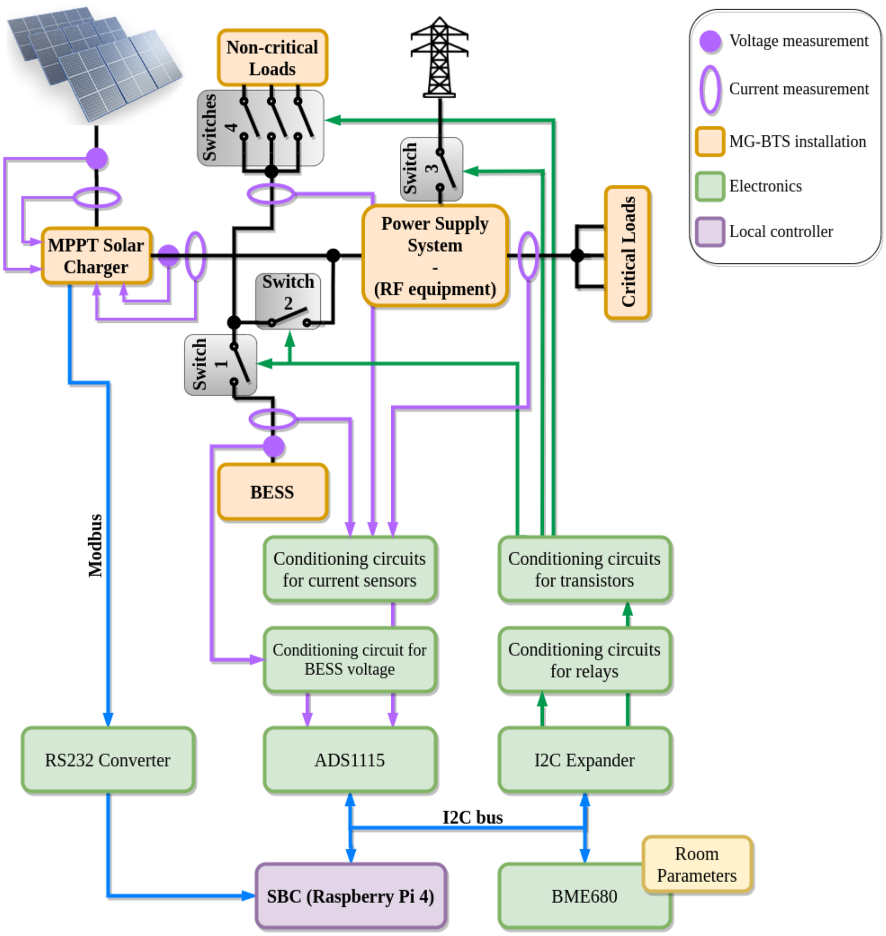

Figure 3. Measurement and control electronics of the MG-based BTS.

Firstly, the DC currents are measured using the ACS758LCB-100B-PFF-T and the ACS758LCB-100U-PFF-T sensors [36] (Figure 4). The range and the sensitivity of these sensors are ±100 A and 40 mV/A, respectively. Regarding the currents, these values are enough for an expected maximum BESS current of ±60 A and a maximum single load current of 20 A. As for the sensitivity, at a full scale, the sensors will output ideally a DC voltage signal between 0 V and 5 V, covering the dynamic range of the ADC used. The conditioning circuits for the current sensors consist of low pass filters with a cutting frequency of 50 Hz. They are used to eliminate possible coupled noise from the grid. Finally, the typical output noise of the sensor, in measured current units, will be 0.33 A, which is acceptable for this application.

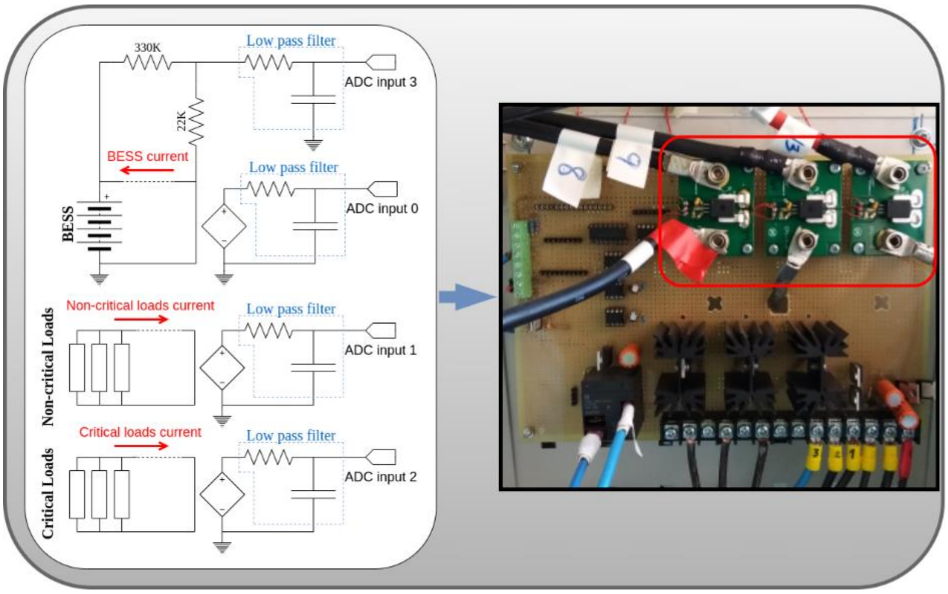

Figure 4. Electronics for the measurement of currents and voltages in BESS, non-critical and critical loads.

The BESS voltage is measured using a voltage divider to scale the voltage to the dynamic range of the ADC (Figure 4). The ADC used to convert the DC currents and voltage measurements is the ADS1115 [37]. This low-cost four-channel 16-bit I2C ADC has an input range from 0 V to 5 V, a maximum sampling frequency of 860 Hz and features low power consumption. Furthermore, to measure the ambient parameters (temperature, humidity and pressure), the I2C BME680 sensor [38] is used due to its low cost and low power consumption.

Once the measurements are obtained, the BESS SoC is estimated. This is an important parameter for the management of the MG-based BTS. In [39], a complete state of the art analysis of different algorithms for lead acid batteries SoC estimation can be found. Among them, the current integration or Coulomb counter method has been used in this paper. This method, along with the manufacturer's specifications of the batteries, are merged to provide an accurate estimation of the SoC, through the floating voltage of the BESS and the dynamic capacity depending on the discharge current rate [40].

The MPPT solar charger provides several parameters related to the PV installation through the Modbus protocol [41]. For the sensing strategy proposed in this paper, the following parameters are required: (i) the output voltage of the MPPT solar charger; (ii) the output current provided by the charger; and (iii) the voltage, current and power of the PV modules. All these parameters are collected in the SBC.

The loads are connected or disconnected through low cost off-the-shelf MOSFET-CSD18536KCS 60 V N-Channel transistors [42]. Their maximum drain-source voltage is 60 V, over the maximum voltage of the DC bus 58 V, which is imposed by the rectifier of the RF equipment at the dedicated output for the BESS [43]. Furthermore, for the connection of the different parts of the installation, EW60-1A3 12VDC 60 A [44] latching relays have been included in the hardware architecture. Figure 5 briefly depicts the conditioning circuits of the transistors and relays of the SBC driver.

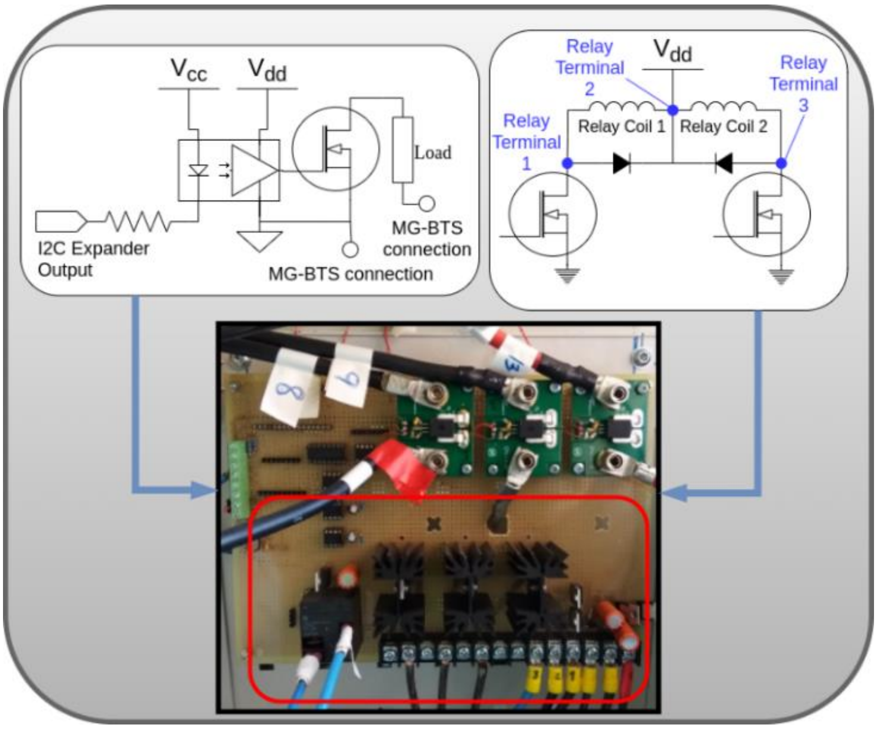

Figure 5. Conditioning circuits of the transistors and relays (SBC driver).

Regarding the power supply for the electronics, there are three isolated sources: (i) the SBC power supply; (ii) the power supply for the main board of the SBC Driver and the transistor-based switches for the critical loads; and (iii) the power source for transistor-based switches for the non-critical loads. This configuration breaks ground loops (leading to less interference in data wires), isolates low power electronics from the higher power parts (cutting off unexpected overloads) and also isolates the SBC and its peripherals, which avoids problems related to different grounding configurations among devices. Regardless of the source, the power is always drawn from the BESS to avoid the eventual loss of power due to a grid failure. To this aim, three different low-cost DC/DC converters, with a rated current of 4 A that meets the current demanded by the SBC driver and the SBC, have been used.

To keep the isolation among the aforementioned parts, drivers based on the FOD3182 optocoupler [45] and the digital isolator MAX14937 [46] for the transistors and I2C communications are included. The SBC controls the optocoupler drivers through two I2C expanders [47].

Finally, electromagnetic noise, due to abrupt changes in DC current flows, must be kept within certain limits. In the early stages of the MG-based BTS development, noise coupling was detected in measurements, generated by the DC currents of the BESS and the loads. Consequently, an analysis of this electromagnetic interference was performed, seeing that a 100-mV noise was coupled into the input signals of the ADC (leading up to a 5 A error in the measurements of DC currents through the loads) and into the BME 680 power supply (leading to a malfunctioning). In the final design of the SBC driver, the components were rearranged to minimize the coupling noise. Figure 6 depicts current measurements taken in the final set up of the SBC driver in the presence of electromagnetic interference. Figure 6 shows a sudden change in the currents through the non-critical loads (Figure 6a) and in the BESS (Figure 6c). Particularly important is the 40 A change in the current through the BESS, which induces electromagnetic interference in the input signal of the ADC, introducing a

0.4 A measurement error in the critical load DC currents. This error is shown in Figure 6b in the shape of a noise peak. Hence, it is important to reduce the negative impact of the noise on the ADC input, achieved in the final design.

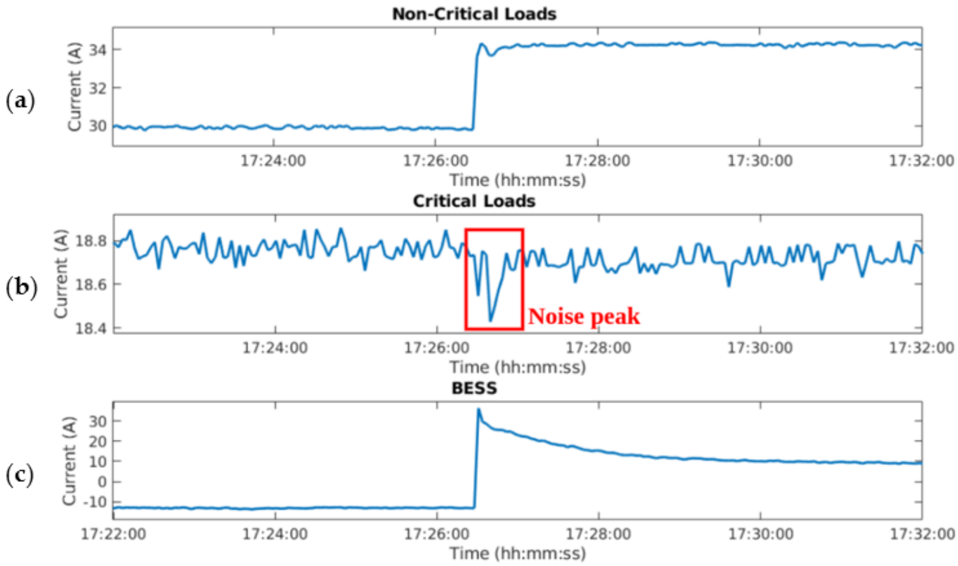

Figure 6. (**a**) sudden change in the currents through the non-critical loads; (**b**) measurement error caused by an approximately 40 A change in the DC current of the BESS; (**c**) sudden change in the currents through BESS.

3.2. Wireless Weather Station

A wireless weather station has been developed and installed close to the PV modules. The architecture of the wireless weather station is shown in Figure 7. The main purpose of this weather station is to collect environmental data, which will be used in the smart sensing strategy focusing on the prediction of PV generation as part of the VPP control strategy.

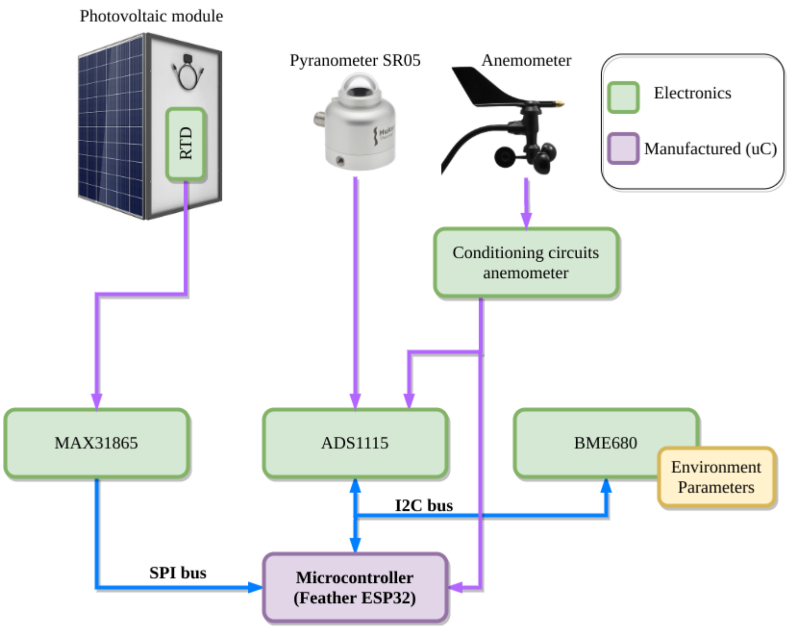

Figure 7. Wireless weather station architecture.

The weather station is made up of two modules: (i) the sensing module, which consists of a set of sensors used to measure environmental parameters related to the PV modules, such as irradiance, wind direction and speed, and PV module temperature; and (ii) the acquisition electronics based on an ESP32 microcontroller and a BME 680 sensor. Regarding the sensing module, a SR05 pyranometer [48] is used to measure the horizontal irradiance [49]. This sensor provides an analog voltage output ranging from 0 V to 2 V for measured irradiance values from 0 to 2000 W/m^2, respectively. The wind direction and speed are obtained by a Davis Instruments anemometer with an operating range from 1 to 322 km/h for wind speed with a resolution of 1 km/h using a sensor based on a reed switch whose output is directly connected to the microcontroller. For wind direction, the operating range goes from 0° to 360° with a resolution of 1 [50]. Finally, the PV module temperature is measured by a PT100.

Figure 8 shows the PT100 fixed to the PV module, the anemometer with PV modules at the background and the acquisition electronics of the weather station.

(**a**) (**b**) (**c**)

Figure 8. (**a**) Wireless weather station: PT100 fixed to the PV module, (**b**) anemometer and (**c**) the acquisition electronics.

As far as the second module is concerned, the ADC ADS1115 converts the voltage information from the pyranometer and the anemometer (wind direction) to digital values which are sent to the microcontroller through the I2C protocol. Additionally, the BME680 sensor measures and processes the ambient temperature, humidity and pressure. This information is also sent to the ESP32 microcontroller via an I2C protocol. A fan has been installed to keep the ambient temperature of the electronics stable and minimize any fluctuation in the temperature measured by the BME680.

The two-core ESP32 microcontroller software architecture is based on the real-time operating system FreeRTOS, which allows to allocate tasks in a particular microcontroller core. One core executes a task which reads the sensor measurements. The other core is responsible for sending the information to the SBC via MQTT (more details will be given in the next subsection), and for sending the information to the IoT cloud of Matlab, named ThingSpeak.

The variables stored in Thingspeak (panel and environment temperature, humidity, irradiance, wind speed and wind direction) are shown in Figure 9.

3.3. Communication System

The communication system is the basis of the smart sensing operation. It is divided into the local communication architecture, which is aimed at creating communication channels between the different SBC processes, the SBC driver and the weather station, and the global communication strategy, which allows the SBC and a global controller to communicate via the IEC61850 standard. A specific extension of this standard is the IEC61850-7-420, which defines the communication and control interfaces of Distributed

Energy Resources (DERs) and proposes logic nodes (LN) to completely describe DERs and control systems associated to them. This extension can be used to model communications in MGs [51].

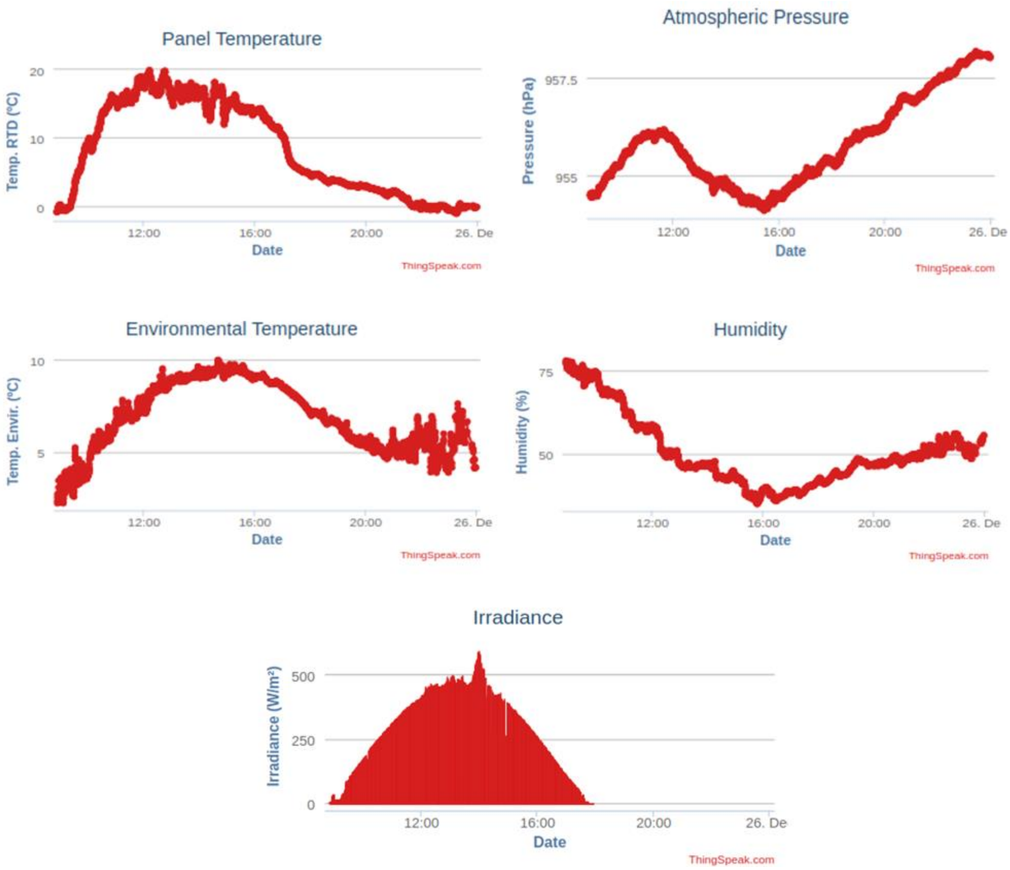

Figure 9. Interface of Thingspeak to visualize stored variables: panel and environment temperature, humidity, irradiance, wind speed and wind direction.

The local communication architecture is based on "The Robot Operating System" (ROS). ROS is an open-source operational system mainly meant to develop robotic systems [52]. In the local communication architecture, the SBC driver sends the measurements via I2C and Modbus to the processes in the SBC. The SBC collects and publishes the measurements as ROS topics to be shared by all the processes. On the other hand, the weather station sends the environmental information via Wi-Fi through MQTT protocol to the SBC. The choice of the MQTT protocol is due to its stability. Finally, the environmental parameters are transformed into ROS topics at the SBC. The block diagram in Figure 10 shows the communication protocols of the smart sensing system.

As for the global communication strategy, the EMS and the IEC61850 Server read the ROS topics related to the measurements and update the IEC61850 plant model parameters of the MG-based BTS. As a result, the IEC61850 clients can directly access the MG-based BTS parameters through a standard communication channel via a TCP/IP protocol. Furthermore, this global communication strategy can receive control instructions from global controllers to change the behavior of the local controller or to directly control the MG-based BTS. The IEC61850 communication standard provides high scalability and interoperability allowing the MG-based BTS to be easily extended with any system or equipment which comply with the standard. From a VPP perspective (based on BTSs), this standard brings an economic benefit, since after the initial investment in the development of an MG-based BTS, the time and capital cost of adding a new MG-based BTS is dramatically reduced.

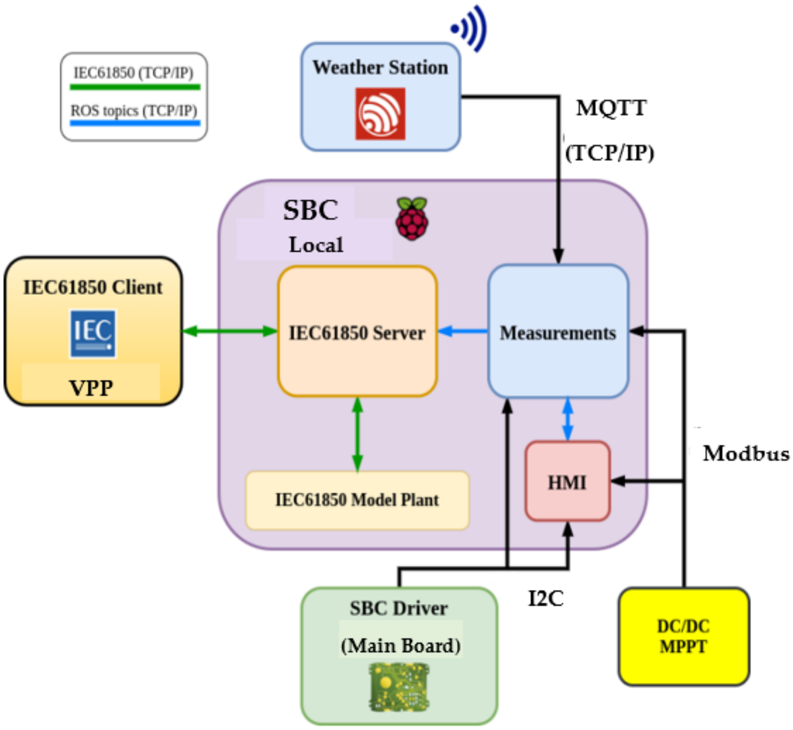

Figure 10. Communication protocols of the smart sensing system.

Figure 11 depicts the plant model of the MG-based BTS, which consists of different logical devices (LD), each one representing one component or device with its own entity. For instance, the logical device labeled as LD RGL represents the MPPT solar charger. This LD contains the ZRGL class, which has been fully specified in this work and cannot be found in the standard. It can be considered that the ZRGL class (Appendix A) expands the IEC61850 (specifically IEC61850-7-420), as the standard does not include any class to describe a DC/DC voltage regulator.

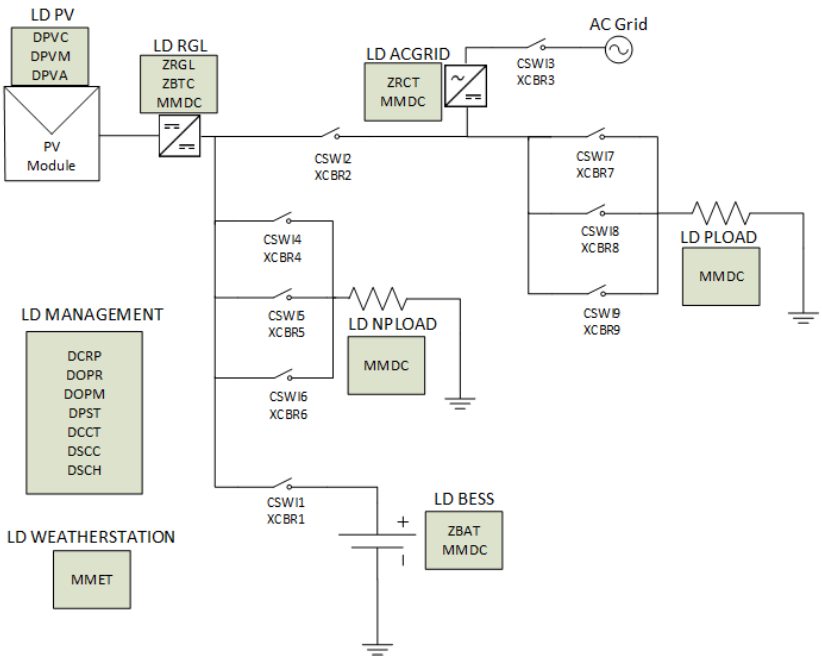

Figure 11. Plant model of the MG-based BTS.

3.4. Processing and Energy Management Systems

3.4.1. Processing System

As introduced in the general overview, the local controller is based on an SBC, which implements the local controller and an HMI (Human-Machine Interface). The local controller consists of a set of processes responsible for coordinating and controlling the different operating modes of the MG-based BTS. Among its main functions are collecting measurements from the SBC driver, the SoC estimation, the control of the energy flows through the EMS, and adding high-level features of the IEC61850 standard. A global controller in the shape of an IEC61850 client could perform control actions and monitoring tasks. Finally, the HMI provides an integrated interface, which displays the data collected from the SBC driver and control variables with the aim of facilitating the manual intervention in the MG-based BTS operation.

The processes comprising the local controller and the HMI can be categorized in three levels: (i) the physical interaction level in which the data from the sensors and the BTS parameters is obtained; (ii) the logic level which is based on the developed IEC61850 Server and implements the EMS, the high-level functionalities, and the modification of the IEC61850 plant model; and (iii) the HMI.

The processes are executed at fixed time intervals depending on the level they are in and the data dependency among them. Those processes in the physical interaction level and those implementing the HMI have the smallest execution interval (2 s) for efficient operation, since the HMI must display the data collected by the processes in the physical interaction level. The execution interval for the processes in the logic level is set to 5 s. It is important to note that the Raspberry PI OS does not feature real-time capabilities. Therefore, the definition of the execution intervals depends on the process execution time.

3.4.2. Energy Management System

The proposed EMS is focused on optimizing the monetary benefits obtained by managing the charging and discharging of the BESS in conjunction with the generation of PV energy and the management of non-critical loads. To implement this strategy, it is necessary to participate in an electricity market with a two-tariff pricing scheme. These markets are common in many countries, as this pricing scheme encourages the consumption of energy in periods where the energy demand is lower. This is the case on the Spanish electricity market [53]. In this type of billing, prices are significantly more expensive for the peak time (PT) tariff in comparison the off-peak (OT) tariff. This type of pricing scheme is particularly recommended for the case under study for two reasons: (i) the PV energy generation takes place mostly during the PT period, which encourages self-consumption at times when the price of energy is higher; and (ii) the energy consumption in the BTS does not tend to vary greatly during the day and the average daily price of energy with two periods is usually lower than the default tariff, which makes the total price of energy consumed by the BTS lower in the case of a two-tariff pricing scheme [54].

In the proposed EMS, it is considered that the installed PV power is less than or equal to the one consumed by the loads installed in the BTS, since the installed equipment does not allow grid feeding. Nevertheless, this strategy can be extended by considering a surplus of PV that can either be injected into the grid or used for battery charging. In this work, it is also assumed that the BESS is working at the proper temperature thanks to the cooling equipment.

Regarding the BESS size, in this work, only the back-up batteries previously installed in the BTS are considered. A further increase in the BESS size could be feasible for new BTS projects, in which more efficient storage technologies, such as Lithium-ion, can be implemented, or if the current battery prices decrease. Since the back-up batteries are used in the EMS strategy, they will not always be fully charged in case of a power outage. To overcome this drawback, three actions are taken:

- It is always guaranteed that the BESS discharge, scheduled by the EMS, does not exceed a minimum level so that the power support is available in the case of an outage.

- The BESS is charged, after a discharge process, at the beginning of the off-peak tariff period when the electricity price is low. This increases the number of hours during the day in which the BESS is fully charged.
- In the event of a power outage, non-critical loads are disconnected to maximize the back-up time provided by the BESS.

It is possible to obtain multiple operating states by using the installed switches (see Table 1). The following states provide an optimal solution for the operation of the BTS while at the same time making an efficient use of the BESS:

- State 0 or Back-up State: this state comes into operation when there is a drop off in the main grid. In this state, which rarely occurs in countries with reliable grids, the consumption of the installation is reduced to only the critical loads, and the BTS is powered by the BESS and the energy available from the PV modules at that time.
- State 1 or Transition State (Peak Tariff) or Battery Charging State (Off-Peak Tariff): this state is used as a transition state in the case of working in the Peak tariff period. The BTS remains in this state for a maximum of 30 s. During the Off-peak tariff period, this state is used to charge the battery.
- State 2 or No Battery State: in this state, the BESS is disconnected, either because it has already been charged to the desired level in the Off-Peak tariff period or because it has been discharged to the defined level in the Peak-tariff period.
- State 3 or Battery Discharging State: the BESS is discharged by powering either part or all of the non-critical loads. Thus, an appropriate discharge current can be selected considering the characteristics indicated by the manufacturer. The remaining loads in the BTS are fed from the grid and the PV system.
- State 4 or Island State: in this state, the BTS works in island mode without drawing power from the grid. This state is used when the production of PV system is sufficient to power the whole BTS, supported by the discharge of the battery within the appropriate discharge range.
- State 5 or Cloud State: this state is used to avoid unnecessary changes of state produced by the drop of PV power occasionally caused by a cloud, while protecting the BESS by keeping it within proper discharge ranges. If the PV power falls abruptly and the BTS is working in State 4 or Island State, the non-critical loads are disconnected, and the average PV production of the last few minutes is continuously checked. If this average PV power generation continues to decrease in the following minutes and the PV production does not recover, the system returns to a grid-supported state.

Once the operational states have been introduced, the proposed finite state machine (FSM) representing the behavior of this EMS is described. Three levels of priority are established, in the state transition:

(1) Very High Priority: In the event of a grid outage, the state is immediately changed from any state to State 0 or Back-up State. When the outage is over, the FSM enters State 1 or Transition State.
(2) High Priority: If there is a change from the off-peak tariff period to the peak tariff period or vice versa, there is a transition from any state to State 1 or Transition State.
(3) Normal Priority: Common EMS operation with grid available and operating within one of the working periods. The transitions in this mode are described in the following table.

To gain an insight into the proposed EMS, a state diagram flowchart describing the operation of the FSM in Normal Priority is shown in Figure 12. To reduce the clutter, the Very High Priority and High Priority transitions are not depicted because they follow basic rules.

Table 1. Finite state machine transitions in normal priority.

State	Switch			Non-Critical Loads	Transition (Normal Priority)	
	1	2	3		Condition	State
0	ON	ON	ON	OFF		
1	ON	ON	ON	ON	$PT\&\&SOC < SOC_{min} \,\|\|\, OT\&\&SOC > SOC_{max}$	2
					$PT\&\&PV < TH_{PV}\&\&\ SOC > SOC_{min}$	3
					$PT\&\&PV \geq\ TH_{PV}\&\&\ SOC > SOC_{min}$	4
2	OFF	ON	ON	ON		
3	ON	OFF	ON	ON	$PV\ > TH^{+}_{PV} \,\|\|\, SOC < SOC_{min}$	1
4	ON	ON	OFF	ON	$SOC < SOC_{min}$	1
					$PV < TH^{-}_{PV}$	5
5	ON	ON	OFF	OFF	$PV > TH_{PV}$	4
					$\overline{PV} > TH_{PV}\|\|SOC < SOC_{min}$	1

PT, Peak tariff period: regarding electricity, the most expensive period of the day. OT, Off-peak period: the most economical period of the day. SOC_{min}, minimum selected state of charge: this value is set according to the manufacturer's guidelines for the BESS to maximize the relation between the depth of discharge of the BESS and the number of life cycles. SOC_{max}, maximum selected state of charge: this value is set according to the manufacture guidelines for the BESS to maximize the relation between the depth of discharge of the BESS and the number of life cycles. TH_{PV}, PV-selected threshold: this value sets the PV power required to switch to island mode ensuring that the BESS complements the PV with adequate discharge currents. TH^{-}_{PV}, PV-selected threshold minus offset: this value is set to establish a hysteresis in state transitions associated with the PV threshold, and thus, prevents high frequency transitions. TH^{+}_{PV}, PV-selected threshold plus offset: this value is set to establish a hysteresis in state transitions associated with the PV threshold, and thus, prevents high frequency transitions. $\overline{PV}$, average PV over the last 15 min: this is used to determine the continuity of the PV drop.

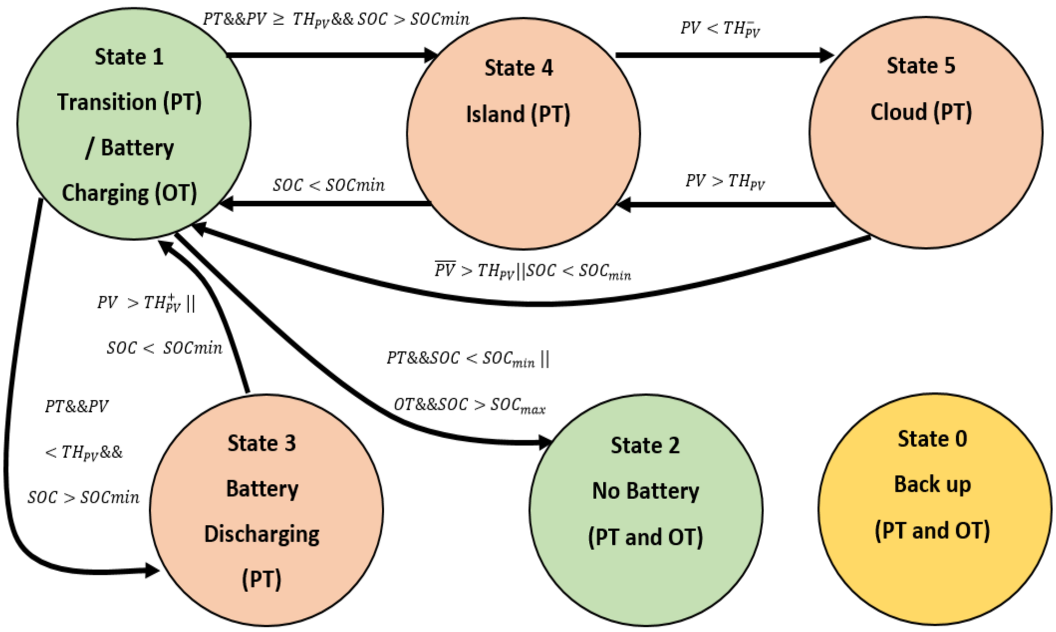

Figure 12. EMS State Diagram showing all states and all Normal Priority transitions.

The green color shows the states that are used in both PT period and OT period, whereas the orange color shows the states that are used only in PT periods. Finally, the yellow color shows the back-up state that is used whenever there is a grid outage.

Once the different transitions have been described, it is possible to analyze the BTS operation modes with the implemented strategy.

When a Very High Priority event occurs, i.e., the grid outage, the system automatically enters the Back-up State. In this state, the non-critical loads are disconnected, and the entire system is powered by the BESS and, if available, by the PV power. This state is maintained until the grid is operative again.

The next condition to be checked is the High Priority event, which occurs twice a day: once when shifting from the PT period to the OT period and the other when changing from the OT period to the PT period. In this case, the EMS operating mode changes completely, as described below in the normal priority operate mode.

The EMS operates in the normal priority mode most of the time, as the very high priority mode only takes place when a grid outage occurs and the high priority mode two moments a day. During the OT period, the BESS is charged to the desired SoC level, which is set by the designer according to the BESS characteristics. Once the BESS is charged, it goes into a standby mode. Conversely, during the PT period, the BESS is discharged in an appropriate manner, considering their characteristics, to guarantee suitable discharge currents and levels to prolong its lifespan and optimize its total capacity [55]. At the same time, PV production is considered in order to choose the moments when it is appropriate to use the island mode of operation in which PV and BESS are responsible for powering the entire BTS by disconnecting it from the grid. It is important to note that all state transitions in this mode of operation are made by applying hysteresis to the PV thresholds of state switching to ensure as few transitions as possible, thus avoiding high-frequency state changes. Following this approach, the Cloud State is implemented to prevent that if a drop in PV production is produced by an occasional cloud, no reconnection to the grid takes place.

This strategy is aimed at optimizing the management of the BESS by ensuring that the discharge currents of the BESS are within the parameters set by the manufacturer and that the depth of discharge chosen maximizes the relationship between the number of BESS cycles and the capacity of the BESS [55].

As an extension of this EMS, in installations where more PV power is installed than the amount of load demanded by the BTS, a new battery state could be considered where the BESS is also charged during the PT period with the surplus of PV. To this end, the BTS PV production forecasts [56] could be used to calculate the periods during the day when this surplus could be produced and, in this way, support the OT charging strategy.

To realize the economic study of the savings obtained with the implemented EMS, it is essential to know the price differential between the PT and OT, as well as the BESS characteristics: battery efficiency, optimal depth of discharge and number of life cycles. For a PV system, it is fundamental to determine the amount of power generated according to the location of the installation as well as the prices in the production hours. In Section 4.4, a study is carried out for the specific case study, also obtaining general conclusions for any market and location.

3.5. Interface System—HMI

The aim of the HMI (Human-Machine Interface) is to display the collected data from the MG-based BTS and the control variables. It also allows the manual operation over the MG-based BTS to be performed. This interface continuously communicates with the local controller to coordinate the operation of BTS and the data monitoring. The HMI has two operational modes: (i) operator mode aimed at manually manipulating all controllable variables of the MG-based BTS and taking measurements without using the local controller processes; and (ii) normal mode, which just acts as a graphical interface to display all the information compiled by the controller and, therefore, by the MG-based BTS. The HMI is implemented using Node-RED, an open-source software which provides a web-based dashboard facilitating its use for any device inside the same network. Figure 13 shows the HMI's appearance.

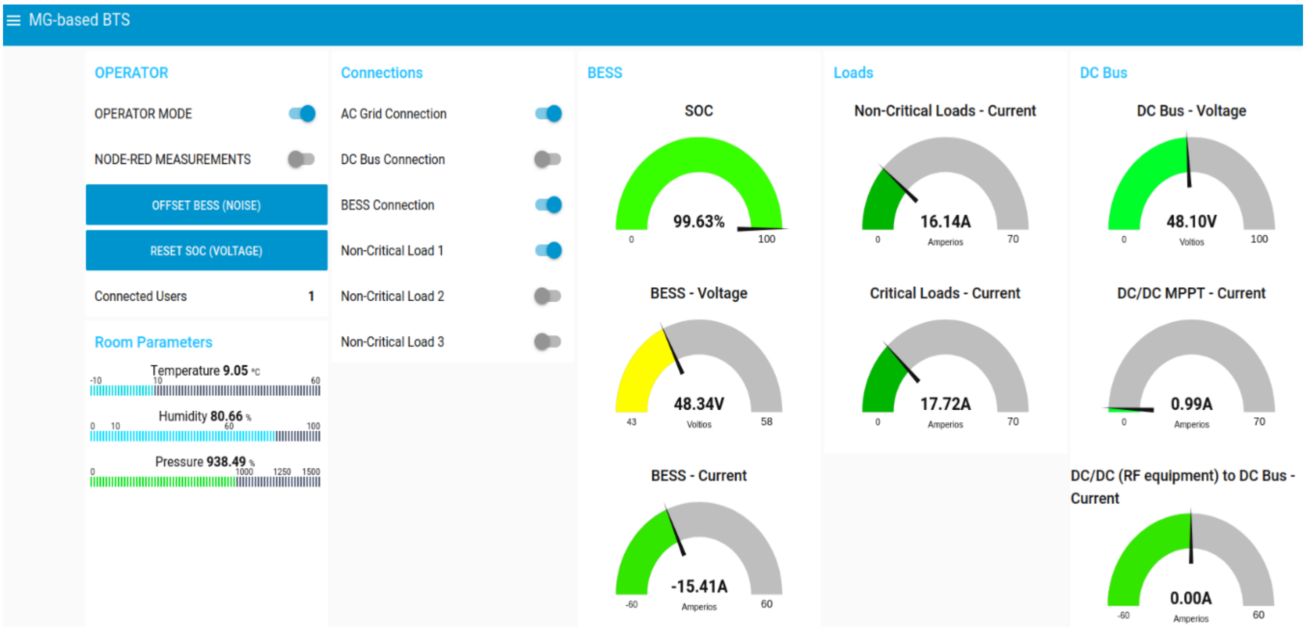

Figure 13. Human-Machine Interface (HMI) designed to monitor and control the MG-based BTS.

4. Results

4.1. Experimental Setup

For the experimental setup, an MG-based BTS has been developed with a rated load power of 3 kW, using the same RF equipment and power amplifiers as those installed in 3-kW BTSs. The sizing of the PV system must consider the space available at the BTS site. Nevertheless, a solar charger controller with MPPT and rated power of 2.7 kW for a BESS of 48 V/190 Ah (composed of four lead batteries) and nine 300-Wp PV panels [57] in a 3 × 3 configuration (3 kW PV power peak) are used in the experimental setup. The charger controller, the BESS and the non-critical loads are connected to the DC bus as seen in the Section 2.2 and shown in Figure 2.

The tests have been performed with a maximum of two critical loads (2 kW) and one non-critical load (1 kW). Figure 14a shows the interior of the main cabinet of the MG-based BTS and Figure 14b shows the PV installation including the meteorological station.

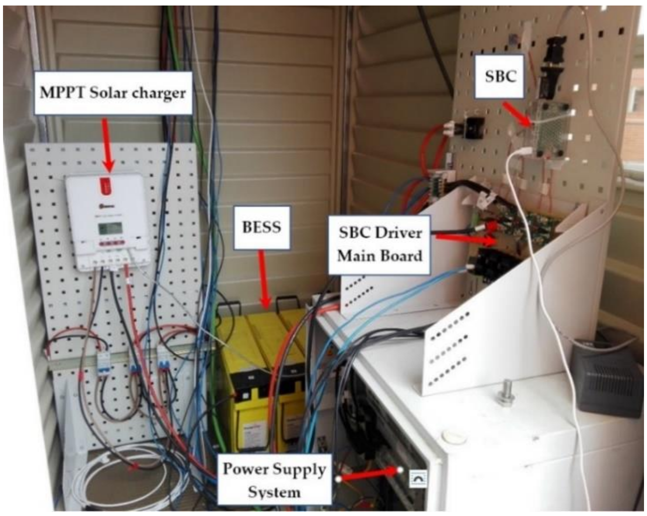

(**a**)

(**b**)

Figure 14. (**a**) Cabinet of the MG-based BTS and (**b**) PV installation including the meteorological station.

4.2. Use Case

In this section, the results obtained with the plant described in the previous section are shown. The first step is to set the design parameters of the EMS according to the characteristics of the plant and the prices of the Spanish energy market in winter time: PT, period from 12:00 to 22:00; OT, period from 22:00 to 12:00; SOC_{min}, 35%; SOC_{max}: 95%; TH_{PV}, 1900 W; TH_{PV}^{-}, 1800 W and TH_{PV}^{+}: 1950 W. The OT and PT values are set by the Spanish energy market. The SOC_{max} and SOC_{min} are based on the battery datasheet provided by the manufacturer, which sets an optimum DoD of 60%. The PV threshold is also defined considering the battery datasheet, stating that the power provided by the BESS is always below 2 kW and most of the time around 1 KW or less. A hysteresis value of 100 W for the PV power is also set to avoid frequent state transitions which could be caused by small oscillations of PV.

Once the design parameters have been described, Figure 15 shows the results obtained in a 24-h test. The test starts at 6.00 a.m., on the 22nd of December 2020, to facilitate the comprehension of the experiment, since it begins in a state in which the BESS is already fully charged to the level defined by the SOC_{max} parameter.

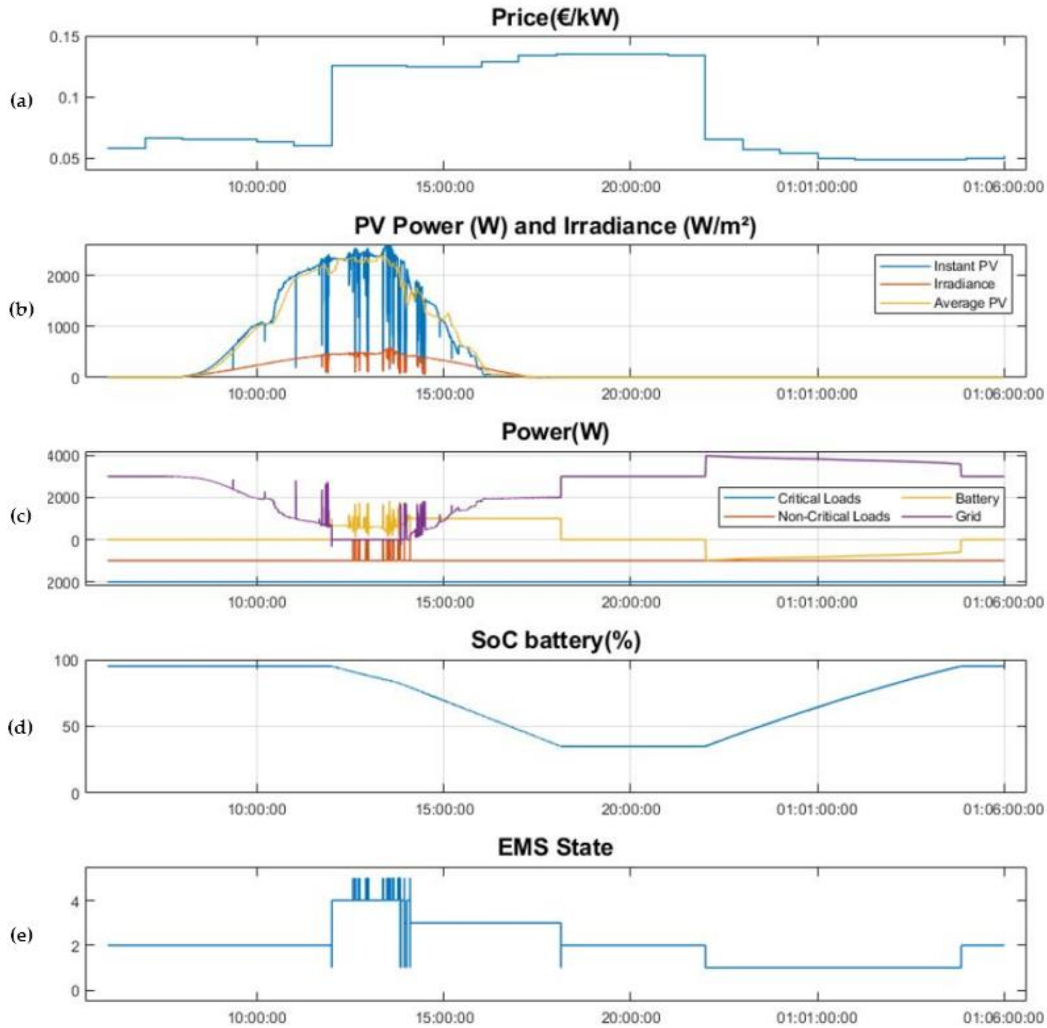

Figure 15. Use Case: (**a**) energy prices in the market for the day under study; (**b**) Instant Power PV production, Average power PV over the last 15 min and irradiance; (**c**) Power consumed by critical and non-critical loads, power consumed and delivered by the BESS and power delivered by the grid; (**d**) SoC level of the battery; (**e**) EMS states.

Figure 15a presents the hourly energy prices. It can be seen that the PT period lasts from 12:00 to 22:00 h and the OT period from 22:00 to 12:00 h. The strategy designed takes advantage of the electricity price difference between the two periods, which is around 0.6 €/kW.

Figure 15b shows the generation of PV power, on a mostly sunny day with different types of clouds to demonstrate the potential of the algorithm. The PV power is shown in blue, the 15-min average PV power in yellow and the irradiance is depicted in red. Analyzing the correlation between the irradiance and PV power measurements, it can be seen that the system is tracking maximum power at all times. The effects produced by the clouds and the potential to use the average PV over the last 15 min is described below, including a zoom of the figure in this working area, Figure 16.

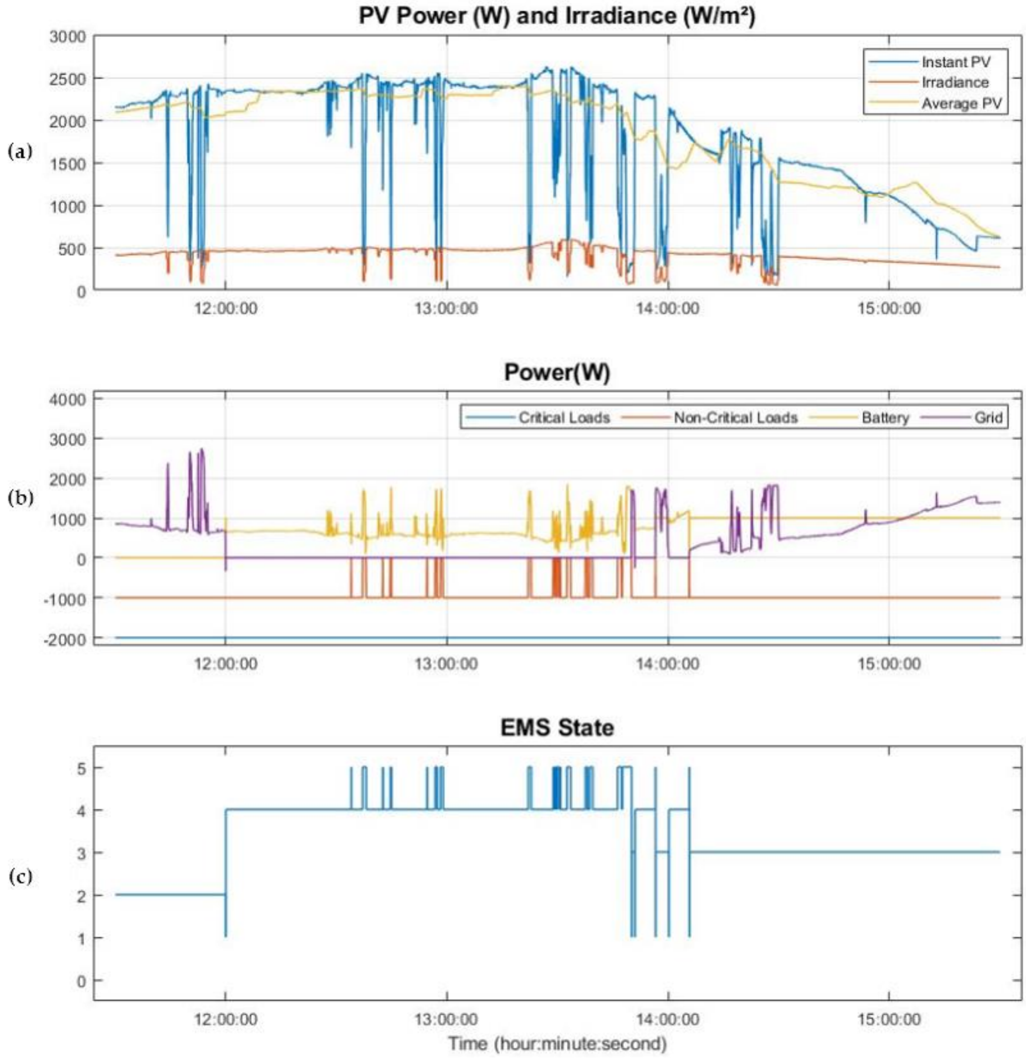

Figure 16. Zoom of use case in the tariff change from OT to PT. (**a**) Instant Power PV production, Average power PV over the last 15 min and irradiance; (**b**) power consumed by critical and non-critical loads, power consumed and delivered by the batteries and power delivered by the grid; (**c**) EMS states.

Figure 15c shows the power consumed by the loads, the power drawn from the grid and the power flow from/to the BESS. Negative values for the power represent consumption and positive values represent supply. The power consumed by the critical loads are shown in blue. These loads have a rated power of 2 kW and are always connected to the power supply. The power consumed by 1-kW non-critical loads are shown in red. These loads are disconnected when the EMS enters the State 5 or Cloud State, which is used to keep the installation in island mode while protecting the maximum discharge current of the BESS. Finally, the power provided to or withdrawn from the BESS is depicted in yellow, and the power drawn from the grid in purple. As expected, the installation consumes all the energy provided by the PV system, with the support of the grid and the BESS when required.

The BESS charging and discharging strategy is represented in Figure 15d, which shows the BESS SoC. It can be appreciated that the BESS is discharged to the desired level, SOC_{min}, 35%, in the first hours of the PT period, from 12:00 to 18:10. During this time, the BESS powers part of the installation, supporting the PV and the grid supply. This minimizes the power drawn from grid in the period of time when the energy is more expensive, reaching the stage where the installation works without drawing power from the grid, which happens when the PV exceeds the 2 kW zone. Then, the BESS is charged from the grid to the desired level SOC_{max}, 95%, in the OT period when the energy is cheaper, from 22:00 to 04:45, to be ready for the next day.

Finally, in Figure 15e, the graph representing the states of the EMS is detailed. In the initial part of the experiment the system is operating in State 2 since the BESS is fully charged. The EMS remains in this state until 12:00 when the tariff changes from OT to PT. Furthermore, the graph shows how the BESS is discharged from 12:00 to 18:10, thereby reducing the power drawn from the grid. In this case, the EMS goes through several states, which are described in detail in Figure 15. From that moment, the system returns to the No Battery State or State 2, as it was discharged to the predefined level. At 22:00 with the change from PT to OT, the BESS is charged taking advantage of the lower prices, State 1 from 22:00 to 04:45.

As mentioned above, in order to describe more precisely the central part of the day in which most states are involved, in Figure 16 a zoomed-in section of Figure 15 with the results between 11:30 and 15:30 h is showed..

At 12:00 h, there is a tariff change from OT to PT, and since the PV power generated is greater than 1900 W, the system is working in island mode using the energy stored in the BESS (states 4 and 5). It can also be seen in the graph that between 12:00 and 13:45, the system, taking advantage of the Cloud State or State 5, is capable of maintaining itself in island mode, while protecting the BESS thanks to the disconnection of the non-critical loads when the occasional crossing of a cloud is detected. This is done by working out the 15-min average PV power in the State 5, which avoids occasional PV fluctuations, which cause high frequency changes from island mode to grid mode, while ensuring that the system does not stay for an excessive amount of time in State 5 in which the BESS may have to assume 2 kW of load and non-critical loads are disconnected.

On the other hand, when the PV power is not sufficient to guarantee island mode all the time, the system relies occasionally on the grid so as not to force the BESS to maintain powers greater than 1 kW for long periods of time caused by longer cloud sky. This parameter results in a trade-off and is modified according to the amount of signal that is integrated to compute the PV average, in this case 15 min. This situation is presented from 13:45 to 14.10, when there is support from the grid.

Finally, from 14:10, the PV power generated is not enough for island mode and the system is maintained in State 3 until the BESS reaches the SoC value of 35%. During this state, the BESS powers the 1 kW non-critical load independently, while the PV system and the grid power the critical loads, 2 kW.

4.3. Smart Sensing Operation

As has been described, all the sensors include communications capabilities, smart processing based on low-cost hardware and cloud computing facilities for predictions and cooperative work among different BTSs.

Going one step further, a set of controllable MG-based BTSs can be aggregated through a centralized management in the shape of a Virtual Power Plant (VPP), which represents a controllable portfolio of BTSs. Consequently, from a VPP perspective, each MG-based BTS is seen as an aggregated controllable VPP node which can interact with other VPP nodes, i.e., other BTSs, with the aim of facilitating the integration of the BTSs into the grid.

Therefore, a hierarchical network structure with a hierarchical control strategy involving both concepts, i.e., microgrid and VPP, can constitute a feasible solution to the challenge of coordinating several BTSs to improve performance.

To allow this cooperative operation mode, the sensors included in the MG-based BTS could provide the EMS system with irradiance predictions in order to better adjust the load and the BESS connection strategy [56]. These predictions are possible because the data provided by the different sensors is stored and processed both locally and in the cloud, thus constituting an intelligent sensor strategy. Additionally, in installations where the PV power installed is greater than the amount of load demanded by the BTS, based on power predictions, a new battery state could be considered where the BESS is also charged during the PT period with the energy surplus from the PV system.

4.4. Economic Study

To carry out an economic study, a general methodology is developed to characterize the savings provided by the proposed strategy in different electricity markets, for different batteries and PV power installed. The most important parameter is related to the market and is based on the average price differential between the PT and OT for battery savings and the energy prices during the hours of PV production.

To make the specific calculation, the Copernicus Atmosphere Monitoring Service [58] is used to calculate the power and the moments when the PV energy is produced at the location of the BTS. By performing these calculations for the last year, savings of 153.93 €/kW of installed PV power are obtained; the total savings are 461.78 € for the 3 kW PV installed. Considering an installation price of 1000 €/kW installed, the PV installation return on investment occurs after 6.5 years.

In the case of the BESS, the calculations are based on the datasheet provided by the manufacturer, which sets a battery discharge efficiency of 85%, an optimum Depth of Discharge (DoD) of 60% and 1500 cycle life for the battery used in the BTS. In addition, it is assumed that these batteries are normally changed every eight years (2920 days); since a cycle is carried out every day, a factor of 0.513 (1500/2920) is applied. This way, the number of days per year that the strategy can be applied can be computed, to match the end of BESS life with the time when the BESS would be replaced. Taking into account that the Spanish average daily price differential between the charging and discharging hours of a whole year is approximately 0.09 €/kWh, the annual savings obtained with a BESS with the described characteristics is 16.8 €/kWh of installed capacity. If the correction factor for the batteries to last eight years is considered, the savings obtained is 8.63 €/kWh for each of the eight years. The total annual savings for the installed battery capacity, 9.12 kWh, is 153.26 €/year without the correction and 79.73 €/year after applying the factor.

Finally, Table 2 provides a summary of the obtained results for a BTS with 2 kW of critical loads and 1 kW of non-critical load with energy supplied by the Spanish energy market, considering a daily price differential between the peak and off-peak hours of approximately 0.09 €/kWh.

Table 2. Results summary.

<table>
<tr><th></th><th>Characteristics</th><th>Annual Savings</th><th>Total Annual Savings</th></tr>
<tr><td>PV</td><td>Peak power = 3 kW</td><td>153.93 €/kW</td><td>461.78 €</td></tr>
<tr><td rowspan="4">BESS</td><td>Capacity = 9.12 kWh</td><td rowspan="4">16.8 €/kWh</td><td rowspan="4">153.26 €</td></tr>
<tr><td>DoD = 60%</td></tr>
<tr><td>Efficiency = 85%</td></tr>
<tr><td>Cycle life = 1500</td></tr>
</table>

5. Conclusions and Future Work

This paper introduces a new BTS HW/SW architecture based on an MG paradigm, which allows an efficient energy management strategy to be implemented through a local EMS. The key function of the EMS is to derive profit from self-consumption of photovoltaic energy generated on the BTS site. With this aim, the EMS implements a load-shedding approach, which depends on the available energy and is applied to non-critical loads. Furthermore, a controllable BESS is used, in which the charging and discharging cycles are optimized to increase its lifespan. Thus, the power supply of conventional BTSs has been entirely transformed into a more sustainable solution by adding new HW/SW elements, which have been described in detail, namely: (i) a monitoring system for determining the value of several electrical and environmental parameters; (ii) electronics to control the energy flow; (iii) a local EMS system; (iv) an IEC 61850 compliant model for the BTS; and (v) a wireless weather station. The proposed HW/SW architecture has been experimentally validated on a pilot BTS plant subjected to different test and weather conditions. Finally, for a two-tariff pricing scheme which is usually offered by energy providers in the Spanish electricity market, annual savings of 16.8 €/kW per installed battery power can be obtained.

A benefit of this system is that it can be applied to both new and existing installations, providing a two-way connection to the electricity grid, photovoltaic generation, smart measurement systems and the required management software, all integrated in a flexible and low-cost HW/SW architecture. More importantly, by adopting an MG-based model, the transformed BTS can also be regarded as an aggregated controllable VPP node. This greatly facilitates the integration of several BTSs into the grid, thereby improving performance by developing a hierarchical network structure based on a hierarchical control scheme in which both the MG and VPP approaches are adopted. Therefore, within the framework of the MG-based BTS architecture proposed in this work, the feasibility of injecting energy into the AC network can be demonstrated by implementing more complex EMS algorithms within larger microgrids for optimal battery management, relying on meteorological information to forecast PV power generation. These are the new challenges which the authors are currently addressing.

Author Contributions: F.J.R. designed and coordinated the overall project; E.S., C.S., J.A.J., M.T., P.M. and M.G. designed and developed the system. C.S. designed the EMS; M.T. developed software of the MG-based BTS; E.S., J.A.J. and M.T. designed and developed the electronics; M.G. defined the 61850 models. Experimental tests were carried out by M.T., C.S. and M.G. Finally, J.A.J., M.T., P.M. and C.S. wrote the manuscript. All authors have read and agreed to the published version of the manuscript.

Funding: This research was funded by the Ministry of Science, Innovation and University of the Government of Spain under the HELIOS Sharing project (RTC-2017-6231-3) and Autonomous Community of Madrid under the project P2018/EMT-4366.

Institutional Review Board Statement: Not applicable.

Informed Consent Statement: Not applicable.

Acknowledgments: The authors thank the company CLYSEMA SA for its collaboration in this research.

Conflicts of Interest: The authors declare no conflict of interest.

Appendix A

Class ZRGL Specified in This Work

<table>
<tr><th colspan="5">ZRGL class</th></tr>
<tr><th>Data object name</th><th>Common data class</th><th>Explanation</th><th>T</th><th>M/O/C</th></tr>
<tr><td>LNName</td><td></td><td>Shall be inherited from logical-node class (see IEC 61850-7-2)</td><td></td><td></td></tr>
<tr><td colspan="5">Data</td></tr>
<tr><td colspan="5">System logical node data</td></tr>
<tr><td></td><td></td><td>LN shall inhert all mandatory data from common logical node class</td><td></td><td>M</td></tr>
<tr><td></td><td></td><td>Data from LLN0 may optionally be used</td><td></td><td>O</td></tr>
<tr><td>WRtg</td><td>ASG</td><td>Maximum power rating</td><td></td><td>M</td></tr>
<tr><td>IsoTyp</td><td>ENG</td><td>Type of isolation:
<table>
<tr><th>Value</th><th>Explanation</th></tr>
<tr><td>0</td><td>Not applicable / Unknown</td></tr>
<tr><td>1</td><td>Power frequency transformer isolated</td></tr>
<tr><td>2</td><td>Hi frequency transformer isolated</td></tr>
<tr><td>3</td><td>Non-isolated, grounded</td></tr>
<tr><td>4</td><td>Non-isolated, isolated DC source</td></tr>
<tr><td>99</td><td>Other</td></tr>
</table></td><td></td><td>M</td></tr>
<tr><td>VRegTyp</td><td>ENG</td><td>Type of voltage regulation:
<table>
<tr><th>Value</th><th>Explanation</th></tr>
<tr><td>0</td><td>Not applicable / Unknown</td></tr>
<tr><td>1</td><td>Regulated output: fixed voltage</td></tr>
<tr><td>2</td><td>Regulated output: variable voltage</td></tr>
<tr><td>3</td><td>Filtered output: load dependant</td></tr>
<tr><td>4</td><td>Unregulated and unfiltered</td></tr>
<tr><td>99</td><td>Other</td></tr>
</table></td><td></td><td>M</td></tr>
<tr><td>ConvTyp</td><td>ENG</td><td>Type of voltage regulation:
<table>
<tr><th>Value</th><th>Explanation</th></tr>
<tr><td>0</td><td>Not applicable / Unknown</td></tr>
<tr><td>1</td><td>Boost</td></tr>
<tr><td>2</td><td>Reducer</td></tr>
<tr><td>3</td><td>Boost-reducer</td></tr>
<tr><td>99</td><td>Other</td></tr>
</table></td><td></td><td>O</td></tr>
<tr><td>CoolTyp</td><td>ENG</td><td>Type of voltage regulation:
<table>
<tr><th>Value</th><th>Explanation</th></tr>
<tr><td>0</td><td>Not applicable / Unknown</td></tr>
<tr><td>1</td><td>Passive air cooling (heatsink)</td></tr>
<tr><td>2</td><td>Forced air cooling (fan + heatsink)</td></tr>
<tr><td>3</td><td>Fluid cooling (water)</td></tr>
<tr><td>4</td><td>Heat pipe</td></tr>
<tr><td>99</td><td>Other</td></tr>
</table></td><td></td><td>O</td></tr>
<tr><td colspan="5">Status information</td></tr>
<tr><td>GridModSt</td><td>ENG</td><td>Current connect mode:
<table>
<tr><th>Value</th><th>Explanation</th></tr>
<tr><td>0</td><td>Not applicable / Unknown</td></tr>
<tr><td>1</td><td>Disconnected</td></tr>
<tr><td>2</td><td>Power not delivered</td></tr>
<tr><td>3</td><td>Power delivered</td></tr>
<tr><td>99</td><td>Other</td></tr>
</table></td><td></td><td>O</td></tr>
</table>

Class ZRGL Specified in This Work (Cont)

<table>
<tr><td>OutFilTyp</td><td>ENG</td><td>Output filter type:
<table>
<tr><th>Value</th><th>Explanation</th></tr>
<tr><td>0</td><td>Not applicable / Unknown</td></tr>
<tr><td>1</td><td>None</td></tr>
<tr><td>2</td><td>Series filter (L)</td></tr>
<tr><td>3</td><td>Parallel filter (LC)</td></tr>
<tr><td>4</td><td>Series-Parallel (LCL)</td></tr>
<tr><td>99</td><td>Other</td></tr>
</table></td><td></td><td>O</td></tr>
<tr><td>Stdby</td><td>SPS</td><td>Regulator stand-by status - True: stand-by active</td><td></td><td>O</td></tr>
<tr><td>CurLev</td><td>SPS</td><td>DC current level available for operation - True: sufficient current</td><td></td><td>O</td></tr>
<tr><td>SwHz</td><td>ASG</td><td>Nominal frecuency of switching</td><td></td><td>O</td></tr>
<tr><td colspan="5">Settings</td></tr>
<tr><td>OutWSet</td><td>ASG</td><td>Output power setpoint</td><td></td><td>O</td></tr>
<tr><td>InALim</td><td>ASG</td><td>Input current limit</td><td></td><td>O</td></tr>
<tr><td>InVLim</td><td>ASG</td><td>Input voltage limit</td><td></td><td>O</td></tr>
<tr><td>OutVSet</td><td>ASG</td><td>Output voltage setpoint</td><td></td><td>O</td></tr>
<tr><td>OutALim</td><td>ASG</td><td>Output current limit</td><td></td><td>O</td></tr>
<tr><td colspan="5">Measured values</td></tr>
<tr><td>HeatSinkTm</td><td>MV</td><td>Heat sink termperature: Alarm if over max</td><td></td><td>O</td></tr>
<tr><td>EnclTmp</td><td>MV</td><td>Enclosure temperature</td><td></td><td>O</td></tr>
<tr><td>AmbAirTem</td><td>MV</td><td>Ambient outside air temperature</td><td></td><td>O</td></tr>
<tr><td>FanSpdVal</td><td>MV</td><td>Measured fan speed: Tach or vane</td><td></td><td>O</td></tr>
</table>

References

1. Vadgama, S.; Hunukumbure, M. Trends in Green Wireless Access Networks. In Proceedings of the 2011 IEEE International Conference on Communications Workshops (ICC), Kyoto, Japan, 5–9 June 2011; pp. 1–5.
2. Sulyman, A.I.; Nassar, A.T.; Samimi, M.K.; MacCartney, G.R.; Rappaport, T.S.; Alsanie, A. Radio propagation path loss models for 5G cellular networks in the 28 GHZ and 38 GHZ millimeter-wave bands. *IEEE Commun. Mag.* **2014**, *52*, 78–86. [CrossRef]
3. Davaslioglu, K.; Gitlin, R.D. 5G green networking: Enabling technologies, potentials, and challenges. In Proceedings of the 2016 IEEE 17th Annual Wireless and Microwave Technology Conference (WAMICON), Clearwater, FL, USA, 11–13 April 2016; pp. 1–6.
4. Wu, J.; Zhang, Y.; Zukerman, M.; Yung, E.K.-N. Energy-Efficient Base-Stations Sleep-Mode Techniques in Green Cellular Networks: A Survey. *IEEE Commun. Surv. Tutorials* **2015**, *17*, 803–826. [CrossRef]
5. Roy, S.N. Energy logic: A road map to reducing energy consumption in telecom munications networks. In Proceedings of the INTELEC 2008—2008 IEEE 30th International Telecommunications Energy Conference, San Diego, CA, USA, 14–18 September 2008; pp. 1–9.
6. Piovesan, N.; Temesgene, D.A.; Miozzo, M.; Dini, P. Joint Load Control and Energy Sharing for Autonomous Operation of 5G Mobile Networks in Micro-Grids. *IEEE Access* **2019**, *7*, 31140–31150. [CrossRef]
7. Standard ETSI ES 203 208. *Environmental Engineering (EE)*; Assessment of Mobile Network Energy Efficiency, Version 1.2.1; ETSI: Sophia Antipolis, France, 2017.
8. Study on Energy Efficiency Aspects of 3GPP Standards; Version 15; Document TR 21.866, 3GPP. Available online: https://portal.3gpp.org/desktopmodules/Specifications/SpecificationDetails.aspx?specificationId=3062 (accessed on 12 October 2020).
9. Auer, G.; Giannini, V.; Desset, C.; Godor, I.; Skillermark, P.; Olsson, M.; Imran, M.A.; Sabella, D.; Gonzalez, M.J.; Blume, O.; et al. How much energy is needed to run a wireless network? *IEEE Wirel. Commun.* **2011**, *18*, 40–49. [CrossRef]
10. ECONET Project. Available online: http://www.econet-project.eu/ (accessed on 20 October 2020).
11. Elmirghani, J.; Klein, T.; Hinton, K.; El-Gorashi, T.; Lawey, A.Q.; Dong, X. GreenTouch GreenMeter core network power consumption models and results. In Proceedings of the 2014 IEEE Online Conference on Green Communications (OnlineGreenComm), Tucson, AZ, USA, 12–14 November 2014; pp. 1–8.
12. Olsson, M.; Cavdar, C.; Frenger, P.; Tombaz, S.; Sabella, D.; Jäntti, R. 5GrEEn: Towards Green 5G mobile networks. In Proceedings of the 2013 IEEE 9th International Conference on Wireless and Mobile Computing, Networking and Communications (WiMob), Lyon, France, 7–9 October 2013; pp. 212–216.
13. OPERA-Net Project. Available online: https://www.celticnext.eu/opera-net-2-paves-the-way-towards-wireless-networks-of-the-future/ (accessed on 16 November 2020).
14. Spagnuolo, A.; Petraglia, A.; Vetromile, C.; Formosi, R.; Lubritto, C. Monitoring and optimization of energy consumption of base transceiver stations. *Energy* **2015**, *81*, 286–293. [CrossRef]
15. Fehske, A.; Fettweis, G.; Malmodin, J.; Biczok, G. The global footprint of mobile communications: The ecological and economic perspective. *IEEE Commun. Mag.* **2011**, *49*, 55–62. [CrossRef]
16. Chamola, V.; Krishnamachari, B. Solar powered cellular base stations: Current scenario, issues and proposed solutions. *IEEE Commun. Mag.* **2016**, *54*, 108–114. [CrossRef]
17. Amutha, W.M.; Veeraraghavalu, R. Techno-economic evaluation of various hybrid power systems for rural telecom. *Renew. Sustain. Energy Rev.* **2015**, *43*, 553–561. [CrossRef]
18. Oviroh, P.O.; Jen, T.-C. The Energy Cost Analysis of Hybrid Systems and Diesel Generators in Powering Selected Base Transceiver Station Locations in Nigeria. *Energies* **2018**, *11*, 687. [CrossRef]
19. Jahid, A.; Hossain, S.; Monju, K.H.; Rahman, F.; Hossain, F. Techno-Economic and Energy Efficiency Analysis of Optimal Power Supply Solutions for Green Cellular Base Stations. *IEEE Access* **2020**, *8*, 43776–43795. [CrossRef]
20. Aris, A.M.; Shabani, B. Sustainable Power Supply Solutions for Off-Grid Base Stations. *Energies* **2015**, *8*, 10904–10941. [CrossRef]
21. Alsharif, M.H. Optimization design and economic analysis of energy management strategy based on photovoltaic/energy storage for heterogeneous cellular networks using the HOMER model. *Sol. Energy* **2017**, *147*, 133–150. [CrossRef]
22. Chamola, V.; Sikdar, B. Power Outage Estimation and Resource Dimensioning for Solar Powered Cellular Base Stations. *IEEE Trans. Commun.* **2016**, *64*, 5278–5289. [CrossRef]
23. Edler, T.; Lundberg, S. Energy efficiency enhancements in radio access networks. *Ericsson Rev.* **2004**, *81*, 22–51.
24. Yan, M.; Chan, C.A.; Gygax, A.F.; Yan, J.; Campbell, L.; Nirmalathas, A.; Leckie, C. Modeling the Total Energy Consumption of Mobile Network Services and Applications. *Energies* **2019**, *12*, 184. [CrossRef]
25. Lubritto, C.; Petraglia, A.; Vetromile, C.; D'Onofrio, A.; Caterina, F.; Logorelli, M.; Marsico, G.; Curcuruto, S.; Miglio, L.; Cenci, F. Simulation analysis and test study of BTS power saving techniques. In Proceedings of the INTELEC 2009—31st International Telecommunications Energy Conference, Incheon, Korea, 18–22 October 2009; pp. 1–4.
26. Louhi, J.T. Energy efficiency of modern cellular base stations. In Proceedings of the INTELEC 07—29th International Telecommunications Energy Conference, Rome, Italy, 30 September–4 October 2007; pp. 475–476.
27. Madeti, S.R.; Singh, S. Monitoring system for photovoltaic plants: A review. *Renew. Sustain. Energy Rev.* **2017**, *67*, 1180–1207. [CrossRef]
28. Moreno-Garcia, I.; Palacios-Garcia, E.J.; Pallares-Lopez, V.; Santiago, I.; Gonzalez-Redondo, M.; Varo-Martinez, M.; Calvo, R.J.R. Real-Time Monitoring System for a Utility-Scale Photovoltaic Power Plant. *Sensors* **2016**, *16*, 770. [CrossRef] [PubMed]

29. Yahyaoui, I.; Segatto, M.E. A practical technique for on-line monitoring of a photovoltaic plant connected to a single-phase grid. *Energy Convers. Manag.* **2017**, *132*, 198–206. [CrossRef]
30. Nosratabadi, S.M.; Hooshmand, R.-A.; Gholipour, E. A comprehensive review on microgrid and virtual power plant concepts employed for distributed energy resources scheduling in power systems. *Renew. Sustain. Energy Rev.* **2017**, *67*, 341–363. [CrossRef]
31. Nakamura, M.; Takeno, K.; Hisamitsu, R.; Shoyama, M. Bi-directional Multiport Converter for Utilizing Green Base Stations as Virtual Power Plant. In Proceedings of the 2019 8th International Conference on Renewable Energy Research and Applications (ICRERA), Brasov, Romania, 3–6 November 2019; pp. 137–141.
32. DeBaillie, B.; Desset, C.; Louagie, F. A Flexible and Future-Proof Power Model for Cellular Base Stations. In Proceedings of the 2015 IEEE 81st Vehicular Technology Conference (VTC Spring), Glasgow, UK, 11–14 May 2015; pp. 1–7.
33. Rwegasira, D.; Mvungi, N.; Tenhunen, H. Agent Based System for Improved Control and Monitoring of a Solar Driven DC Microgrid. In Proceedings of the 2018 IEEE PES/IAS PowerAfrica, Cape Town, South Africa, 28–29 June 2018; pp. 890–894. [CrossRef]
34. Iovine, A.; Rigaut, T.; Damm, G.; De Santis, E.; Di Benedetto, M.D. Power management for a DC MicroGrid integrating renewables and storages. *Control. Eng. Pr.* **2019**, *85*, 59–79. [CrossRef]
35. Rwegarsira, D.; Ben Dhaou, I.; Kondoro, A.W.; Kelati, A.; Mvungi, N.; Tenhunen, H. A Hardware-in-Loop Simulation of DC Microgrid using Multi-Agent Systems. In Proceedings of the 2018 22nd Conference of Open Innovations Association (FRUCT), Jyvaskyla, Finland, 15–18 May 2018; pp. 232–237.
36. Allegro Microsystems. Available online: https://www.allegromicro.com/en/products/sense/current-sensor-ics/fifty-to-two-hundred-amp-integrated-conductor-sensor-ics/acs770 (accessed on 14 December 2020).
37. ADS1115—Texas Instruments. Available online: http://www.ti.com/lit/ds/symlink/ads1114.pdf (accessed on 20 December 2020).
38. BME680—Bosch. Available online: https://cdn-shop.adafruit.com/product-files/3660/BME680.pdf (accessed on 20 December 2020).
39. Zabaleta, J.; San Martín, I.; Pascual, J. *Cálculo del Estado de Carga en Baterías de Plomo-Ácido: Diseño y Validación Experimental*; Universidad Pública de Navarra: Pamplona, Spain, 2016.
40. Power Safe. Available online: https://datasheet.octopart.com/12V125F-EnerSys-datasheet-62067597.pdf (accessed on 15 December 2020).
41. Bauer—MPPT Solar Charger 12/24/36/48v 60a. Available online: https://autosolar.es/pdf/manual-regulador-mppt-bauer-12-24-36-48-60a.pdf (accessed on 15 December 2020).
42. Texas Instruments—sd18536kcs60 v n-Channelnexfet Powermosfet. Available online: https://www.ti.com/lit/ds/slps532a/slps532a.pdf?ts=1598804855050&ref_url=https%253A%252F%252Fwww.google.com%252F (accessed on 11 October 2020).
43. Huawei-Apm30h. Available online: https://fccid.io/ANATEL/03515-13-03257/Manual/51E9F29C-1DCE-4A94-8275-1A7E1FF7533A (accessed on 11 October 2020).
44. Te Connectivity—Power Latching Relay Ew60. Available online: https://www.te.com/commerce/DocumentDelivery/DDEController?Action=showdoc&DocId=Data+Sheet%7FEW60_Datasheet_07042016%7F0416%7Fpdf%7FEnglish7FENG_DS_EW60_Datasheet_07042016_0416.pdf%7F2071366-1 (accessed on 14 December 2020).
45. Mouser. Available online: https://www.mouser.com/datasheet/2/149/FOD3182-93828.pdf (accessed on 12 October 2020).
46. Maxim. Available online: https://datasheets.maximintegrated.com/en/ds/MAX14937.pdf (accessed on 11 October 2020).
47. NXP. Available online: https://www.nxp.com/docs/en/data-sheet/PCF8574_PCF8574A.pdf (accessed on 17 October 2020).
48. Hukseflux Thermal Sensors. Available online: https://www.hukseflux.com/products/solar-radiation-sensors/pyranometers/sr05-d1a3-pyranometer (accessed on 23 November 2020).
49. Hukseflux User Manual sr05 Series. Available online: https://www.hukseflux.com/uploads/product-documents/SR05_digital_series_manual_v1814.pdf (accessed on 23 November 2020).
50. Davis Instruments. Available online: https://www.davisinstruments.com/product_documents/weather/spec_sheets/7911_SS.pdf (accessed on 23 October 2020).
51. Hussain, S.M.S.; Tak, A.; Ustun, T.S.; Ali, I. Communication Modeling of Solar Home System and Smart Meter in Smart Grids. *IEEE Access* **2018**, *6*, 16985–16996. [CrossRef]
52. Quigley, M.; Conley, K.; Gerkey, B.; Faust, J.; Foote, T.; Leibs, J.; Wheeler, R.; Ng, A. Ros: An open-source robot operating system. In Proceedings of the ICRA Workshop on Open Source Software, Kobe, Japan, 12–17 May 2009.
53. REE. Available online: https://www.esios.ree.es/es (accessed on 14 December 2020).
54. Gayo, M.; Santos, C.; Sanchez, F.J.R.; Martin, P.; Jimenez, J.A.; Tradacete, M. Addressing Challenges in Prosumer-Based Microgrids with Blockchain and an IEC 61850-Based Communication Scheme. *IEEE Access* **2020**, *8*, 201806–201822. [CrossRef]
55. Alramlawi, M.; Li, P. Design Optimization of a Residential PV-Battery Microgrid with a Detailed Battery Lifetime Estimation Model. *IEEE Trans. Ind. Appl.* **2020**, *56*, 2020–2030. [CrossRef]
56. Moreno, G.; Martin, P.; Santos, C.; Rodríguez, F.J.; Santiso, E. A Day-Ahead Irradiance Forecasting Strategy for the Integra-tion of Photovoltaic Systems in Virtual Power Plants. *IEEE Access* **2020**, *8*, 204226–204240. [CrossRef]
57. TP672P-320/325/330W. Polycrystalline Solar Module. 72-Cell Series. Available online: https://www.talesunenergy.com/fileadmin/user_upload/pdf/data_sheets/TP672P.pdf (accessed on 11 October 2020).
58. Copernicus Atmosphere Monitoring Service. Available online: https://atmosphere.copernicus.eu/solar-energy (accessed on 15 December 2020).

sensors

Article

Intra-Day Solar Power Forecasting Strategy for Managing Virtual Power Plants

Guillermo Moreno [1], Carlos Santos [2], Pedro Martín [1], Francisco Javier Rodríguez [1,*], Rafael Peña [2] and Branislav Vuksanovic [3]

[1] Department of Electronics, University of Alcalá, Alcalá de Henares, 28805 Madrid, Spain; guillermo.morenob@uah.es (G.M.); pedro.martin@uah.es (P.M.)
[2] Department of Signal Theory and Communications, University of Alcalá, Alcalá de Henares, 28805 Madrid, Spain; carlos.santos@uah.es (C.S.); rafael.pena@uah.es (R.P.)
[3] School of Engineering, University of Portsmouth, Winston Churchill Ave., Portsmouth PO1 3HJ, UK; branislav.vuksanovic@port.ac.uk
* Correspondence: franciscoj.rodriguez@uah.es; Tel.: +34-91-885-6561

Abstract: Solar energy penetration has been on the rise worldwide during the past decade, attracting a growing interest in solar power forecasting over short time horizons. The increasing integration of these resources without accurate power forecasts hinders the grid operation and discourages the use of this renewable resource. To overcome this problem, Virtual Power Plants (VPPs) provide a solution to centralize the management of several installations to minimize the forecasting error. This paper introduces a method to efficiently produce intra-day accurate Photovoltaic (PV) power forecasts at different locations, by using free and available information. Prediction intervals, which are based on the Mean Absolute Error (MAE), account for the forecast uncertainty which provides additional information about the VPP node power generation. The performance of the forecasting strategy has been verified against the power generated by a real PV installation, and a set of ground-based meteorological stations in geographical proximity have been used to emulate a VPP. The forecasting approach is based on a Long Short-Term Memory (LSTM) network and shows similar errors to those obtained with other deep learning methods published in the literature, offering a MAE performance of 44.19 W/m^2 under different lead times and launch times. By applying this technique to 8 VPP nodes, the global error is reduced by 12.37% in terms of the MAE, showing huge potential in this environment.

Keywords: power forecasting; long short-term memory recurrent neural network (LSTM-RNN); virtual power plant (VPP)

Citation: Moreno, G.; Santos, C.; Martín, P.; Rodríguez, F.J.; Peña, R.; Vuksanovic, B. Intra-Day Solar Power Forecasting Strategy for Managing Virtual Power Plants. *Sensors* **2021**, *21*, 5648. https://doi.org/10.3390/s21165648

Academic Editor: Hossam A. Gabbar

Received: 29 July 2021
Accepted: 20 August 2021
Published: 22 August 2021

1. Introduction

Around the world, the full deployment of solar energy is being facilitated by several factors including, but not limited to, the reduced price of solar panels; environmental, political and social concerns; and solar energy undercutting utility prices, inter alia. According to [1] global installed capacity will double every two years; however, significant factors have been identified which impede the speed at which solar dominance can be achieved: (i) lack of investments in efficiency, (ii) insufficient government incentives, and (iii) regulatory constraints. Small-scale Photovoltaic (PV) installations such those in the residential sector benefit from self-consumption by shifting a load from hours when electricity prices are high to hours when the PV energy is being generated, thereby achieving electricity bill savings. Going one step further, the aggregation and coordination of several PV installations in the shape of a Virtual Power Plant (VPP) with the accurate forecasting of global production facilitates its integration into the network [2]. Consequently, the increasing PV penetration can lead to the increasing aggregation of PV systems into VPPs. However, these new business models are difficult to implement due to the previously mentioned regulatory constraints.

Power forecasting along with load demand and energy prices, for different time horizons and resolutions, are factored into the equation. For VPPs, spatial horizons should also be considered. Forecasting methods can be classified according to different factors, such as: the forecasted parameter (irradiance or power), the time horizon and resolution, the lead time, the model approach, and the nature of the forecasting statistic. Regarding the forecasted parameter, two different alternatives exist: direct [3] and indirect [4]. The direct method predicts the solar power through historical datasets of PV power generation and weather conditions. Indirect forecasting differs from the direct method in that it firstly predicts the solar irradiance and then, the solar power is calculated by using a performance model of the PV plant. As far as the time horizon is concerned, four categories can be found [5,6]: nowcasting (from 1 min to several minutes) which is used for real-time optimization in Energy Management Systems (EMSs); short-term forecast (from 1 h to several hours) used for intra-day market participation and for day-ahead operation optimization; medium term forecast (from 1 month to 1 year); and long-term forecast (up to several years). Time resolutions may range from 1 minute for real-time market operations, and 15-minute periods for load-shifting strategies and for optimizing Battery Energy Storage Systems (BESSs), to 1 hour for longer time horizons used by consumption monitoring, and a 1-week resolution for 1-year time horizons which can be used to identify consumption trends [7]. The lead time can be defined as the time difference between the instant when the forecast is launched and the occurrence of the forecasted value, considering the forecast horizon as the maximum forecast lead time. Forecast errors increase with forecast lead time due to the atmospheric motion. As for the model, the optimal method for solar irradiance prediction depends on the forecast lead time [8]. In this regard, four approaches have been widely used [9]: (a) time-series-based statistical models whose aim is to identify patterns between historical datasets and the output parameters; (b) machine learning (ML) models mainly based on artificial neural networks (ANNs), which use historical datasets to learn the dependency between the past and the future; (c) physical strategies which utilize Numerical Weather Prediction (NWP) and PV models for solar power forecasting; and (d) hybrid models which explore different algorithm combinations with the aim of improving forecast accuracy and reducing the computational burden of online forecasting applications [5]. The objective of all the models is to improve forecasting accuracy by minimizing some quality metrics, usually the sum of squared errors. The existence of different models raises the question of whether one method is better than the others. This is particularly true for statistical and ML models. Some studies conclude that statistical models outperform ML models [10] while others state the opposite [11,12]. However, this interpretation may appear to be fairly simplistic without taking into account the dataset size [13], the variable being forecast [14], the time horizon [15], or the computational load [16]. Although historically, the forecasts have been dominated by statistical methods, over the last decade there has been a significant shift toward ML strategies [17]. This comparative study is beyond the scope of the paper.

Regardless of the method used, the existence of forecasting errors poses a major challenge in optimizing the PV plant operation. While minor forecasting errors may not adversely affect the PV plant operation, larger errors can produce negative effects in the optimization models. Uncertainties hinder the performance in terms of accurately assessing the variables during the PV plant scheduling and operation. Forecast uncertainty quantification is, therefore, crucial. For this reason, considering the prediction intervals, which account for the uncertainty, provides additional accurate information about the expected values in terms of the range of plausible values and the probability assigned to each of them [17,18]. Another solution to the problem involves the aggregation of several PV sites for a unique forecasting strategy, since the error is significantly reduced as the number of installations increases. To prove this, in [19] the authors present an approach to forecast the PV power from irradiance prediction maps, obtaining the power forecast of 200 sites located in Germany. Results show that the error is reduced from a Root Mean Square Error (RMSE) of 0.11 kW/kW_{peak} for single sites, to 0.06 kW/kW_{peak}

for an area of 220 km × 220 km with multiple sites. The distance among sites is also an important factor which influences accuracy, since the error is significantly reduced when the distance between facilities increases. This strategy provides a powerful solution in the context of VPPs, since multiple systems or nodes are controlled, managing Distributed Generation (DG) units, Energy Storage Systems (ESSs), flexible loads and Information and Communication Technologies (ICTs) [20]. Regarding the types of DG units, PV systems can be considered as the easiest and most cost-effective Renewable Energy Sources (RESs) to exploit, mainly for households, where it is possible to turn PV installations into flexible VPP nodes [21].

Finally, as stated above, for indirect forecasting approaches, performance models of PV systems are required to obtain the prediction of solar power generation. To this end, a strategy that works under arbitrary conditions of irradiance and temperature must be adopted. Methods that exhibit these key characteristics are the Osterwald's method [22], which stands out by its simplicity, or similar studies from the literature that improve the performance of the Osterwald's method by adjusting the results under low irradiance levels [23,24]. When the operating point of the PV panels is known, alternative methods, such as those reported in [25,26], can improve accuracy, while other research uses parametrization models to simplify the process [27]. Sometimes, the irradiance of the site is measured on a horizontal plane, obtaining the Global Horizontal Irradiance (GHI). However, the panels are on a different plane. This is typical in satellite measurements but can also be the case in installations with multiple Maximum Power Point Trackers (MPPT) or PV panels with axis trackers. To solve this problem, a conversion process is needed, using: (i) different expressions to tackle the problem step-by-step by separating the global components into direct irradiance, diffuse irradiance, and albedo, modifying the angle of these components to obtain the global irradiance on the plane of the panel, estimating its losses to obtain the effective irradiance, or (ii) an approach that simplifies the process [28]. In this regard, it becomes crucial to reduce the complexity and the computational burden placed on the forecasting algorithms. With this in mind, this work makes use of the Osterwald's method to calculate the PV power, since low irradiance values ($G < 125\ \mathrm{W/m^2}$) are barely existent in the dataset and a generalization of the algorithm for VPP environments leads to better results. Satellite data are also required in this work since they offer information on the GHI, which is converted into irradiance on the tilted plane by following the steps stated above.

The forecasting strategy developed in this paper, uses long short-term memory recurrent neural networks (LSTM-RNNs) and is based on an indirect approach in which the irradiance is forecasted first and the output power is calculated by using the PV model. LSTM-RNNs have been used in several works, achieving satisfactory results on account of their recurrent architecture, which includes memory units [16]. These allow the ANN to identify temporal patterns from the historical data of the forecast variable, thereby reducing the forecast error in comparison to other alternatives. The authors in [29] propose a PV power forecasting strategy based on LSTM-RNN which is compared with other methods without memory units, showing their limitations in terms of not being able to model the dynamics of the PV output power data. In [30] a LSTM-RNN with only exogenous inputs, e.g., dry bulb and wet bulb temperatures, and relative humidity, is used to forecast the day-ahead solar irradiance.

The main contributions of this paper are summarized as follows: (i) the PV forecasting method is applied to a VPP environment to reduce the forecasting error, which is modelled as a function of two well-defined parameters called lead time and launch time; (ii) prediction intervals are used to model the forecast uncertainty as a function of not only the lead time and the launch time, but also the Cloud Cover Factor (CCF), which allows the type of day to be identified; (iii) the input data for the forecasting strategy are derived from free-of-charge open-access data sources, offering a viable and cost-effective solution; and (iv) a trade-off between accuracy and computational burden facilitates the application of multiple PV power forecasts at different locations, within the context of a VPP.

The remainder of this paper is organized as follows: Section 2 introduces the framework for the intra-day power forecasting strategy; the experimental results are presented in Section 3; and finally, some conclusions are drawn in Section 4.

2. Intra-Day Power Forecasting Framework

The proposed intra-day power forecasting strategy is depicted in Figure 1. It consists of four main blocks, namely: (i) input data; (ii) data preprocessing; (iii) model design and forecasting; and (iv) VPP coordination. The input data, which come from different sources, are fed to the preprocessing stage. The preprocessing step prepares the data as required by the training and forecasting models. Finally, the output of the forecasting algorithms is used as the input of the EMS of the VPP. In the following, the different parts are explained in detail.

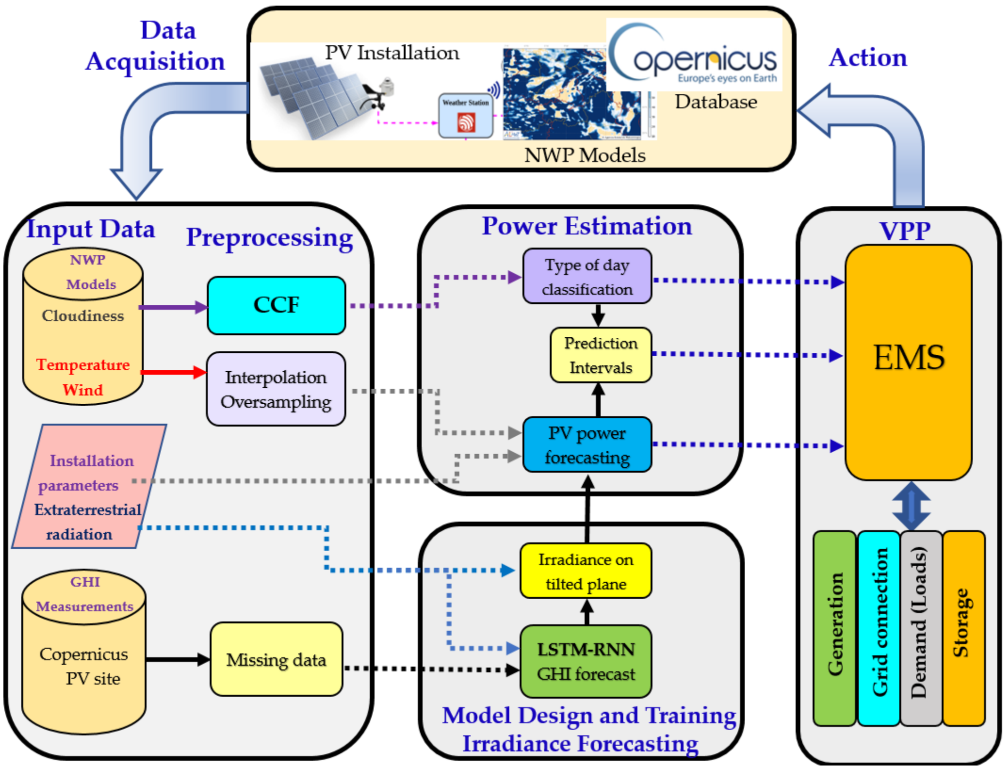

Figure 1. Forecasting framework.

2.1. Input Data

The input data consist of three specific categories according to the source and type of the information provided. The first category includes cloudiness and temperature, which are obtained from forecast maps, at different spatial and temporal scales, generated and regularly published by the Spanish agency of meteorology AEMET, via NWP [31]. The cloudiness dataset is used to define the Cloud Cover Factor (CCF), which indicates to what extent a cloud area on the NWP-based cloudiness maps creates shadows on the PV installation. This parameter is used to define the type of day: sunny, cloudy, and overcast. This allows the dataset to be split in different groups to create prediction intervals. Temperature data, on the other hand, are used to estimate the cell temperature of the solar panel at the prediction instant [32]. NWP-based weather maps are of great interest since some useful weather variables might not be available in solar installations. The deviation in the estimation of the cell temperature is then assessed by using the data obtained from the experimental setup, which is located at the Polytechnic School of the University of Alcala (Spain) and consists of a 2.97 kW_p PV facility with a meteorological station that gathers information of GHI, temperature and cell temperature [33]. The dataset, obtained from the PV facility, is taken during the period between 1 June 2020 and 31 May 2021, with a resolution of 15 min. In the second category, the Global Horizontal Irradiance (GHI) measurements are obtained from two sources: (i) a pyrometer, which is installed in the experimental setup and 30-second GHI measurements are taken and stored on the cloud (ThingSpeak) [34]; and (ii) the Copernicus Atmosphere Monitoring Service (CAMS), which provides a free historical dataset of the incoming surface solar irradiance that can be used for any purpose. The data accuracy is ensured by a regular quality control against information from in situ systems such as ground stations [35]. At the PV facility, the Mean Absolute Error (MAE) committed for the temperature with respect to NWP maps is 2.12 ºC. Likewise, the MAE obtained between the CAMS and the PV station is 46.97 W/m^2, for the whole year of measurements. This database is used to provide the forecasting models with a large GHI dataset for training purposes. Finally, the third category comprises non-stochastic data, such as sun position, used for the CCF calculation to determine the type of day; the extraterrestrial radiation for generating the forecasts and working out the irradiance on the tilted plane of the PV modules; and the installation parameters which are required for the PV power forecasting, as is explained in the following sections.

2.2. Data Preprocessing

The information obtained from the NWP-based weather forecasts must be transformed into numerical values. The forecasting time resolution is set to 15 min, mainly to follow the European Electricity Market Directive to be implemented in the coming years, which sets 15-minute energy matching periods. However, the AEMET only generates the weather maps hourly. This poses the inherent problem of merging time series with different time steps. For instance, for the PV power forecasting, the cell temperature (based on the ambient temperature) and the irradiance on the tilted plane are required. Since the latter has a time resolution of 15 min, so too should the time resolution of the time series for the cell temperature. To this end, quadratic interpolation is performed to create an oversampling of the NWP time series. Changes in the ambient temperature are usually smooth and it is assumed that the measurements shown in the NWP maps are defined with their intermediate values, since the Darboux property [36] is accomplished.

To prove the accuracy of this approach, Figure 2 depicts the ambient temperature obtained from the AEMET forecasts with respect to the values measured by a weather station located in the PV installation. The remarkable accuracy of the weather forecast for the temperature is noticeable.

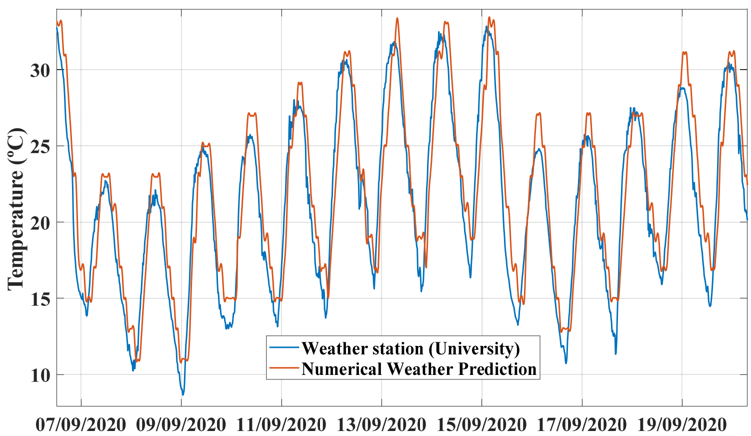

Figure 2. A comparison between the ambient temperature measured at the station and the temperature obtained from the AEMET website.

The CCF, on the other hand, is obtained by processing cloudiness information from weather maps. This parameter, which allows the type of the day to be defined, is used to identify those periods of time for which the presence of clouds can alter the PV power generation over a region through blocking the sun's radiation. The CCF is obtained using a similar method as the work presented in [37], which provides a detailed description of how to calculate this parameter; mainly by detecting cloud-contaminated pixels in the weather maps that interfere between the sun and the installation.

Finally, missing data can negatively affect the accuracy of the forecasts. To fill the missing gaps in the temperature and GHI datasets obtained from the weather station in the PV installation, GHI satellite data and the data from the NWP-based weather forecasts are used. Figure 3 shows an example of the reconstruction of missing data for the temperature and irradiance time series.

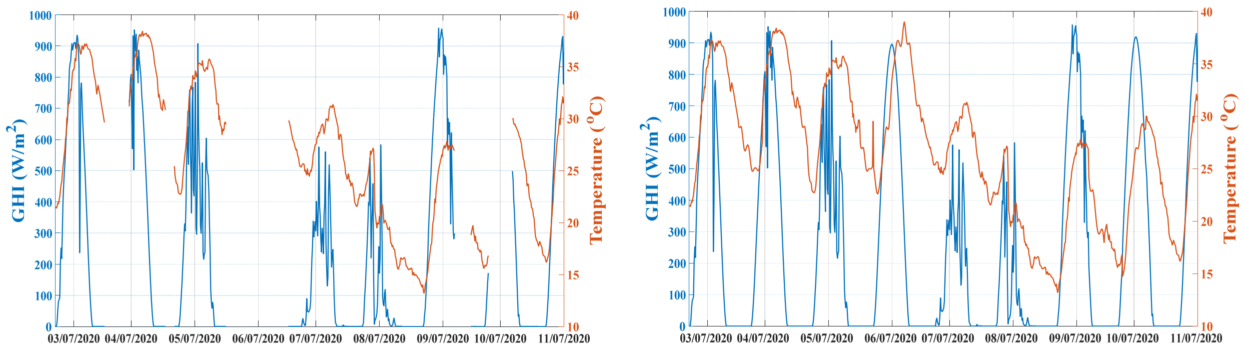

(**a**) (**b**)

Figure 3. (**a**) Missing data of the GHI and the temperature on the site; (**b**) Time series reconstruction of the GHI and the temperature on the site.

2.3. Model Design and Irradiance Forecasting

The third part in the forecasting framework deals with the LSTM-RNN-based model design and the forecasting itself, which aims to: (a) predict the mean PV power for a particular day with a 15-minute time step at the experimental PV facility, and (b) compute prediction intervals intended to show the likely uncertainty in the forecasting outcome [17]. This information constitutes an important input for the EMS in the VPP.

Figure 4 shows the flowchart of the model design and forecasting. The forecasting process starts with the LSTM-RNN model definition based on an iterative approach. Five years of GHI measurements from the Copernicus databases are utilized in the training process. The LSTM-RNN architecture depends on the characteristics of the input and output data and the cross-validation process. When creating the LSTM-RNN, 10% of the training set is used as the cross-validation set, optimizing the number of hidden layer units, mini-batch sizes, regularization factors, learn rate, and epochs (Table 1). Once these parameters are defined, the algorithm is extended to be used for future forecasts. The error in the training process is minimized by computing the RMSE, taking into account not only the proper convergence of the system but the computational time of the process. Squared errors lead the convergence in the LSTM-RNN as they are responsible for avoiding atypical errors, which have remarkable importance in energy management tasks. The architecture is composed of two input layers, one recurrent hidden layer (based on fifty memory blocks), and one output layer (Table 1). The memory block includes one or more self-connected memory cells along with four multiplicative gates (input, output, update, and forget gates). These gates provide the mechanism whereby the information can be stored and accessed over long periods of time, thereby avoiding the vanishing and exploding gradient problem posed by the conventional RNNs [38], e.g., the activation of the cell can be delayed, providing that the input gate remains closed to new inputs which can later become available by opening the output gate. The purpose of LSTM-RNN is, therefore, to model long-range dependencies. When training with sequential data, Gated Recurrent Unit (GRU), LSTM-RNN, and the Convolutional Neural Network (CNN)-LSTM are predominant in the literature [16]. As for CNN-LSTM models, they ensure higher accuracies for predictions based on more features which significantly compromise the computational time. It is worth noting that only two variables are used in this work. In [39] the authors show that these deep learning techniques ensure a higher accuracy than conventional ANNs or Support Vector Machines (SVMs) in GHI short-term forecasting. Consequently, LSTM-RNNs are used in this paper for the forecasting process. LSTM-RNNs achieve remarkable forecast accuracy with different prediction intervals, on account of their ability to memorize long historical data and determine the optimal time lags for the time series. These features are fundamental in the context of irradiance forecasting since there is no previous knowledge of the relationship between forecasts and the length of the historical dataset.

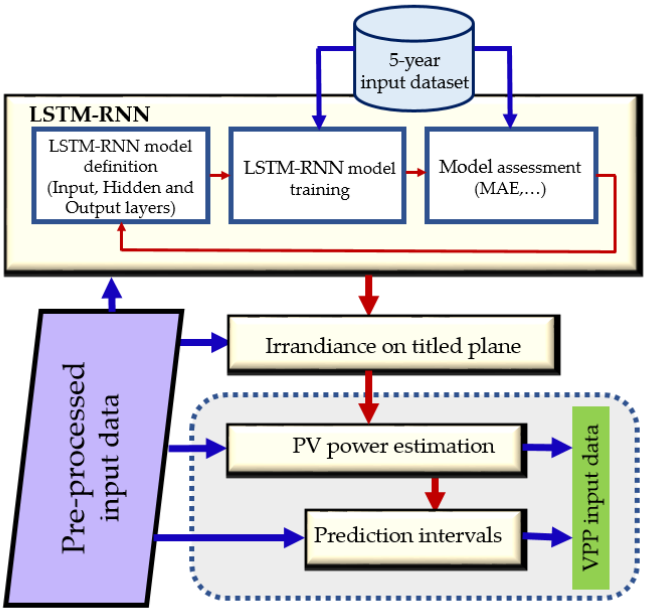

Figure 4. Flowchart for the LSTM-RNN-based forecasting model design.

Table 1. Parameters selected in the LSTM-RNN.

Number of Features	2 (GHI, Extra-Terrestrial Radiation)
Hidden layer units	50
Number of responses	1
Mini-batch size	256
Regularization factor	5×10^{-4}
Optimizer	Adam ($\beta_1 = 0.9$, $\beta_2 = 0.999$, $\epsilon = 1 \times 10^{-8}$)
Initial learn rate	0.01
Learn rate schedule	Piecewise (periodically)
Learning drop	0.5 every 20 epochs
Epochs	70
Limited gradient	1

Once the LSTM-RNN model has been devised, the GHI prediction is made, followed by the estimation of the effective irradiance on the tilted plane of the PV module. Firstly, the calculation of the effective irradiance uses information from the two components of irradiance in the horizontal plane (direct and diffuse, since the albedo is zero in this case), calculated as a function of the clarity index (k_{th}), to obtain the diffuse fraction (k_{dh}) [40]. Once this information is obtained, the conversion into the tilted plane is estimated with the diffuse irradiance [41] and the albedo:

$$albedo = r_o \, ghm_0 \, (1 - cos\beta)/2 \tag{1}$$

where r_o is the albedo coefficient, considering that a value of 0.2, ghm_0 is the GHI and β is the tilted angle of the panels. Finally, the effective irradiance is determined by considering angular [42] and spectral [43] losses for p-Si modules and a typical moderate dust degree of $DT = 0.97$ for the installation.

The Osterwald's model [22] is used to convert the effective irradiance into PV power:

$$P_{DC} = SF\, \eta_{DC}\, P_{peak} \frac{G_{panel}}{G_{STC}} \left(1 + \delta P_m (T_{cell} - T_{cell,STC})\right), \quad (2)$$

where P_{DC} is the PV power forecasted; SF represents the shading losses due to the surroundings of the installation, determined in Section 3.2 for this particular case; $\eta_{DC} = 0.927$ includes wiring losses, module tolerances and mismatch losses; $P_{peak} = 2.97$ kW is the peak power of the installation; G_{panel} is the effective irradiance of the panels previously calculated; $G_{STC} = 1$ kW/m^2 is the irradiance under Standard Test Conditions; (STC), $\delta P_m = -0.4\%/^{\circ}$C is the temperature coefficient of the PV panels of the installation; T_{cell} is the cell temperature; and $T_{cell,STC}$ is the cell temperature under STC.

The cell temperature can be determined with the following expression, assuming the wind speed is negligible, since it can be considered as a nonsignificant effect complex to model because the wind does not affect each panel in the facility equally:

$$T_{cell} = \frac{T_{cell,NOCT} - T_{amb,NOCT}}{G_{NOCT}} G_{panel} + T_{amb}, \quad (3)$$

where $T_{cell,NOCT} = 45$ °C is the cell temperature under Normal Operating Cell Temperature (NOCT) conditions; $T_{amb,NOCT} = 20$ °C is the ambient temperature under NOCT conditions; $G_{NOCT} = 0.8$ kW/m^2 is the irradiance under NOCT conditions; and T_{amb} is the ambient temperature, obtained from NWP forecasts.

Then, with the historical dataset of PV power forecasts, it is possible to compute prediction intervals for new forecasts. A prediction interval is an interval estimate for an unknown future value [17] which can be regarded as a random variable at the time when the prediction is made. In this paper, statistical prediction intervals are employed based on the work presented in [44], considering a Laplacian distribution model for the error as a function of the lead time, the launch time, and the type of day. Figure 5 shows the intervals for a specified day with 90% confidence, providing additional, valuable information from the forecast. PV power generation strongly depends on the weather conditions, the latter varying according to the season. This greatly hinders the ability of the forecasting algorithms to deliver accurate predictions, causing some degree of uncertainty which should be evaluated. Prediction intervals constitute the tool that can be used to express the degree of uncertainty of point forecasts which add a given confidence level. Additional details about the definition of the intervals, such as group selection and accuracy, are further explained in Section 3.3.

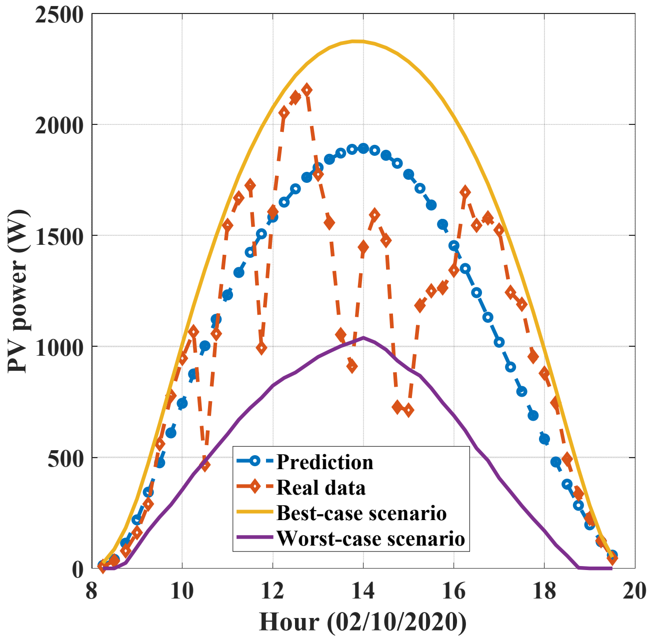

Figure 5. Prediction intervals with respect to the PV power.

3. Results

This section presents the results obtained by the proposed intra-day forecasting strategy for VPP, which is divided into different steps: (a) GHI forecasting for a real VPP node and for an emulated VPP; (b) PV power estimation from the GHI forecasting output; (c) the quantitative assessment of prediction intervals; and (d) VPP scheduling. Firstly, the results are validated for a real PV installation, which plays the role of a VPP node. The PV installation is located in the Polytechnic School, at the University of Alcala (Madrid). Secondly, the strategy is developed for an emulated VPP, by using several ground-based meteorological stations uniformly spread over the Community of Madrid [33]. In order to evaluate the effectiveness of the model, a performance comparison in terms of accuracy/error, with respect to other methods proposed in literature, is also performed.

3.1. LSTM-RNN-Based GHI Forecasting for a Real VPP Node

The LSTM-RNN-based GHI forecasting for the real VPP node is performed by using measurements of irradiance taken in the PV facility located at the Polytechnic School of the University of Alcala (Spain). The initial training dataset is based on a 5-year period of irradiance values obtained from the CAMS dataset, since RNNs require a large amount of data for the learning process and GHI measurements are scarce in new installations. However, the test dataset is based on real measurements taken during the period from 1 June 2020 to 31 May 2021. Therefore, a whole year of real GHI values under different seasonal weather conditions are used to assess the accuracy of the forecasting approach. With a resolution of 15 min, the forecasting process starts at sunrise and ends at sunset. Furthermore, a new prediction is launched every 15 min and the dataset of irradiance is then updated, which ensures the accuracy of the results obtained. The network is trained with new measurements every day, during the night, to yield the best results. The GHI forecasts are given as a function of both the launch time and the lead time, parameters which are further defined, with the aim of computing the prediction intervals.

As far as the error assessment is concerned, this work relies on two types of metrics: (i) scale-dependent metrics such as the MAE and the Root Mean Square Error (RMSE); (ii) percentage-error metrics, such as the relative Mean Absolute Error (rMAE); and (iii) the relative Root Mean Square Error (rRMSE). Absolute values provide information about the average forecasting whereas the quadratic values are more sensitive to outliers, the combined analysis of the two allows for a thorough study of the results.. Error percentage values, on the other hand, provide an intuitive understanding of the error committed, which allows for a fair comparison to be conducted since the dependence on the magnitude is removed. However, when these values are near zero, scale-dependent metrics constitute the preferred option. The error metrics are summarized in Table 2, where Y_t is the measured data at time t, $\hat{Y}_t$ is the forecast value at time t, and T is the length of the time series used to assess the accuracy of the algorithm.

Table 2. Metrics used to evaluate the model performance.

Metrics	Scaled (W/m^2)	Percentage (%)
Absolute	$MAE = \frac{1}{T}\sum_{t=1}^{T}\left\lvert Y_t - \hat{Y}_t\right\rvert$	$rMAE = \frac{\frac{1}{T}\sum_{t=1}^{T}\left\lvert Y_t - \hat{Y}_t\right\rvert}{\frac{1}{T}\sum_{t=1}^{T} Y_t} \times 100$
Quadratic	$RMSE = \sqrt{\frac{1}{T}\sum_{t=1}^{T}\left(Y_t - \hat{Y}_t\right)^2}$	$rRMSE = \frac{\sqrt{\frac{1}{T}\sum_{t=1}^{T}\left(Y_t - \hat{Y}_t\right)^2}}{\frac{1}{T}\sum_{t=1}^{T} Y_t} \times 100$

The value of Y_t denotes GHI at a specific hour of the day, t, and $\hat{Y}_{t',t}$ is the prediction of Y_t at t'. The initial time, t_0, is fixed for each day and corresponds to the sunrise. To assess the error, two parameters are defined: lead time and launch time. Lead time corresponds to $(t' - t)$ and is the difference between the time instant of the prediction and the moment when the prediction is launched. Launch time, on the other hand, is denoted by $(t' - t_0)$ and is the difference between the current time and sunrise. Launch and lead time for the predictions of a particular day are better explained in Figure 6. When the launch time is fixed and the lead time is used as a parameter, a vector of predictions is obtained. However, when both parameters are set to a value, a single point forecast is obtained (red diamond in Figure 6).

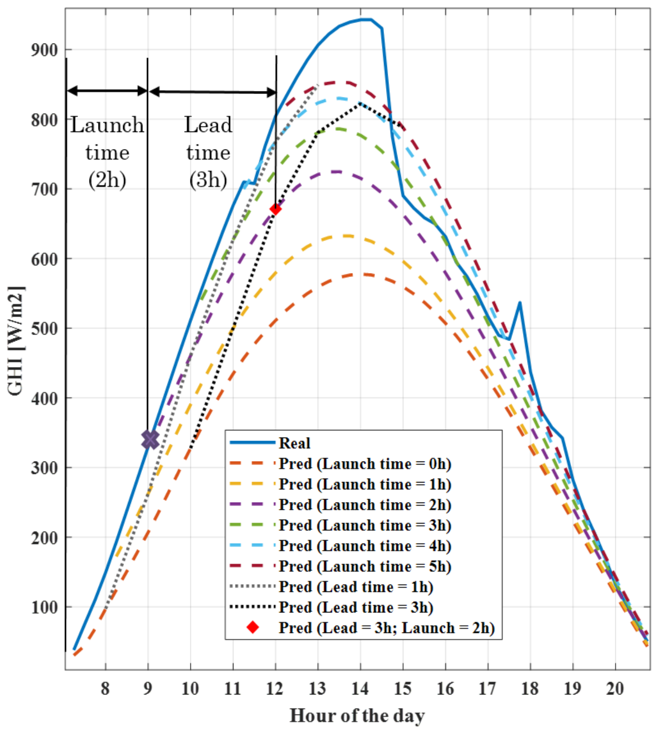

Figure 6. Real measurements of a selected day and its predictions. Dashed lines are the predictions for different launch times and dotted lines correspond to different lead times. Both parameters can be specified for a single day, obtaining the point forecast plotted with a red diamond.

The 3D plot in Figure 7 depicts the errors as a function of the lead time and the launch time which leads to the following conclusions. Firstly, for the scaled error, a high error rate is observed for short launch times under medium lead times. It is expected that the scaled error is large under the previous conditions since the radiation is high. However, as the launch time increases, this error significantly decreases. Secondly, it was clear that the lower the radiation, the smaller the scaled error; however, for percentage errors, the opposite is the case; when the launch time is small (less than 1 h), the percentage error is high, irrespective of the lead time. These plots give some insight into the prediction behavior and become particularly useful in enhancing confidence in the prediction with respect to other forecasting techniques. In this particular case, the intra-daily prediction is used when the mean error is smaller than the day-ahead prediction [37]. Finally, prediction intervals are derived from the MAE, assuming a particular distribution and splitting the predictions into groups as a function of the lead time, the launch time and the type of day, being very useful when a high degree of accuracy is required for the prediction.

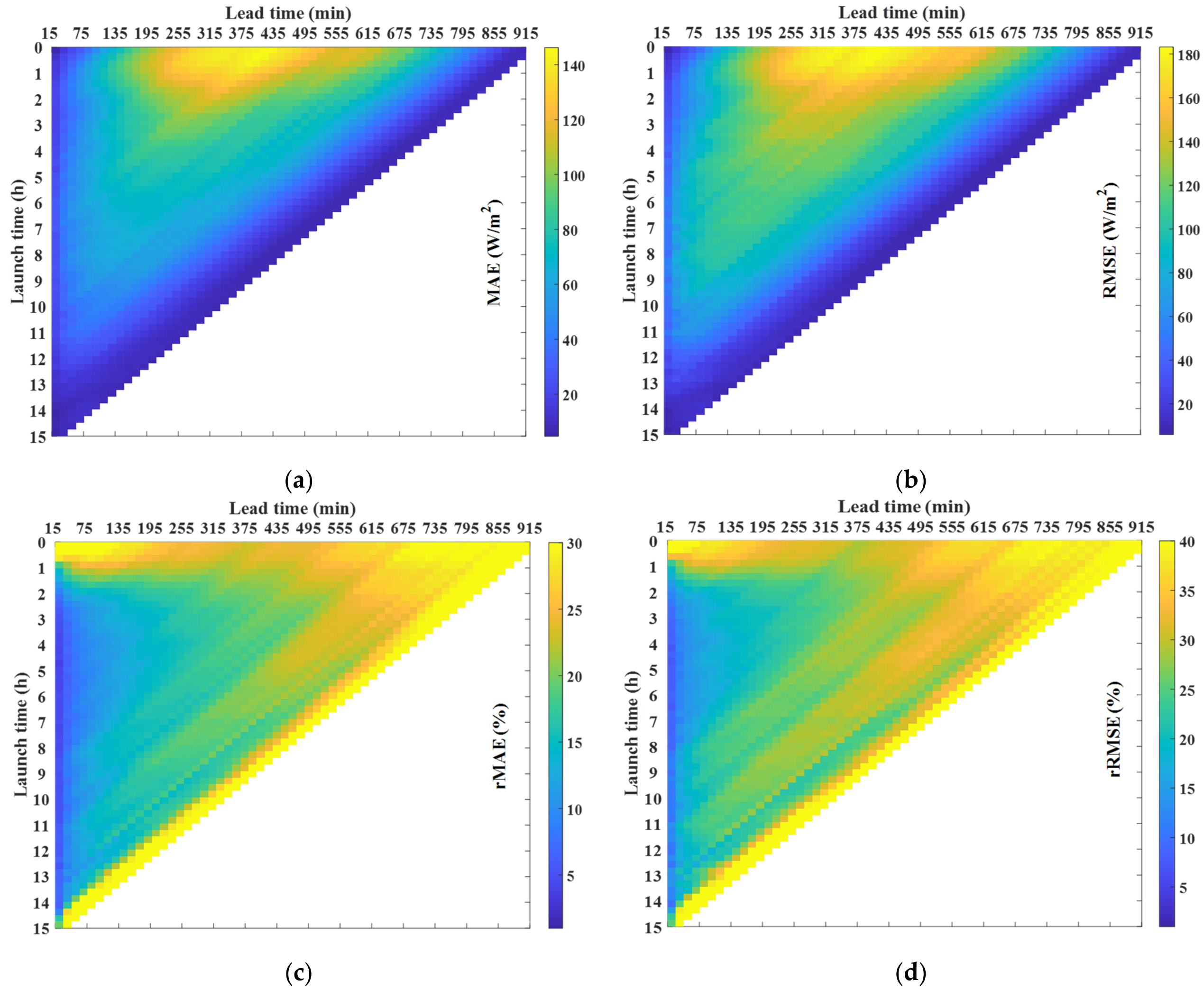

Figure 7. Error matrices obtained from GHI real measurements and GHI forecasted values, as a function of the launch time and the lead time: (**a**) MAE; (**b**) RMSE; (**c**) rMAE; and (**d**) rRMSE.

Finally, the predictions obtained by the LSTM-RNN used in this work are compared with those available in the literature, which are depicted in Table 3. It is worth noting that this comparative analysis should not be strictly considered, since each dataset can have a relative influence on the performance. Nevertheless, some preliminary conclusions can be drawn from the study. Firstly, taking into account other widely used techniques from [45], the forecast error obtained in this work, in terms of the rMAE, is much smaller under short lead times (15 min), increasing until a similar value of the error is obtained under large lead times (6 h). A good performance under small forecast horizons is also obtained when comparing the results with [46] for a statistical AutoRegressive Integrated Moving Average (ARIMA) model, in terms of the MAE, obtaining a similar error to that of traditional RNNs, and a higher error with respect to a similar LSTM-based approach presented in [46], despite considering other inputs highly correlated with the irradiance. Finally, comparing the strategy presented in this paper with respect to the deep learning techniques (GRU, LSTM-RNN, and CNN-LSTM) from [39,47–49], a similar performance can be observed. To conclude, for small lead times, the forecasting approach introduced in this paper yields better results than those obtained by traditional methods. However, the forecasting error of the proposed LSTM-RNN-based method increases for higher lead times, until a similar performance is obtained with respect to the traditional methods compared from the literature. It is also observed that an increase in the number of inputs seems to slightly improve the performance of the forecast approach. Adding exogenous inputs to the forecast process is an alternative which is often used by researchers but negatively affects the performance when those resources are not available.

Table 3. Comparison between the research results from this paper and those from other articles in the literature.

Model [Article]	Error	Forecast Horizon	Time Interval	Inputs	Results from This Paper
Smart pers. [45] CIAD Cast [45] Satellite [45] WRF-Solar [45] SVM-Radial [45]	$rMAE = (8–18)\%$ $rMAE = (11–20)\%$ $rMAE = (10.5–19.5)\%$ $rMAE = (12–18)\%$ $rMAE = (7.5–15.5)\%$	6 h	15 min	GHI, Clear Sky GHI, Cloud index maps, Cloud top height maps, ...	$rMAE = (4.17–17.73)\ \%$
ARIMA [46] RNN [46] LSTM [46]	$MAE = 71.48\ \mathrm{W/m^2}$ $MAE = 41.83\ \mathrm{W/m^2}$ $MAE = 31.86\ \mathrm{W/m^2}$	1 h	1 h	GHI, Clear Sky GHI, Cloud type, Temperature, Humidity, Precipitation, Wind, ...	$MAE = 41.88\ \mathrm{W/m^2}$
CNN-LSTM [39] CNN-LSTM [39] CNN-LSTM [39] CNN-LSTM [39]	$MAE = 41.88\ \mathrm{W/m^2}$ $RMSE = 78.17\ \mathrm{W/m^2}$ $rMAE = 10.58\ \%$ $rRMSE = 19.75\ \%$	1 h	1 h	GHI, Temperature, Wind, Precipitation, Humidity, Azimuth, ...	$MAE = 41.88\ \mathrm{W/m^2}$ $RMSE = 72.54\ \mathrm{W/m^2}$ $rMAE = 8.72\ \%$ $rRMSE = 15.1\ \%$
LSTM [47] LSTM [47]	$RMSE = (77–143)\ \mathrm{W/m^2}$ $rRMSE = (18.4–33)\%$	8 h	1 h	GHI, Humidity, Cloudiness, Temperature, Extra-terrestrial	$RMSE = (72–124)\ \mathrm{W/m^2}$ $rRMSE = (15.1–29.2)\ \%$
GRU [48] LSTM [48]	$RMSE = 67.29\ \mathrm{W/m^2}$ $RMSE = 66.57\ \mathrm{W/m^2}$	1 h	1 h	GHI, Zenith, Humidity, Temperature	$RMSE = 72.54\ \mathrm{W/m^2}$
GRU [49] LSTM [49]	$RMSE = 58\ \mathrm{W/m^2}$ $RMSE = 55.29\ \mathrm{W/m^2}$	30 min	1 min	GHI	$RMSE = 55.78\ \mathrm{W/m^2}$

3.2. PV Power Estimation from the Forecasted GHI

The following step consists of estimating the power delivered by the PV modules from the GHI forecasts. To this end, the following parameters are required: (i) the prediction time instant; (ii) the site location in terms of latitude, longitude, and altitude; (iii) the installation characteristics, which include the orientation and inclination of the panels, rated parameters of the PV models available in datasheets, and losses associated with each part of the installation; and (iv) the ambient temperature, obtained from NWP maps. As stated above, analytical techniques exist to achieve this goal and, as a result, it is possible to quantify the error committed in the procedure.

This section focuses on two different approaches Firstly, real measurements of PV power are compared against the estimated values of PV power obtained from real measurements of GHI at the site. Secondly, the PV power is estimated from the forecasted values of GHI, evaluating the errors associated with the whole process. The GHI conversion searches for a reduced value of the error to maintain a similar performance to that obtained in the previous section, using the errors to construct the prediction intervals (Section 3.3).

Figure 8 depicts the comparison between the measured values of PV power at the site with respect to the PV power estimation obtained from real GHI measurements taken at the site. Three types of days have been selected: a cloudy day, an overcast day and a sunny day. The x axis is expressed in solar time. It is worth noting that the experimental setup at the site location has a building near the PV panels that generates partial shadows on some of them, starting from 16:36 and continuing until sunset. This event is also modelled in Equation (2), assuming a linear variation of this effect with respect to time (in Figure 8 $SF = 0.95$ at 16:36, decreasing until $SF = 0.4$ at sunset), and it also varies depending on the season of the year. Results show a reduced value for the error similar to that reported in other works [28], obtaining an $rMAE = 2.54\%$ for sunny days, an $rMAE = 3.04\%$ for partially cloudy days, and an increased value of $rMAE = 4.03\%$ for overcast days. In terms of the squared error, values range from $rRMSE = 3.44\%$ on sunny days and $rRMSE = 3.90\%$ on partially cloudy days, to $rRMSE = 5.95\%$ for overcast days. The transient characteristic of the inverter MPPT controller reveals that, in the presence of passing clouds, the inverter operating point becomes unstable. This is the reason why the error increases on these days. However, this does not pose any problem for the forecasting process since the time interval is 15 min, which considerably mitigates this negative effect.

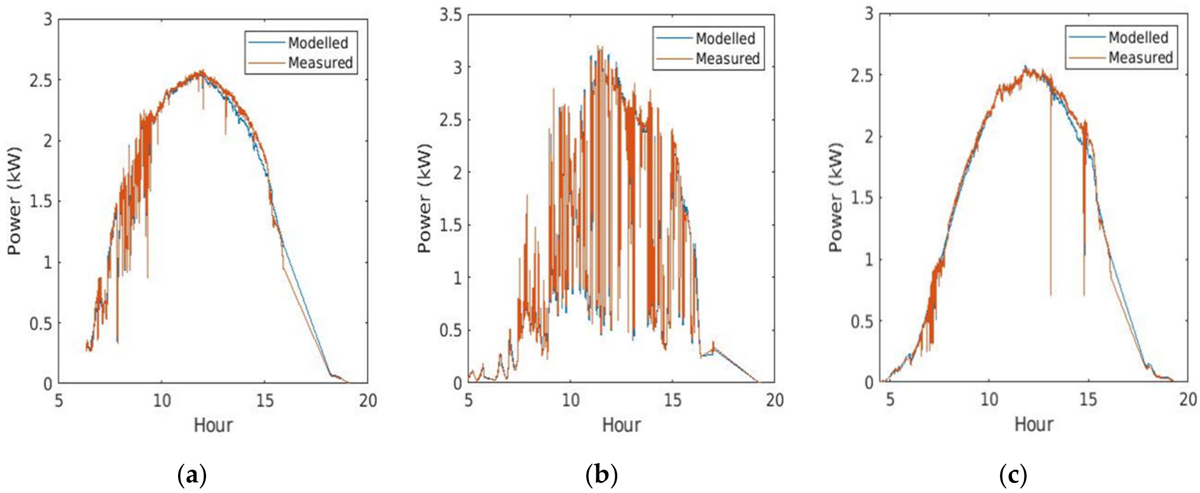

Figure 8. Comparison between the measured values of PV power with respect to values obtained from the conversion of real GHI measurements at the site. The selected days are: (**a**) a partially cloudy day (17 May 2021: $rMAE = 3.04\%$ $rRMSE = 3.90\%$), (**b**) an overcast day (1 June 2021: $rMAE = 4.03\%$ $rRMSE = 5.95\%$) and (**c**) a sunny day (4 June 2021: $rMAE = 2.54\%$ $rRMSE = 3.44\%$).

Finally, Figure 9 depicts the forecast error in terms of the difference between the measured and estimated PV power as a function of the lead time and the launch time. The shapes of the figures are similar to the previous section, with similar percentage errors. Therefore, from the figure, the same conclusions reached by analyzing Figure 7 can be drawn: (i) the scaled error is high for short launch times and medium lead times but decreases significantly as the launch time increases; (ii) for launch times of less than an hour the percentage error is high, irrespective of the lead time; and (iii) the percentage error is high at lead times higher than approximately 7 h. The forecast error, which is dependent on the lead time and the launch time, is used to generate the prediction intervals in the following section.

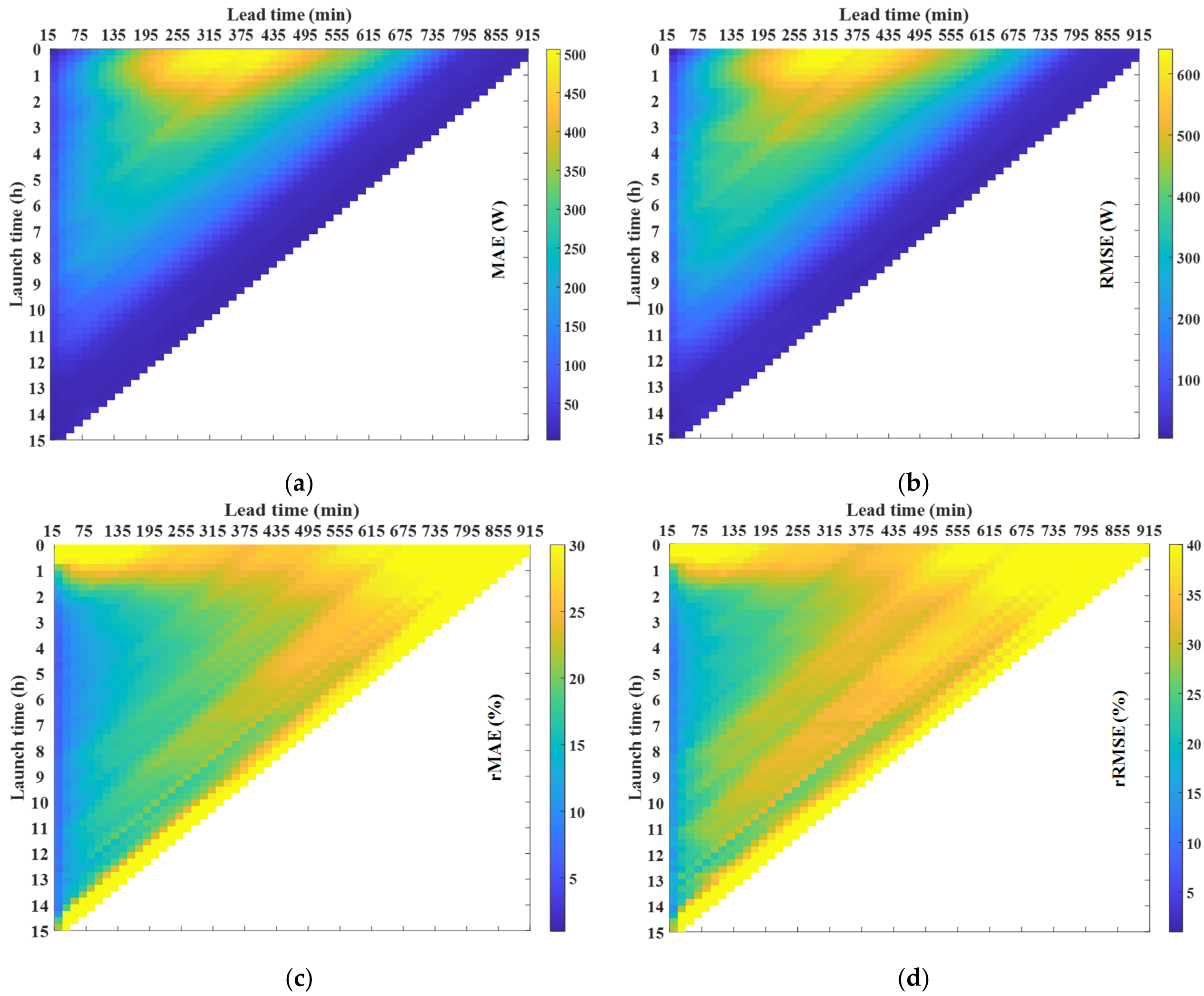

Figure 9. Error matrices obtained from PV power real measurements and PV power estimated values, as a function of the launch time and the lead time: (**a**) MAE; (**b**) RMSE; (**c**) rMAE; and (**d**) rRMSE.

3.3. Prediction Intervals of the Forecasted PV Power

Prediction intervals provide additional information about the plausible range of PV energy that will be generated at the site, for a defined confidence level selected by the user. Prediction intervals also indicate the degree of uncertainty in point forecasts. This could avoid unexpected energy shortages or, by contrast, energy surpluses, which are less critical than the former since the inverter can change its operational point to produce only the energy needed, despite wasting an exploitable energy resource.

In this paper, prediction intervals are obtained based on the work carried out in [44]. Previous results show how dependent the forecast accuracy is on the lead time and the launch time. This fact is used to split the dataset of predictions and create groups, assuming a specific distribution which is built based on the *MAE*. Therefore, each group is defined by selecting a launch time and a lead time, obtaining 365 samples per group, since a whole year is forecasted on this research. Figure 10 shows different error distributions for launch time values of 2, 4, and 6 h, and lead time values of 1, 2, and 3 h. In all of them, a Laplacian distribution is considered, similar to the work carried out in [37] but as a function of the CCF. Prediction intervals ($E_{15m} \pm p_s$) for each subset can be defined in terms of the *MAE* under this assumption: for a Laplacian distribution, a percentile p of probability $(1-s)$ has an interval of $p_s = \pm MAE \cdot \ln(2s)$.

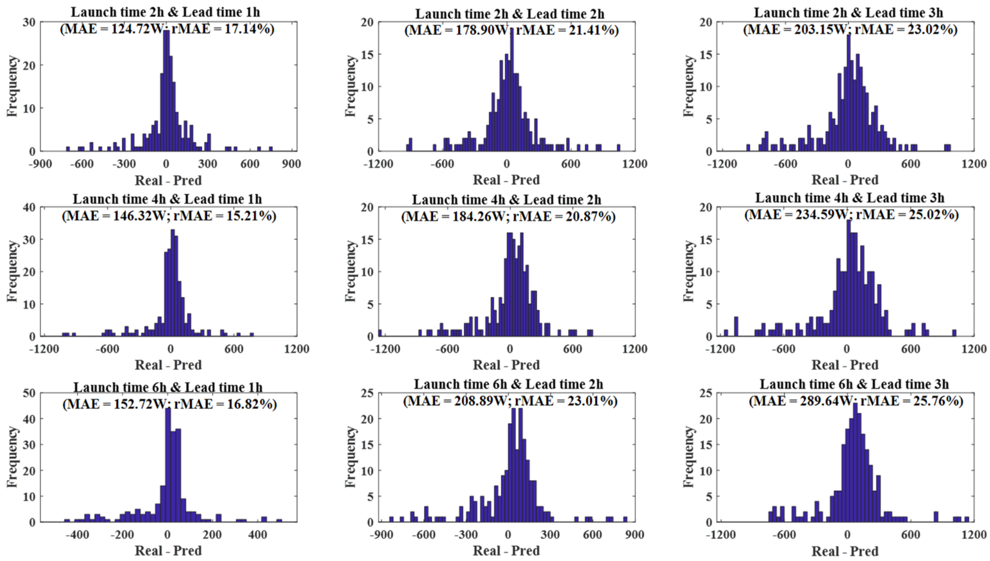

Figure 10. Error distribution for different subsets. A Laplacian distribution is assumed to create prediction intervals in terms of the MAE.

More detailed distributions can be determined provided that the selected groups are also created as a function of the CCF. However, by considering 10 groups as presented in [37], the number of samples of each group is not sufficient to create a proper error distribution. To overcome this drawback, the number of CCF groups is reduced to three, using the type of day classification criteria (e.g., sunny, cloudy, and overcast). The CCF parameter has an hourly resolution, its value is 0 when the sun is not covered by clouds and 1 when the sunlight is totally blocked. The type of day is classified evaluating the CCF during the daylight hours, with an hourly weighting of the amount of energy produced during the day. After that, the k-nearest neighbors (k-NN) method is used to form the groups, since it allows the dataset to be split in a simple way, offering an independent solution for each site in the VPP.

The assumption of a Laplacian distribution for each new selected subset carries an error that is necessary to quantify. The Prediction Interval Coverage Probability (*PICP*) [50], in Equation (4), indicates the percentage of predicted values that are inside the interval selected, and it must be close to the confidence level (γ_L). The confidence level selected in this research is $\gamma_L = 80\%$, although this parameter can be modified depending on the operational risks that the site can handle: the higher the risks, the higher the benefits from the installation:

$$PICP = \frac{1}{T}\sum_{t=1}^{T}\epsilon_t,\ \text{where}\ \epsilon_i = \begin{cases} 1\ \text{if}\ x_i \in [\mathrm{L_i},\ \mathrm{U_i}] \\ 0\ \text{if}\ x_i \notin [\mathrm{L_i},\ \mathrm{U_i}] \end{cases}. \tag{4}$$

Figure 11 depicts the absolute difference between the confidence level and the *PICP* for each type of day, being an effective method when this difference is close to zero. On sunny days, the *PICP* is close to the confidence level across the whole area, except for high lead times under small launch times where the difference increases. On cloudy days, the *PICP* is quite different from the confidence level during sunset. Nevertheless, the difference is acceptable in the rest of the area. In this case, the forecast has a lesser value during sunset since the energy produced is significantly reduced. Hence, prediction intervals also offer valuable information on cloudy days. Finally, for overcast days, the difference between the *PICP* and the confidence level increases with respect to sunny days, but the magnitude is acceptable and the prediction intervals are still valuable. To conclude, there are some zones with a high difference between the *PICP* and the confidence level. However, these scenarios correspond to small PV power measurements with bad forecasting performance

(Figure 9). Therefore, prediction intervals are of little value for these points, since the strategy presented in this paper does not focus on those cases.

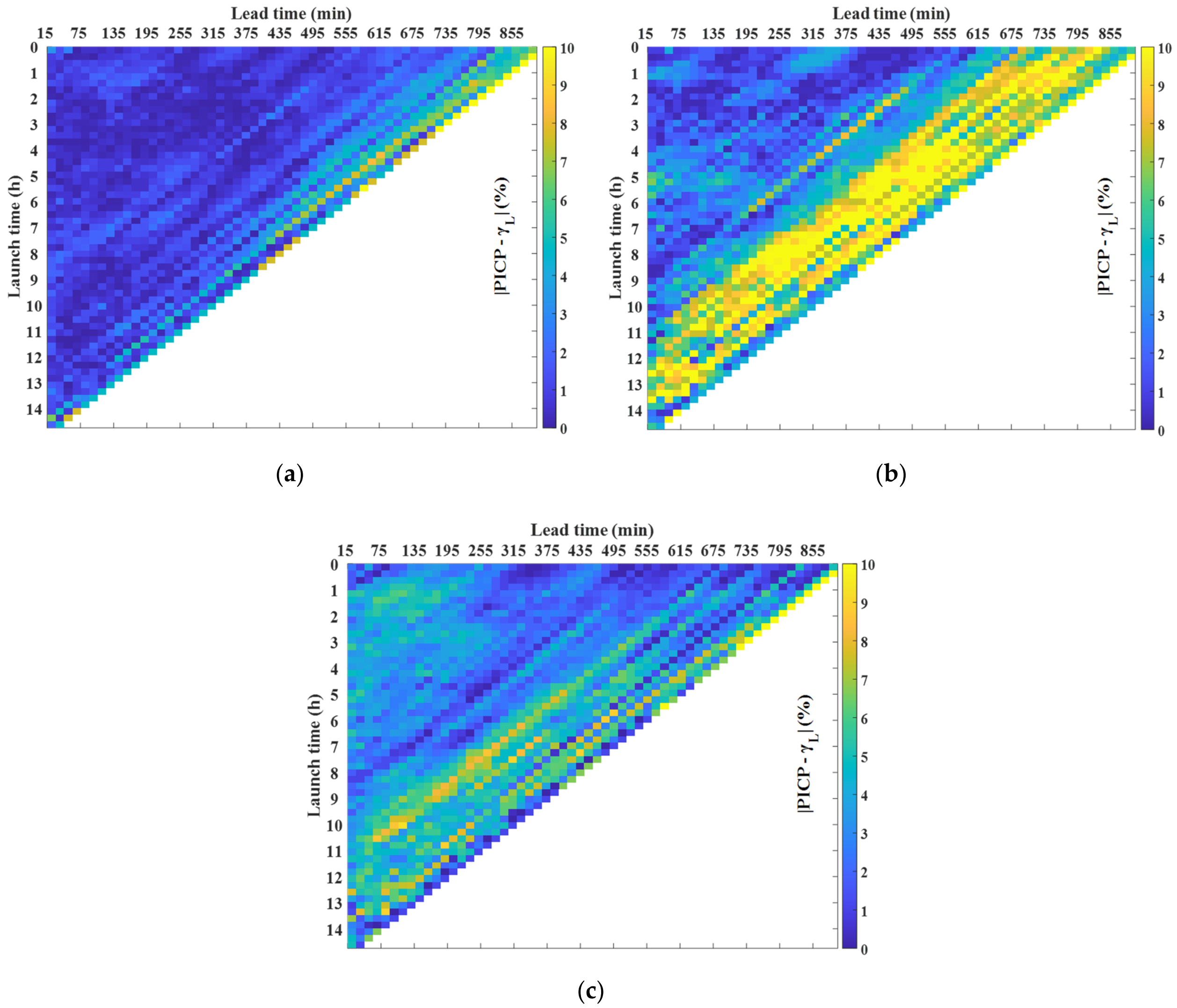

Figure 11. Absolute difference between the *PICP* and the confidence level for every subset selected on the prediction intervals for different types of day: (**a**) sunny; (**b**) cloudy; and (**c**) overcast.

3.4. Evaluation of the GHI Forecasting for an Emulated VPP

The effectiveness of the whole forecasting process has been demonstrated for a single PV installation, which plays the role of a VPP node, along with its limitations with respect to the launch time and the lead time. The next step consists of assessing the algorithm performance for a set of PV facilities, forming a VPP. There are, however, no additional PV installations available in the study. Therefore, seven ground-based meteorological stations located in the Community of Madrid, apart from the PV facility at the university, are used to emulate the VPP nodes. Their locations are depicted in Figure 12. These ground-based stations are equipped with GHI sensors which allow the GHI forecasts to be generated. As for the power conversion, the characteristics of the PV installation from the university are used to obtain the power estimation for each emulated VPP node (peak power, $P_{peak} = 2.97$ kW, temperature coefficient, $\delta P_m = -0.4\%/°$C, and the performance of the equipment).

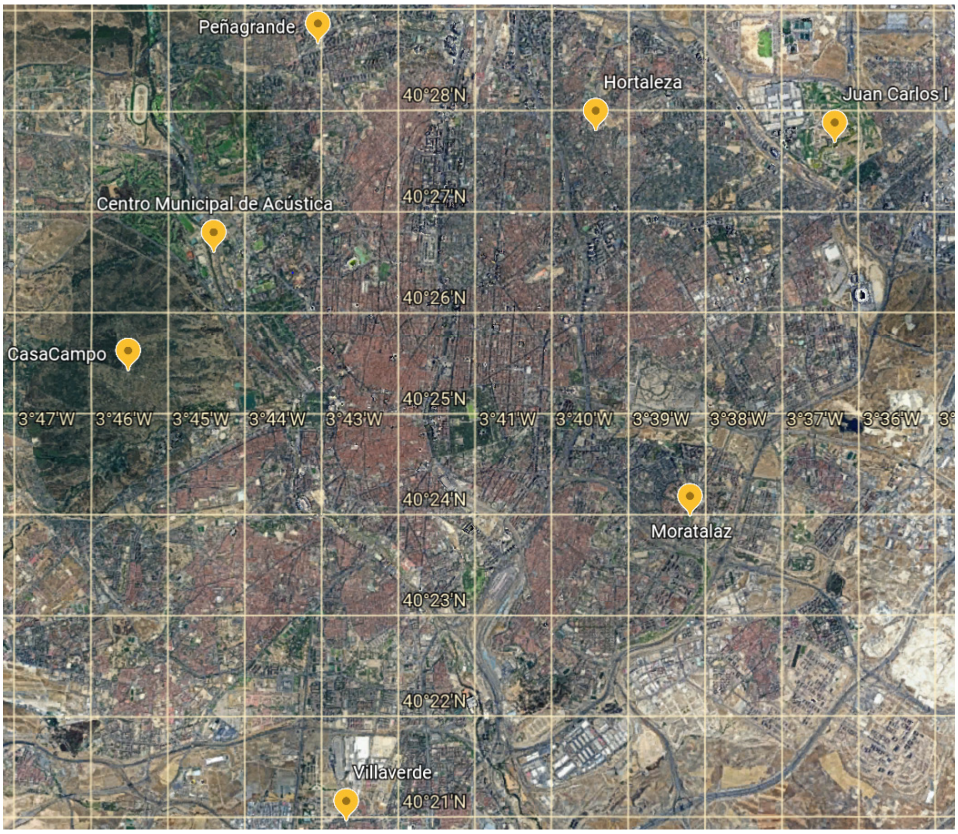

Figure 12. Location of the ground-based stations in the Community of Madrid used in the research.

The same results as those shown in Figure 9 are used to quantify the accuracy of the prediction. However, in this case, the PV power forecast for each station is individually evaluated and the sum of power forecasts of the stations represents the PV power generated by the VPP, whose forecast error is depicted in Figure 13. By doing so, the PV power obtained at each station can be compared with respect to the total PV power forecasted. It can be observed that the scaled values of the error (MAE and RMSE) are higher than those in Figure 9. However, there is an 8-fold increase in the peak power with respect to a single facility. As a result, by looking at the relative values of the error (rMAE and rRMSE) it can be noted that the performance of the prediction increased for the VPP. The accuracy improvement of the PV power forecast can be expressed as the difference between the VPP forecast error and the sum of the error on each installation, dividing that value by the mean error committed on a single installation, obtaining a mean value of 12.37% with respect to the MAE, and 11.84% with respect to the RMSE. The shapes of the figures lead to identical conclusions to those reached by the analysis in Figure 9. Therefore, the prediction intervals maintain their potential value for error forecasting in the case of a VPP.

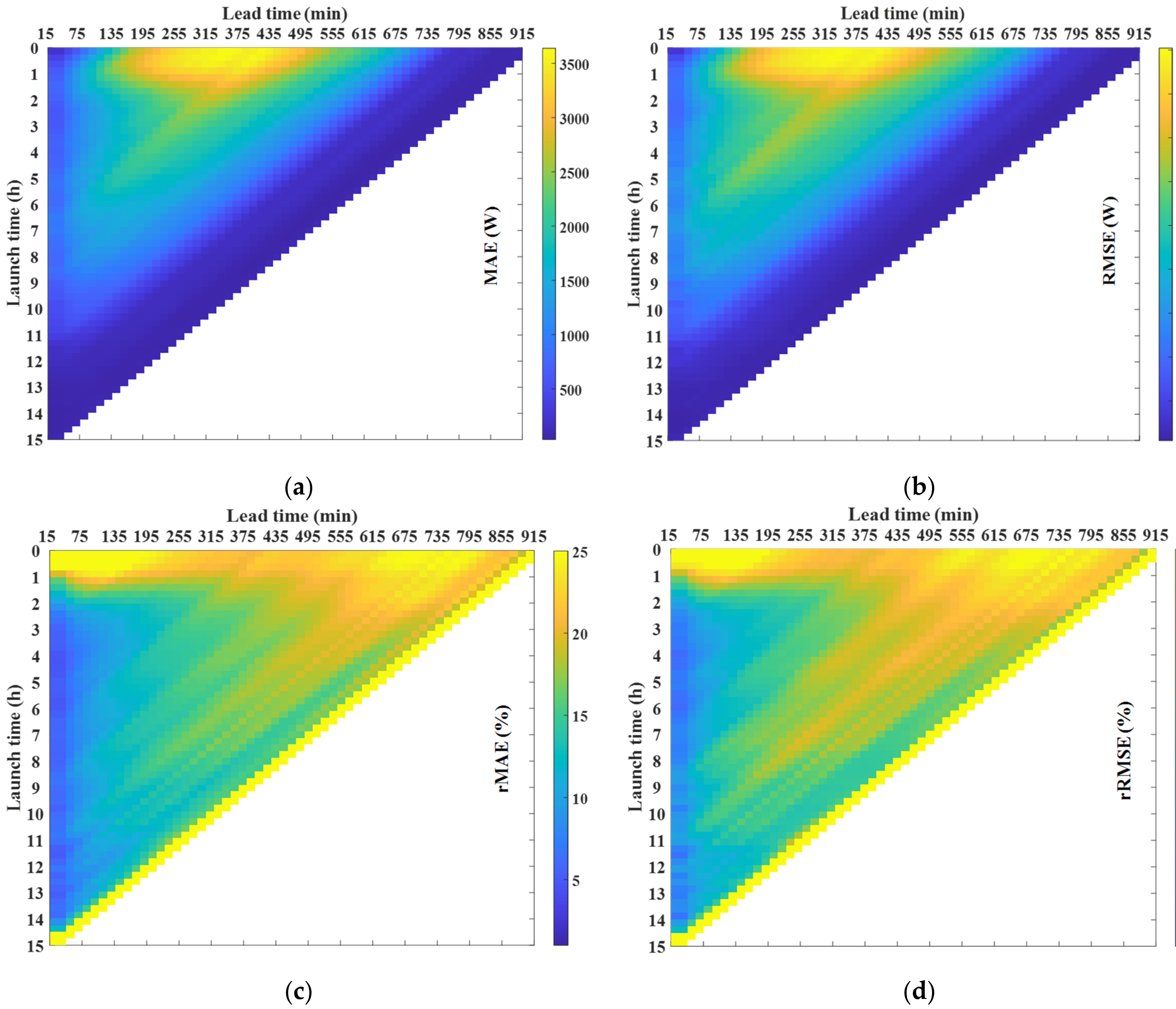

Figure 13. Error matrices of PV power forecasts from the VPP emulated in the research, represented as the sum of 8 different VPP nodes located in the Community of Madrid, as a function of the launch time and the lead time: (**a**) *MAE*; (**b**) *RMSE*; (**c**) *rMAE*; and (**d**) *rRMSE*.

4. Discussion and Conclusions

The technical development of VPPs must be supported by EMSs, for which PV power forecasting is an essential part. By knowing the energy produced by each VPP node, usually based on renewable resources such as solar technologies, it is possible to optimize the expected profit generated by energy exchanges with the grid operator. However, it is difficult to obtain PV power forecasts when it is necessary to gather information from several nodes scattered throughout a wide area, especially when the input data, required for the predictions, incur costs. This research presents a way of accomplishing this objective, using an LSTM-RNN-based strategy to, firstly, forecast the GHI by using a dataset of irradiance values derived from satellite data freely obtained from the CAMS, and secondly, estimate the solar power by utilizing a PV model of the installation. The forecast is updated during the day to achieve the highest accuracy, and prediction intervals are estimated as a function of the *MAE*. This provides a useful framework to understand the behavior of each installation that composes the VPP.

The first results provided are related to the GHI forecast for the installation and are based on the lead time and the launch time, which allow zones with a reduced error and a high level of confidence to be created in the shape of prediction intervals which depend on the type of day. The GHI error, as a function of the lead time and the launch time, shows a low performance when the launch time is lower than 1.5 h, corresponding to sunrise. To avoid this, the forecasting process can begin at 1.5 h after sunrise; before this time, this research can rely on the day-ahead prediction made in [37] to obtain the irradiance forecast. To assess the accuracy of the intraday forecast, the results have been compared with those in the literature, achieving similar results to those obtained from deep learning algorithms and outperforming traditional techniques. The distinction between the lead time and the launch time means it possible to create better comparisons with respect to the literature, but also means it is difficult to summarize the research with only one value. The *MAE* committed, without considering the lead time and the launch time, is of 44.19 W/m^2, which is coherent with other studies.

Once the irradiance is forecasted, the conversion to PV power is analytically calculated, minimizing the error, which ranges from 2.54% to 4.03% in terms of the *rMAE* and from 3.44% to 5.95% in terms of the *rRMSE*. The error committed in this case is similar to the errors found in other articles [26,28]. The shapes of the error matrixes show similar results to those presented above. Therefore, similar conclusions can be drawn. The global *MAE* committed in this case is 137.21 W in a PV facility of 2.97 kW_p.

Prediction intervals are selected once the PV power forecast is available, which allow a range of plausible values of point forecasts to be obtained. The method considers a Laplacian distribution of the error and distinguishes between the lead time, the launch time and the type of day, which is selected with a k-NN algorithm as a function of the CCF. To verify whether the boundaries maintain the associated level of confidence, the *PICP* is calculated, obtaining values close to the selected confidence level of $\gamma_L = 80\%$. In this case, results reveal a noticeable difference between the *PICP* and the confidence level on cloudy days close to sunset. However, the predictions at those hours have minor importance. It can be concluded that the selected prediction intervals are of great relevance.

Finally, the PV power forecast is created, and the prediction intervals are selected for the PV facility so that conclusions under a VPP environment can be drawn. In this case, a real PV facility and seven ground-based weather stations in the Community of Madrid are selected to emulate the VPP, obtaining an improvement in the accuracy of 12.37% with respect to the *MAE*, and 11.84% with respect to the *RMSE*. Similar conclusions can be reached regarding the error as a function of the lead time and the launch time. Therefore, the whole strategy can be applied under different scenarios for launch times higher than 1.5 hours, relying on the day-ahead prediction prior to this. For this case, the error matrixes also indicate the best moments to obtain the predictions of the nodes, making it possible to increase the reliability of the VPP operation.

The major limitation of this study is related to the information of temperature and cloudiness freely obtained in Spain from NWP maps. In locations where this information is not available forecasts cannot be provided. Future works will focus on the application of this strategy along with a day-ahead time horizon strategy to schedule the operation of a VPP, creating a software that simplifies the process.

Author Contributions: G.M., C.S., P.M. and F.J.R. developed the forecasting framework of the research, generated the predictions of the installation, created the prediction intervals and emulated the VPP; R.P. and G.M. developed the model to obtain the PV power system from GHI; G.M., C.S., P.M., R.P. and B.V. carried out the experimental tests and wrote the manuscript. All authors have read and agreed to the published version of the manuscript.

Funding: This research was funded by the Ministry of Science, Innovation and University of the Government of Spain under the HELIOS Sharing project (RTC-2017-6231-3) and Autonomous Community of Madrid under projects P2018/EMT-4366 and Y2020/EMT-6368.

Institutional Review Board Statement: Not applicable.

Informed Consent Statement: Not applicable.

Data Availability Statement: The datasets generated for this study are available on request to the author Guillermo Moreno.

Acknowledgments: The authors thank the company CLYSEMA SA for their collaboration in this research.

Conflicts of Interest: The authors declare no conflict of interest.

References

1. Goodstein, E.; Lovins, L.H. A pathway to rapid global solar energy deployment? Exploring the solar dominance hypothesis. *Energy Res. Soc. Sci.* **2019**, *56*, 101197. [CrossRef]
2. Nosratabadi, S.M.; Hooshmand, R.A.; Gholipour, E. A comprehensive review on microgrid and virtual power plant concepts. *Renew. Sustain. Energy Rev.* **2017**, *67*, 341–363. [CrossRef]
3. Das, U.K.; Tey, K.S.; Seyedmahmoudian, M.; Mekhilef, S.; Idris, M.Y.I.; Van Deventer, W.; Horan, B.; Stojcevski, A. Forecasting of photovoltaic power generation and model optimization: A review. *Renew. Sustain. Energy Rev.* **2018**, *81*, 912–928. [CrossRef]
4. Kudo, M.; Takeuchi, A.; Nozaki, Y.; Endo, H.; Sumita, J. Forecasting electric power generation in a photovoltaic power system for an energy network. *Electr. Eng. Jap.* **2009**, *167*, 16–23. [CrossRef]
5. Raza, M.Q.; Nadarajah, M.; Ekanayake, C. On recent advances in PV output power forecast. *Sol. Energy* **2016**, *136*, 125–144. [CrossRef]
6. Wan, C.; Zhao, J.; Song, Y.; Xu, Z.; Lin, J.; Hu, Z. Photovoltaic and solar power forecasting for smart grid energy management. *CSEE J. Power Energy Syst.* **2015**, *1*, 38–46. [CrossRef]
7. Massidda, L.; Marrocu, M. Smart meter forecasting from one minute to one year horizons. *Energies* **2018**, *11*, 3520. [CrossRef]
8. McCandless, T.C.; Haupt, S.E.; Young, G.S. A regime-dependent artificial neural network technique for short-range solar irradiance forecasting. *Renew. Energy* **2016**, *89*, 351–359. [CrossRef]
9. Diagne, M.; David, M.; Lauret, P.; Boland, J.; Schmutz, N. Review of solar irradiance forecasting methods and a proposition for small-scale insular grids. *Renew. Sustain. Energy Rev.* **2013**, *27*, 65–76. [CrossRef]
10. Makridakis, S.; Spiliotis, E.; Assimakopoulos, V. Statistical and Machine Learning forecasting methods: Concerns and ways forward. *PLoS ONE* **2018**, *13*, e0194889. [CrossRef] [PubMed]
11. Wang, F.; Yu, Y.; Zhang, Z.; Li, J.; Zhen, Z.; Li, K. Wavelet decomposition and convolutional LSTM networks based improved deep learning model for solar irradiance forecasting. *Appl. Sci.* **2018**, *8*, 1286. [CrossRef]
12. Li, G.; Wang, H.; Zhang, S.; Xin, J.; Liu, H. Recurrent neural networks based photovoltaic power forecasting approach. *Energies* **2019**, *12*, 2538. [CrossRef]
13. Cerqueira, V.; Torgo, L.; Soares, C. Machine learning vs statistical methods for time series forecasting: Size matters. *arXiv* **2019**, arXiv:1909.13316.
14. Voyant, C.; Notton, G.; Kalogirou, S.; Nivet, M.L.; Paoli, C.; Motte, F.; Fouilloy, A. Machine learning methods for solar radiation forecasting: A review. *Renew. Energy* **2017**, *105*, 569–582. [CrossRef]
15. Kostylev, V.; Pavlovski, A. Solar power forecasting performance–towards industry standards. In Proceedings of the 1st International Workshop on the Integration of Solar Power into Power Systems, Aarhus, Denmark, 24–25 October 2011; pp. 1–8.
16. Rajagukguk, R.A.; Ramadhan, R.A.; Lee, H.J. A Review on Deep Learning Models for Forecasting Time Series Data of Solar Irradiance and Photovoltaic Power. *Energies* **2020**, *13*, 6623. [CrossRef]
17. Antonanzas, J.; Osorio, N.; Escobar, R.; Urraca, R.; Martinez-de-Pison, F.J.; Antonanzas-Torres, F. Review of photovoltaic power forecasting. *Sol. Energy* **2016**, *136*, 78–111. [CrossRef]
18. Chatfield, C. Prediction intervals for time-series forecasting. In *Principles of Forecasting*; Springer: Boston, MA, USA, 2001; Volume 30, pp. 475–494. [CrossRef]
19. Lorenz, E.; Hurka, J.; Karampela, G.; Heinemann, D.; Beyer, H.G.; Schneider, M. Qualified forecast of ensemble power production by spatially dispersed grid-connected PV systems. In Proceedings of the 23rd European PV Solar Energy Conference and Exhibition (EU PVSEC), Valencia, Spain, 1–5 September 2008; pp. 3285–3291.
20. Ghavidel, S.; Li, L.; Aghaei, J.; Yu, T.; Zhu, J. A review on the virtual power plant: Components and operation systems. In Proceedings of the 2016 IEEE International Conference on Power System Technology (POWERCON), Wollongong, NSW, Australia, 24 November 2016; pp. 1–6. [CrossRef]
21. Nakamura, M.; Takeno, K.; Hisamitsu, R.; Shoyama, M. Bi-directional Multiport Converter for Utilizing Green Base Stations as Virtual Power Plant. In Proceedings of the 8th International Conference on Renewable Energy Research and Applications, Brasov, Romania, 3–6 November 2019; pp. 137–141. [CrossRef]
22. Osterwald, C. Translation of device performance measurements to reference conditions. *Sol. Cells* **1986**, *18*, 269–279. [CrossRef]
23. Menicucci, D. Photovoltaic array performance simulation models. In Proceedings of the PV and Isolation Measurements Workshop, Vail, Colombia, 1 July 1985; pp. 383–392.
24. Marion, B. Comparison of predictive models for photovoltaic module performance. In Proceedings of the 33rd IEEE Photovoltaic Specialists Conference, San Diego, CA, USA, 11–16 May 2008; pp. 1–6. [CrossRef]
25. Marion, B.; Rummel, S.; Anderberg, A. Current–voltage curve translation by bilinear interpolation. *Prog. Photovolt.* **2004**, *12*, 593–607. [CrossRef]
26. Peña, R.; Diez-Pascual, A.; Diaz, P.; Davoise, L. A new method for current–voltage curve prediction in photovoltaic modules. *IET Renew. Power Gener.* **2021**, *15*, 1331–1343. [CrossRef]

27. Heydenreich, W.; Müller, B.; Reise, C. Describing the world with three parameters: A new approach to PV module power modelling. In Proceedings of the 23rd European PV Solar Energy Conference and Exhibition (EU PVSEC), Valencia, Spain, 1–5 September 2008; pp. 2786–2789.
28. Takilalte, A.; Harrouni, S.; Yaiche, M.; Mora-López, L. New approach to estimate 5-min global solar irradiation data on tilted planes from horizontal measurement. *Renew. Energy* **2020**, *145*, 2477–2488. [CrossRef]
29. Abdel-Nasser, M.; Mahmoud, K. Accurate photovoltaic power forecasting models using deep LSTM-RNN. *Neural Comput. & Applic.* **2019**, *31*, 2727–2740. [CrossRef]
30. Husein, M.; Chung, I.Y. Day-ahead solar irradiance forecasting for microgrids using a long short-term memory recurrent neural network: A deep learning approach. *Energies* **2019**, *12*, 1856. [CrossRef]
31. Spanish Agency of Meteorology (AEMET) Numerical Weather Predictions. Available online: http://www.aemet.es/es/eltiempo/prediccion/modelosnumericos/harmonie_arome_ccaa?opc2=mad (accessed on 27 July 2021).
32. Schwingshackl, C.; Petitta, M.; Wagner, J.E.; Belluardo, G.; Moser, D.; Castelli, M.; Zebisch, M.; Tetzlaff, A. Wind effect on PV module temperature: Analysis of different techniques for an accurate estimation. *Energy Procedia* **2013**, *40*, 77–86. [CrossRef]
33. Tradacete, M.; Santos, C.; Jiménez, J.A.; Rodríguez, F.J.; Martín, P.; Santiso, E.; Gayo, M. Turning Base Transceiver Stations into Scalable and Controllable DC Microgrids Based on a Smart Sensing Strategy. *Sensors* **2021**, *21*, 1202. [CrossRef] [PubMed]
34. The MathWorks, I. ThingSpeak for IoT Projects. Available online: https://thingspeak.com/ (accessed on 27 July 2021).
35. Commission, E. Copericus Europe's eyes on Earth. Available online: https://www.copernicus.eu/en (accessed on 27 July 2021).
36. Malý, J. The Darboux property for gradients. *Real Anal. Exch.* **1996**, *22*, 167–173. [CrossRef]
37. Moreno, G.; Martin, P.; Santos, C.; Rodríguez, F.J.; Santiso, E. A Day-Ahead Irradiance Forecasting Strategy for the Integration of Photovoltaic Systems in Virtual Power Plants. *IEEE Access* **2020**, *8*, 204226–204240. [CrossRef]
38. Bengio, Y.; Simard, P.; Frasconi, P. Learning long-term dependencies with gradient descent is difficult. *IEEE Trans. Neural Netw.* **1994**, *5*, 157–166. [CrossRef]
39. Zang, H.; Liu, L.; Sun, L.; Chen, L.; Wei, Z.; Sun, G. Short-term global horizontal irradiance forecasting based on a hybrid CNN-LSTM model with spatiotemporal correlations. *Renew. Energy* **2020**, *160*, 26–41. [CrossRef]
40. Berrizbeitia, S.E.; Jadraque Gago, E.; Muneer, T. Empirical Models for the Estimation of Solar Sky-Diffuse Radiation. A Review and Experimental Analysis. *Energies* **2020**, *13*, 701. [CrossRef]
41. Davies, J.; Hay, J. Calculations of the solar radiation incident on an inclined surface. In Proceedings of the First Canadian Solar Radiation Data Workshop, Toronto, ON, Canada, 17–19 April 1978; pp. 32–58.
42. Martin, N.; Ruiz, J. Calculation of the PV modules angular losses under field conditions by means of an analytical model. *Sol. Energy Mater. Sol. Cells* **2001**, *70*, 25–38. [CrossRef]
43. King, D.L.; Boyson, W.E.; Kratochvil, J.A. *Photovoltaic Array Performance Model*; Sandia National Laboratories: Albuquerque, NM, USA, 2003; pp. 1–43.
44. Fonseca Junior, J.G.D.S.; Oozeki, T.; Ohtake, H.; Takashima, T.; Kazuhiko, O. On the use of maximum likelihood and input data similarity to obtain prediction intervals for forecasts of photovoltaic power generation. *J. Electr. Eng. Technol.* **2015**, *10*, 1342–1348. [CrossRef]
45. Huertas-Tato, J.; Aler, R.; Galván, I.; Rodríguez-Benítez, F.; Arbizu-Barrena, C.; Pozo-Vázquez, D. A short-term solar radiation forecasting system for the Iberian Peninsula. Part 2: Model blending approaches based on machine learning. *Sol. Energy* **2020**, *195*, 685–696. [CrossRef]
46. Yu, Y.; Cao, J.; Zhu, J. An LSTM short-term solar irradiance forecasting under complicated weather conditions. *IEEE Access* **2019**, *7*, 145651–145666. [CrossRef]
47. Chen, X.; Huang, X.; Cai, Y.; Shen, H.; Lu, J. Intra-day Forecast of Ground Horizontal Irradiance Using Long Short-term Memory Network (LSTM). *J. Meteorol. Soc. Jpn.* **2020**, *5*, 945–957. [CrossRef]
48. Wojtkiewicz, J.; Hosseini, M.; Gottumukkala, R.; Chambers, T.L. Hour-ahead solar irradiance forecasting using multivariate gated recurrent units. *Energies* **2019**, *12*, 4055. [CrossRef]
49. Yan, K.; Shen, H.; Wang, L.; Zhou, H.; Xu, M.; Mo, Y. Short-term solar irradiance forecasting based on a hybrid deep learning methodology. *Information* **2020**, *11*, 32. [CrossRef]
50. Van der Meer, D.W.; Widén, J.; Munkhammar, J. Review on probabilistic forecasting of photovoltaic power production and electricity consumption. *Renew. Sust. Energ. Rev.* **2018**, *81*, 1484–1512. [CrossRef]